5-2014

Formulation and Experimental Verification of Alternate Calibration Techniques of the Temperature Dependent Response of Phosphor Fluorescence

Kelsey Michele Winstead
University of Tennessee - Knoxville, kwinstea@utk.edu

To the Graduate Council:

I am submitting herewith a thesis written by Kelsey Michele Winstead entitled "Formulation and Experimental Verification of Alternate Calibration Techniques of the Temperature Dependent Response of Phosphor Fluorescence." I have examined the final electronic copy of this thesis for form and content and recommend that it be accepted in partial fulfillment of the requirements for the degree of Master of Science, with a major in Mechanical Engineering.

Jay I. Frankel, Major Professor

We have read this thesis and recommend its acceptance:

Majid Keyhani, Rao V. Arimilli

Accepted for the Council:
Carolyn R. Hodges

Vice Provost and Dean of the Graduate School

(Original signatures are on file with official student records.)

Formulation and Experimental Verification of Alternate Calibration Techniques of the Temperature Dependent Response of Phosphor Fluorescence

A Thesis Presented for the
Master of Science
Degree
The University of Tennessee, Knoxville

Kelsey Michele Winstead
May 2014

DEDICATION

This work is dedicated to my loving husband, Hobbie Turley, who has supported me constantly and put up with my long work hours. I am so grateful to have him in my life.

This work is also dedicated to my parents, Joel and Suzanne Winstead, and my little brother Christopher Winstead. They have always been a tremendous source of encouragement in both my academic and personal endeavors.

I love you all very much.

ACKNOWLEDGEMENTS

First, I would like to thank my advisor, Dr. Jay Frankel, for his time, consideration, and constant support. He has taught me to be creative in my thinking so that I can approach scientific problems in new ways. He is always willing to stop what he is doing to help me or give advice. His encouragement and understanding has been essential to the completion of this research. I would also like to thank my co-advisor, Dr. Majid Keyhani, for taking me under his wing and teaching me how to be an experimentalist. Through his support and patience, I gave grown from a dependent undergraduate research aid into an independent researcher that is able to design experiments and interrogate problems in a thorough and insightful manner.

I would also like to thank Dr. Rao Arimilli for serving on this committee. He has taught many of my classes and has helped to expand my knowledge on subjects pertinent to my work.

I would also like to thank Dr. Steve Allison and Emerging Measurements (emco) for their involvement in this work and providing essential pieces of equipment. Dr. Allison has spent a lot of time helping me investigate problems of my experiment and without him this thesis would probably not have been completed.

A very important thanks also goes to my friend Adam Travis, who has been my partner in crime throughout all of undergraduate and graduate school. He has put up with my panicky fears about failing classes and most of the time resisted rolling his eyes when I ended up doing well. He helped to make classes and studying a lot more fun.

I would also like to thank my fellow graduate students Dominik Bottlaender, Yinyuan Chen, Hongchu Chen, and Abhay Pande for all the help they have given me. I would like to thank my lab mate Alex Hashemian. It has been a privilege to know and work alongside him. Without his help I would not have been able to construct the many pieces of my experimental setup that involved power tools. I would also like to thank Jake Plewa for helping to teach me the ropes of the heat transfer lab and also for his friendship.

Finally, I am very grateful to my advisors, Dr. Frankel and Dr. Keyhani, for funding for my research and education through my years in graduate school. In this regard, I would like to thank NASA-EPSCoR (NNX10AN35A) for providing monetary support.

ABSTRACT

The overall goal of this work is to provide an alternative approach to the thermographic phosphor (TP) time constant calibration method for temperature recovery. In this work two techniques are proposed that retain the pulsed source input used in the standard TP time constant calibration approach but reinterpret the phosphor response taken a fixed distance such that the single-exponential decay assumption is removed. The methods do not require knowledge of key parameters prior to data processing, nor do they involve complicated numerical schemes that attempt to fit data in the low signal-to-noise region of the phosphor response. The approaches do involve integrating the full phosphor response signal to arrive at a single value related to the integrated intensity trajectory. This value can be calibrated to temperature. One method uses the slope of the integrated intensity in the rise portion of the phosphor emission as the calibration parameter, while the second technique uses the total integral of the emission as the calibration parameter.

Both techniques are validated as an effective means of TP calibration by experimental data. First, the phosphor emission response is recorded at different steady-state temperatures in order to form a calibration curve. Different regression models are investigated to determine the functional relationship that best fits the observed calibration data. Second, the phosphor is heated under transient conditions and both calibration techniques are applied to resolve the temporal temperature history of the test sample. From the experimental results, it is found that a bi-exponential based calibration curve or a rational function based calibration curve accurately predict the temperature measurements of the transient tests for both calibration procedures. However, it is suggested that the total integrated intensity method is more reliable compared to the slope calibration method since smaller error estimates are observed using the total integral in the transient sense. Another attractive feature of the integral method is that the only numerical manipulation of the raw physical experimental data to resolve the calibration parameter involves integrating the signal. The outcome of this work is highly encouraging and indicates that these techniques could be found useful in certain applications.

TABLE OF CONTENTS

LIST OF TABLES

LIST OF FIGURES

Nomenclature

Symbols

a,b	=	arbitrary coefficients
C	=	constant
c	=	generalized calibration paramater
c_L	=	speed of light, [299705 km/s]
D_M	=	sum of squares of the deviation, [$(°C)^2$]
d_M	=	number of fitted coefficients for a given regression model
E	=	energy, [J]
f	=	generalized function
h	=	Planck's constant, [$6.626(10^{-34})$ J-s]
I	=	spectral intensity, [V]
L,M	=	generalized equation orders
m	=	number of calibration points
m'	=	total time-voltage data pairs in collected phosphor emission
k	=	Boltzmann's constant, [$1.38(10^{-23})\ \frac{m^2 - kg}{s^2 - K}$]
N	=	number of waveform shot averages
n^*	=	number of luminescent centers
P	=	probability level

p,q	=	arbitrary coefficients
R	=	local residual, [°C]
$R_{p,1}$	=	electrical resistance, [Ω]
R^2_M	=	correlation coefficient
$R^2_{adj,M}$	=	adjusted correlation coefficient
$S_{0,1,2}$	=	electron singlet state
T	=	temperature, [°C]
T_1	=	electron triplet state
$\hat{T}$	=	arithmetic mean of samples, [°C]
t	=	time variable, [s]
W	=	data sample size
X	=	oscilloscope data value for time, [s]
Y	=	oscilloscope data value for voltage, [V]
ε	=	noise parameter
η	=	slope of linear portion of integrated intensity curve, [V]
κ	=	decay rate variable, [s]
λ	=	wavelength, [m]
ν	=	residual degrees of freedom
τ	=	time constant variable, [s]

ρ = probability distribution of electron deexcitation pathway

σ = unbiased standard deviation

σ^2 = unbiased variance

φ = electron yield

$\Psi(t)$ = integrated intensity in time, [V-μs]

Ψ_T = total integrated intensity, [V-μs]

Abbreviations

CB = confidence bound

rms_M = root-mean-square error, [°C]

RMS = root-mean-square error of the residuals, [°C]

Chapter 1: Introduction

1.1 Problem Description

The expeditious advancement of technology in science and engineering fields has revealed a universal need to utilize new approaches for measuring temperature. Investigating severely hostile thermal environments has become increasingly crucial in the study of hypersonic flight conditions, hypersonic combustors, and thermal protection systems. In fact, accurate characterization of heating loads in such studies is essential to the survivability of aerospace structures operating in harsh conditions. Other applications such as ground testing facilities (shock tunnels, arc jets) and fire and combustion sciences also require quantifying temperatures in adverse environments that preclude the invasive nature of surface instrumentation. As a result, several optical methods not encumbered by the limitations of contact thermometry have evolved as viable measurement techniques.

By definition, an optical temperature measurement is noncontact in nature and thereby uses a remote optical sensor to measure a thermal dependent property intrinsic to the experimental specimen or arrangement in question. This offers several benefits over the common forms of temperature measurements such as thermocouples. Though generally easy to use, thermocouples in high temperature environments can degrade with time and even disintegrate leading to dubious or nonexistent results. In contrast, noncontact thermometry systems eliminate conductive lead losses and offer long term stability under harsh environments. Optical measurements are adaptable to a wide variety of situations and have the advantages of high sensitivity, quick response time, and being unaffected by electromagnetic interference.

The optical measurement technique considered in this thesis involves the use of thermographic phosphors (TPs). This thermometric technique exploits the temperature dependence of phosphor fluorescence to provide a noncontact, emissivity-independent measurement option. The potential utility of using TPs in applied fields depends on two major issues. First, the chosen calibration method of the phosphor to temperature using some recorded response should possess good sensitivity and be highly repeatable in the laboratory. Second, the calibration method must be easily applied to resolve transient responses to provide an accurate history of the surface temperature.

1.2 Background and Theory

In a broad sense, a phosphor refers to a material that exhibits luminescence, the phenomenon in which the electronic energy of a substance is excited by some kind of external energy and the excitation energy is given off as light.[1] Research on such compounds has been ongoing since the early 17th century when alchemists accidently synthesized luminescent materials in their quest to produce gold.[2] This study of phosphors has led to many useful devices such as the fluorescent lamp, the cathode ray tube, and color television.[3] Such advancements led the lighting and display industries to provide financial support for the study of such phosphors so that now the fundamental aspects of luminescence are well understood.[4]

The works of Alexander Jablonski culminated in a diagram still used today to explain the basic physical processes of luminescence. The Jablonski energy-level diagram, presented in Fig. 1.2.1, illustrates the energy levels associated with the electronic and vibrational states of a typical photoluminescent molecule. The electron states are arranged vertically by energy and horizontally by electron spin orientation. Each electron state has numerous vibrational levels associated with it.[5] The electron levels are represented by heavy horizontal lines while the vibrational levels are represented by lighter horizontal lines.

Figure 1.2.1 shows the relevant processes that govern molecular luminescence. These key events occur on timescales that are orders of magnitudes apart. Excitation, which is brought about by photon absorption, is very rapid and takes place in about 10^{-14} to 10^{-15} seconds.[5] Upon excitation, the luminescent molecules are promoted to a higher electronic state ($S_0 \rightarrow S_1, S_2$). However, the configuration does not remain excited continually and all excited states decay back to the stable ground state, S_0.[6] The conservation of energy principle dictates that the amount of energy absorbed must be released. This occurs via a combination of deactivation steps. Certain steps, indicated by wavy arrows in Fig. 1.2.1, are radiationless processes. These include vibrational relaxation (an intrastate process), internal conversion ($S_2 \rightarrow S_1$ and $S_1 \rightarrow S_0$), and intersystem crossing ($S_1 \rightarrow T_1$). The remaining steps of fluorescence ($S_1 \rightarrow S_0$) and phosphorescence ($T_1 \rightarrow S_0$) involve the emission of a photon of radiation.[6] Typically fluorescence occurs in 10^{-7} to 10^{-10} seconds whereas the lifetimes of phosphorescence range from 10^{-3} to 10^{0} seconds.[7] The probability of following a certain deactivation route to ground state depends on the physical and environmental features of the luminescent material.[5] Certain features that influence that nature of emission are thermally driven.[2]

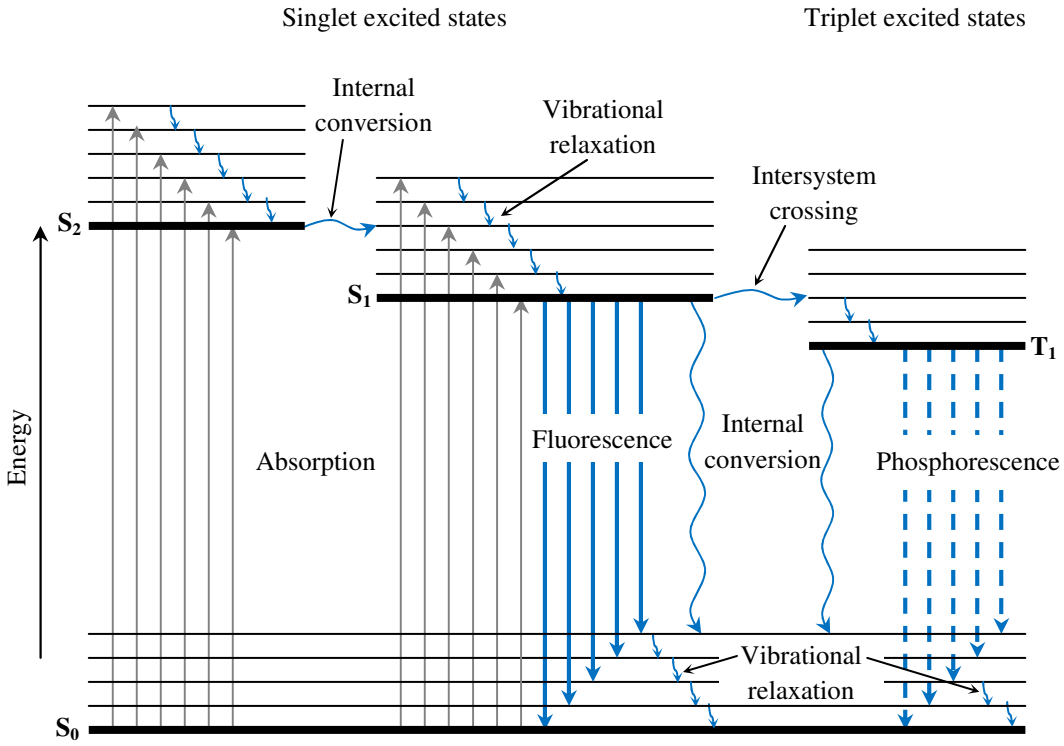

Figure 1.2.1: The Jablonski Diagram

Phosphor thermometry exploits the temperature sensitive properties of luminescence in inorganic phsophors.[2] The first survey of numerous phosphors exhibiting an effective temperature dependence for practical thermometric applications was by Urbach et al.[8] in 1949. In 1952, Bradley[9] then used one such phosphor provided by Urbach to measure the temperature distribution on a flat wedge in a supersonic flow field. Today, the primary materials used in such applications are referred to as thermographic phosphors (TP). These TPs generally consist of two components: a ceramic host and an intentionally added impurity which acts as an activator.[1] It is this impurity, termed the dopant, from which the luminescence originates. For example, the host compound Al_2O_3 is a standard, transparent powder until the metal ion Cr^{3+} is added. The substance then becomes red and fluoresces when irradiated.[4] A TP is specifically designed to fluoresce efficiently in the visible band of the spectrum in the presence of a pulsed excitation source.[4]

During the fluorescence process, the intensity of a transition from one quantum state to another depends on various principles and selection rules of quantum mechanics and the Boltzmann distribution. These laws that govern

the fundamental aspects of fluorescence are typically dependent on temperature. Thus, there is a corresponding temperature dependence that manifests in the spectral and temporal behavior of TPs.[4] These behaviors can be introduced with the aid of the configurational coordinate diagram seen in Fig. 1.2.2. The configurational coordinate diagram shows the potential curves of the luminescent center in the crystal lattice as a function of the configuration coordinate (deviation from the ion equilibrium distance). In Fig. 1.2.2, the parabolic wells represent the total energy of the molecule in its ground or excited state.[10] The vibrational states associated with both electron levels are represented by light horizontal lines.

Similar to the Jablonski diagram, in optical absorption the electrons are promoted from the ground state to the excited state. After excitation the atom usually occupies an upper vibrational level of the excited state (B) and subsequently falls down to the ground vibrational level of the excited state (C). This vibrational relaxation process involves the release of phonons in the form of heat energy. Following radiative emission, the electron reaches a high vibrational state of the ground state (D). The atom further loses energy by the release of phonons so that it can relax to ground state equilibrium (A).[2] From the diagram, it follows that the emission energy is less than that of excitation. Thus, the emission will be shifted to longer wavelengths relative to those of excitation according to Planck's equation[6]

$$E = \frac{hc_L}{\lambda_e}, \tag{1.2.1}$$

where E represents the energy of emission, c_L represents the speed of light, and λ_e is the emission wavelength. This fundamental characteristic of luminescence was first illustrated in 1852 by Stokes and is now known as Stokes shift.[2]

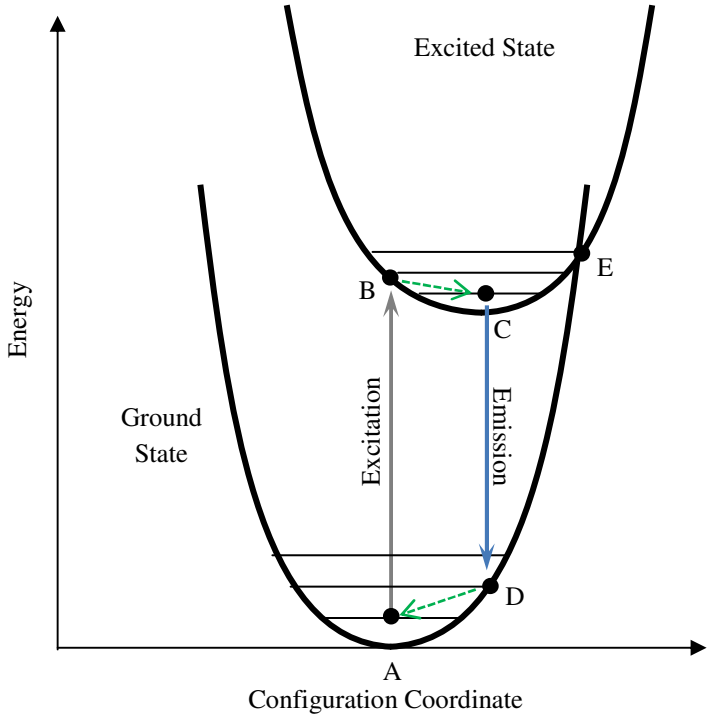

Figure 1.2.2: The Configurational Coordinate Diagram

The previous process describes luminescence originating from the TP dopant for the ideal situation of 0 K. At temperatures above 0 K, however, the entire electron population does not singly occupy the lowest possible vibrational level at equilibrium but is instead distributed over the various vibrational levels following Boltzmann's law[11]

$$\frac{n^*_{excited}}{n^*_{ground}} = e^{-\Delta E/kT}, \tag{1.2.2}$$

where $n^*_{excited}$ and n^*_{ground} is the electron population of the excited and ground state respectively and ΔE is the energy gap between the states. As the temperature increases, electrons can populate the excited state vibrational levels close to the intersection of the two parabolic curves (point E in Fig. 1.2.2). This increases the probability that electrons will change from a vibrational level of the excited state to a vibrational level of the ground state. Relaxation of electrons into the ground state occurs non-radiatively. Thus, fewer electrons participate in the radiative transmission and the intensity of the observed luminescence decreases. Also at elevated temperatures, the electrons are spread vertically over a number of vibrational levels in the excited state. This results in radiation emissions of a photon at different emission energy levels. This contributes to broadening of the emission lines.[2]

Though the previous temperature dependent features are typical of luminescent centers in host materials, there are molecular structures that make certain activators more ideal than others. This stems from the fact that it is the interaction of the host lattice with the activator that influences the temperature measuring properties of TPs.[12] Rare-earth ions (lanthanides) are now widely used in phosphor thermometry as dopants in various hosts. They possess ideal optical properties that derive from their unique electronic structure.[2,11,12]

Lanthanides are characterized by an incomplete 4f shell that is shielded from the effects of the host crystalline structure by the outer 5s and 5p shells of electrons. In small concentrations, the 4f levels of the rare earth ion remain isolated from the host compound and can be treated as a free ion. Thus, the gross features of the energy levels of these activators in different hosts remain almost unchanged.[11] An extensive investigation of this can be found at Dieke and Crosswhite.[13]

Temperature may affect the spectrum of rare-earth ions in several ways. As previously described, increasing temperatures causes the number of upper vibrational levels that become populated with electrons to increase according to Eq. (1.2.2). This causes more electrons to relax to ground state via non-radiative transitions so that the subsequent luminescence intensity decreases.[14] This effect can be seen through the comparison of the emission spectra of $LuPO_4$:Dy,Eu presented in Fig. 1.2.3. Allison et al.[15] illustrate that for excitation at 353 nm, the intensities of the emission lines near 484 and 575 nm are temperature dependent. At elevated temperatures, the rapid decrease of intensity becomes less dramatic. This indicates that the selected emission line is losing sensitivity to temperature change. At a certain temperature value, this sensitivity drops off completely and not trend in intensity change in perceptible. This method of temperature dependence is known as the intensity ratio technique. Using this technique, the relative emission intensity of $LuPO_4$:Dy,Eu can be plotted as a function of temperature as in Fig. 1.2.4.

An emission line shift is another spectral characteristic that exhibits temperature dependence. These shifts are usually attributed to interactions between the rare-earth ion electron states and the lattice vibrations.[16] For an individual phosphor there exists an emission line of a characteristic wavelength where the intensity is maximum. The shift of this maximum emission intensity to an emission line of a different characteristic wavelength is termed a fluorescence line shift.[4] Kusama et al.[16] use the line shift method for measuring temperature using a Y_2O_2S:Eu phosphor. As can be observed in Fig. 1.2.5, there is a shift of about 0.2 nm between -15°C and 72°C. In general, however, this particular technique is not often used in TP applications since line shift changes as a function of temperature are generally small.[4]

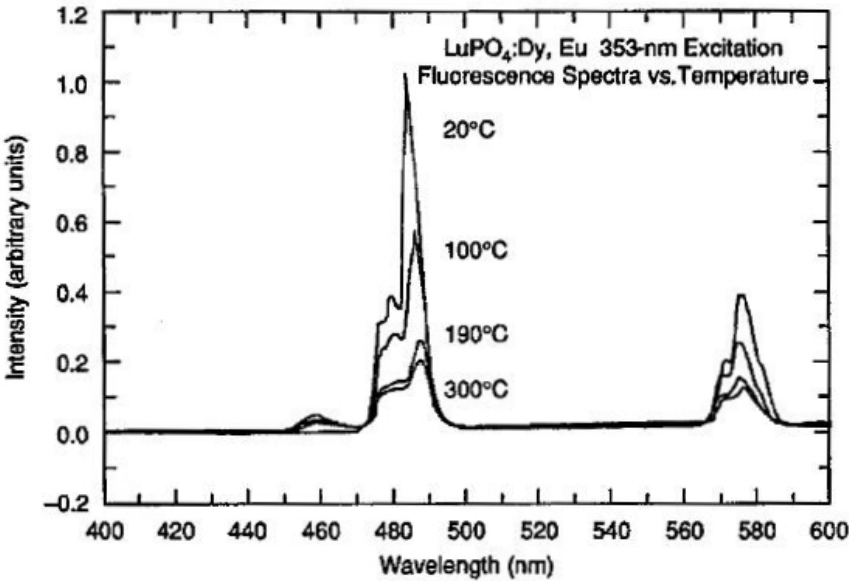

Figure 1.2.3: Temperature Dependence of $LuPO_4$:Dy,Eu emission spectra[15]

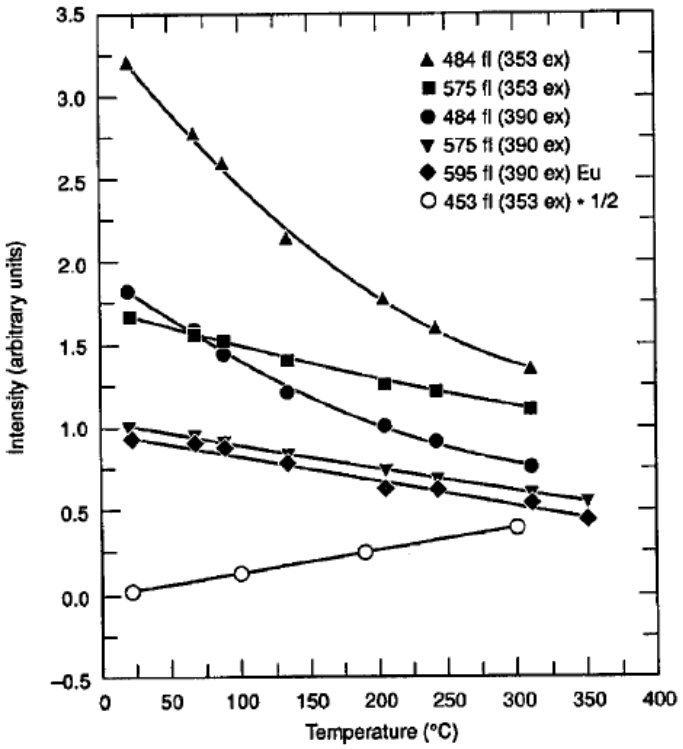

Figure 1.2.4: Relative Intensity Against Temperature for Several of the Pertinent Spectral Lines of $LuPO_4$Dy:Eu (fl, Fluorescence; ex, Excitation)[15]

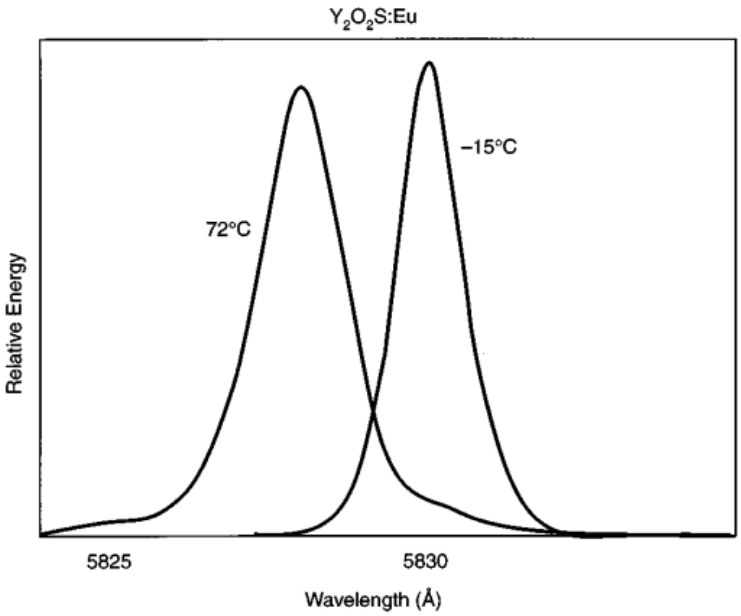

Figure 1.2.5: Line Shift Variation with Temperature for Y_2O_2S:Eu[16]

The most commonly noted temperature dependent property of TPs is the fluorescent lifetime. After radiation is absorbed, the spectral intensity of the emission decays in an exponential manner with a certain decay time that corresponds to a temperature value in a certain temperature range. A TP exhibits good sensitivity to temperature in a certain range.[4] This is demonstrated in the Choy et al.[17] results for the lifetime decay of the 611 nm emission line of Y_2O_3:Eu monitored at three different temperatures. As can be seen in Fig. 1.2.6, the lifetime decay decreases with increasing temperature. This occurs since as the temperature increases, the vibration of the crystal lattice (phonons) nonradiatively relaxes the excited electronic state. Thus, the lifetime of the radiative transition is reduced.[14] This particular phenomena will be discussed in more detail in Chapter 2.

The emission qualities previously discussed are quantifiable properties that can be measured in an experimental setting. It is then possible to use these observed changes in either the spectral or temporal behavior of a TP to calibrate with temperature. This validates that thermographic phosphors can be used as an optical thermometry system.

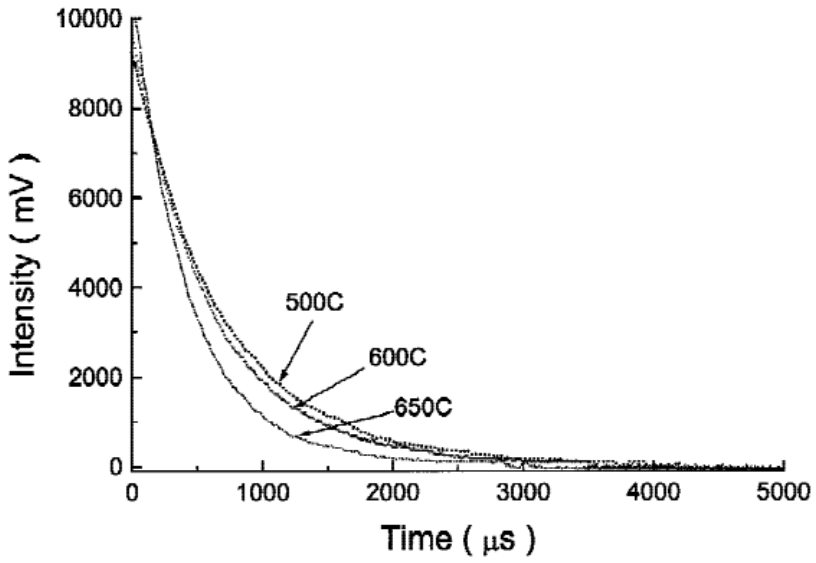

Figure 1.2.6: Temperature Variation of the Lifetime Decay of Y_2O_3:Eu[17]

1.3 Purpose and Organization of Thesis

This thesis provides an alternative approach that is intended to improve the current TP time constant calibration method for temperature recovery. The proposed approach retains the pulsed source input used in the standard TP time constant calibration practice but reinterprets the phosphor response at a fixed distance such that the single-exponential decay assumption is removed. For this new concept, no rigorous data reduction algorithms are needed because it does not rely on fitting an analytical waveform to the decaying luminescence signal. Also, knowledge of key parameters is not needed prior to data processing. The new approach integrates the full phosphor response signal to arrive at a single value related to the integrated intensity trajectory. This value can be calibrated to temperature. The raw collected intensity data can be used without digital filtering since integration is a naturally smoothing process.

In Chapter 2, the approaches to both the traditional TP calibration and the alternative method will be introduced. A first-order model used to describe the released emission will be derived from the physical processes of luminescence. Then the relative challenges associated with using this method to resolve the decay time of the emission will be presented. On the other hand, it will be shown that the alternative calibration techniques are based

on experimental observations so that the restrictive model is removed. The process of obtaining the calibration value from the integrated intensity response will be thoroughly explained for each method.

Chapter 3 will present the experimental set up and procedure used to validate the calibration techniques. The steady-state and transient experiments will be described. Chapter 4 will detail the experimental results. It is shown that the steady-state results for both the alternative techniques can be used as a calibration scheme to resolve the temporal history of a test sample. Finally, Chapter 5 provides some conclusions and possible applications of this research.

Chapter 2: Thermographical Phosphor Calibration

2.1 Traditional Calibration of TP

As previously established in Chapter 1, there are multiple physical properties related to thermographic phosphor emission that exhibit temperature dependence. Such properties include emission wavelength, fluorescence intensity, and decay rate. Any particular one of these variables may offer the best measurement strategy depending on the given application and data requirements. Presently, the most preferred calibration method adopts a model-based formulation to estimate the fluorescence lifetime. It is a well-established and particularly prevalent technique among several disciplines, i.e. medical applications, electrical machinery, and turbomachinery.[4,18-20] This approach has gained popularity due to advantages that include insensitivity to non-uniform excitation, insensitivity to dye concentrations/surface curvature/paint and thickness, and a capacity to be used in high ambient light environments.[2]

The method based on the decay mechanism of phosphor emission involves estimating the fluorescence lifetime, τ associated with a first-order model that describes the released emission (spectral intensity), $I(t)$ after the source is removed. The derivation of this first-order model is associated with the physical response of the phosphor excitation by a pulsed source. Upon excitation, a large number of electrons are promoted to a higher electron state. After the cessation of excitation, the electrons return to the ground state via an electron transition pathway.[4] At sufficiently low concentrations, the rare-earth dopant is treated as a free ion. Therefore, the observed luminescence is due only to electron transitions within the activator and can be described according to first-order kinetics.[21] In this case, excited electrons may decay back to the ground state by either a radiative pathway (photon emission) or a non-radiative pathway (phonon release) according to a certain probability distribution. These two processes are mutually exclusive.[22] A simplified model of the deactivation routes can be seen in Fig. 2.1.1.

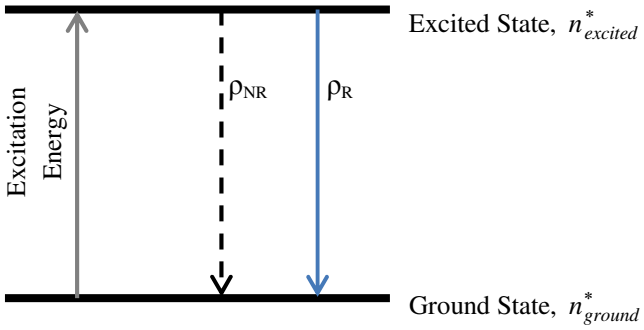

Figure 2.1.1: Simplified Model of Competing Deactivation Routes

For the two-level system, such as presented in Fig. 2.1.1, the rate of change of excited luminescence centers in a unit volume, n^* during the electron population transition from an emitting state to a ground state can be expressed by the sum of a constant, purely radiative component, ρ_R, and a non-radiative component, ρ_{NR}, such that[1]

$$\frac{dn^*}{dt} = -(\rho_R + \rho_{NR})n^*(t), \quad t \geq t', \tag{2.1.1a}$$

subject to the initial condition

$$n^*(t') = n_0^*, \tag{2.1.1b}$$

where $\rho_{NR} \geq 0$, $\rho_R \geq 0$, and $n_0^* \geq 0$. Equation (2.1.1) describes the decrease in excited molecules at all further times. Note that the negative sign indicates emission. The solution to the first-order linear ODE seen in Eq. (2.1.1) is then[1]

$$n^*(t) = n_0^* e^{-(\rho_R+\rho_{NR})(t-t')}, \quad t \geq t', \tag{2.1.2}$$

where n_0^* represents the number of excited luminescence centers at time $t = t'$, the end time of excitation. Stating that the decay rate, κ denotes the rate of transitions per molecule per unit time and is made up of all deexcitation processes such that

$$\kappa = \rho_R + \rho_{NR}, \tag{2.1.3}$$

permits Eq. (2.1.2) to be expressed as

$$n^*(t) = n_0^* e^{-\kappa(t-t')},\ t \geq t'. \tag{2.1.4}$$

Therefore, the mean lifetime or time constant, τ that describes the average amount of time an electron remains in an excited state can be calculated by

$$\tau = \frac{1}{\kappa} = \left(\rho_R + \rho_{NR}\right)^{-1} \geq 0. \tag{2.1.5}$$

The lifetime indicates the time duration for the number of excited molecules to decay to e^{-1} or 36.8%[23] of the original population according to

$$\frac{n^*(t)}{n_0^*} = e^{-(t-t')/\tau},\ t \geq t'. \tag{2.1.6}$$

Under certain conditions the lifetime, τ, shows an appreciable dependence on temperature. The explanation for this lies in the competition between the deexcitation pathways. The radiative transition rate, ρ_R, is temperature independent whereas the non-radiative transition, ρ_{NR}, is highly temperature dependent.[24] As the temperature increases, the probability that an energy state will depopulate via non-radiative decays increases. This kind of process is referred to as phonon quenching and results in a decrease in fluorescence efficiency (quantum yield).[11] At a given temperature, the two transition rates can be related using the quantum yield equation[1] where

$$\phi = \frac{\rho_R}{\rho_R + \rho_{NR}} \geq 0. \tag{2.1.7}$$

Since the radiative transfer rate is known to be a constant, it is also assumed that the radiation lifetime is a constant[2] so that

$$\tau_R = \rho_R^{-1}. \tag{2.1.8}$$

Combining Eq. (2.1.5) with Eqs. (2.1.7) and (2.1.8) yields

$$\phi = \frac{\rho_R}{\rho_R + \rho_{NR}} = \frac{\tau}{\tau_R}. \tag{2.1.9}$$

Therefore, it can be seen that quantum yield is proportional to fluorescence lifetime τ. Increases in temperature lead to increases in radiationless energy transfer. This increases ρ_{NR} and subsequently decreases τ and ϕ.

In a fluorescence experiment, the number of excited molecules is not observed, but rather the fluorescence intensity. Therefore, it is necessary to develop an expression associated with the quantifiable and observable property of emission. The intensity of emission at any instant $I(t)$ is proportional to the rate of change of excited luminescence centers, $n^*(t)$.[24] Hence,

$$I(t) = -C\frac{dn^*}{dt}(t), \ t \geq t', \tag{2.1.10}$$

where C is the constant of proportionality. By manipulating Eqs. (2.1.1-2.1.5), Eq. (2.1.10) becomes

$$I(t) = \frac{C}{\tau} n^*(t), \ t \geq t'. \tag{2.1.11}$$

Evaluating Eq. (2.1.11) at $t = t'$ yields

$$I(t) = I_0 e^{-(t-t')/\tau}, \ t \geq t', \tag{2.1.12}$$

where I_0 is the intensity at time $t = t'$. The physical representation of Eq. (2.1.12) can be seen in Fig. 2.1.2. Once excited by a pulsed source, the phosphor emission decays from $I(t-t') = I_0$ at $t = t'$ to $I(t-t') = 0$ as a result of the competing deexcitation pathways previously indicated in Fig. 2.1.1.

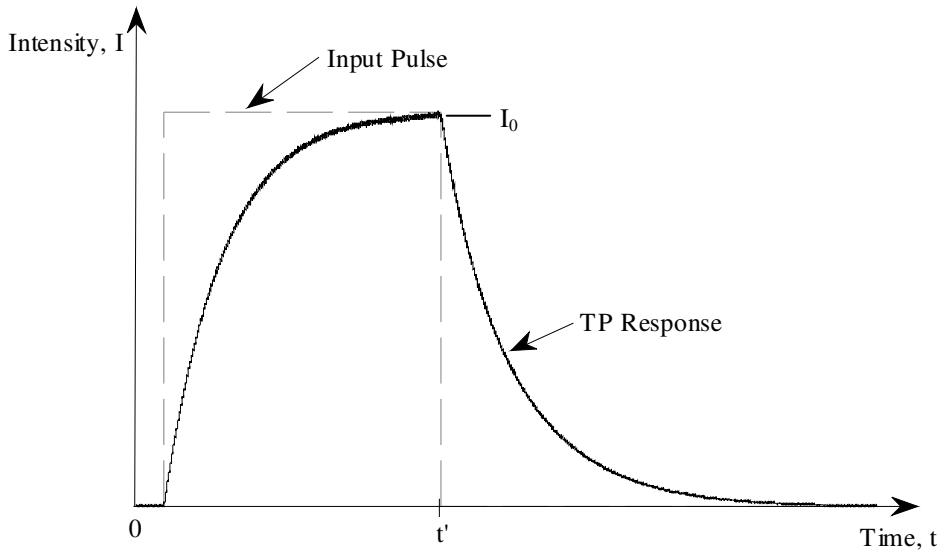

Figure 2.1.2: TP Response to Pulsed Excitation Source

Equation (2.1.12) represents the mathematical model of an ideal exponential decay associated with perfect experimental data and a first-order system, $t \geq t'$. In reality, experimental results possess errors caused by instrumentation and techniques employed in data analysis. Instrumentation errors may be random, such as the PMT shot noise[25], or systematic, such as in oscilloscope timebase distortion[26]. These issues affect how accurately the measurement system is able to characterize the true phosphor emission. Therefore, the measured signal deviates from the ideal behavior detailed in Eq. (2.1.12). The parameters t' and I_0 now become difficult to define in the signal-decay region of the collected emission. Thus, curve fitting an analytical waveform to the entire emission decay with a mono-exponential approach becomes more challenging.

Current work with TPs often rectifies the issues associated with nonideal experimental data by employing a predefined fitting window to the analysis. This involves choosing only a segment of the phosphor emission signal for analysis in determining the decay time. Often a certain percentage of the initial portion of the decay is unused due to the effects of light leakage, other short lived fluorescent states of the phosphor, fluorescence from binder to substrate, and/or other phenomena.[27] However, if too large of a percentage is cut off then the portion of data used in analysis has a low signal-to-noise ratio. This can also cause problems. The choice of this percentage is an arbitrary

guessing game and generally is not able to remain a constant value since the dynamic range of the decay characteristics of TPs often exceeds more than three orders of magnitude.[28] This can lead to a lack of unity in the calibration results for a given phosphor.

Other options for resolving τ in order to calibrate with temperature usually involve rigorous data algorithms. For example, Eq. (2.1.12) can be transformed into

$$I(t) = I_0 e^{-(t-t')/\tau} + I_{offset},\ t \geq t', \tag{2.1.13}$$

where I_{offset} is the baseline offset. After the mean value of the respective waveform's intensity prior to an excitation pulse has been subtracted from the signal, the Levenberg-Marquardt algorithm, Prony's method, or a Monte-Carlo simulation could be used to iteratively resolve I_0 and τ using a certain abort criterion.[28-31] Others have gone a step further and transformed Eq. (2.1.12) to

$$I(t) = I_0 e^{-(t-t')/\tau} + \varepsilon(t) + I_{offset},\ t \geq t', \tag{2.1.14}$$

where $\varepsilon(t)$ is the noise component attributed to the various noise sources. In this case, the previously mentioned methods must be used to iteratively resolve I_0, τ, and $\varepsilon(t)$ after the baseline offset has been subtracted from the signal.[30] Finally, additional physical issues can also arise in using lifetime estimation for temperature calibration since not all phosphors obey a mono-exponential decay emission.

It is already known that the favored deactivation route of excited electrons to the stable ground state is the one that minimizes the lifetime of the excited state.[5] As the temperature increases, electrons are promoted to higher vibrational levels of the excited state, and there is a higher probability that non-radiative energy transfer will occur. The deactivation rate of fluorescence (10^{-6} s) no longer effectively competes with the kinetic rate associated with phonon release (10^{-15} s). This is the main principle behind the thermal quenching of TP fluorescence. Previous discussion assumes that interactions between the dopant activator and host crystal lattice have a negligible effect on the luminescence physics in TPs. At increased dopant concentrations, however, this assumption breaks down because the lanthanide is more strongly coupled to the host lattice. This causes another nonradiative deexcitation

pathway stemming from ion-lattice interactions to become more important.[4] At this point, the first-order kinetic model no longer applies. As multi-phonon relaxation becomes more probable, the effects of phonon quenching become even stronger. This leads to a change in the exponential nature of the emission.[32-34] The lifetime of the emitting state still possesses temperature sensitivity; however, it can manifest in bi- and multi-exponential fluorescence decay profiles. This requires the iterative resolution of the following linear combination of exponential functions possessing different time constants, as

$$I(t) = \sum_{i=1}^{M} I_i e^{-(t-t')/\tau_i} + \varepsilon(t), \;\; t \geq t', \tag{2.1.15}$$

where I_i are the initial separate fluorescence amplitudes and τ_i are the corresponding fluorescence lifetimes. In Eq. (2.1.15), there are M separate fluorescent decays present in the signal.[30] Unlike Eq. (2.1.12), which is the solution of a first principle derivation, Eq. (2.1.15) is a model based on physical system responses. This idea is illustrated by the TP emission signal presented in Fig. 2.1.3. The time axis has been shifted according to $\bar{t}(i) = t' - t(i)$ so that the end time of excitation occurs at time $\bar{t} = 0$. As can be observed in Fig. 2.1.3, the decay does not display single exponential behavior and is in fact better characterized using the bi-exponential model. The double exponential consists of a fast decay portion at the beginning of the fluorescence profile (low data density region) and subsequently moves to a long decay portion that is usually used in lifetime-temperature measurements.[22] This introduces further complexities into the lifetime curve-fitting algorithms. The proper optimization techniques must be employed so that there is a compromise in estimation accuracy of both decay counterparts.[24]

The complicated numerical schemes needed to resolve Eqs. (2.1.13)-(2.1.15) require large computation times and can be difficult to implement. Thus, a new, less complicated TP calibration concept could be proposed for certain applications.

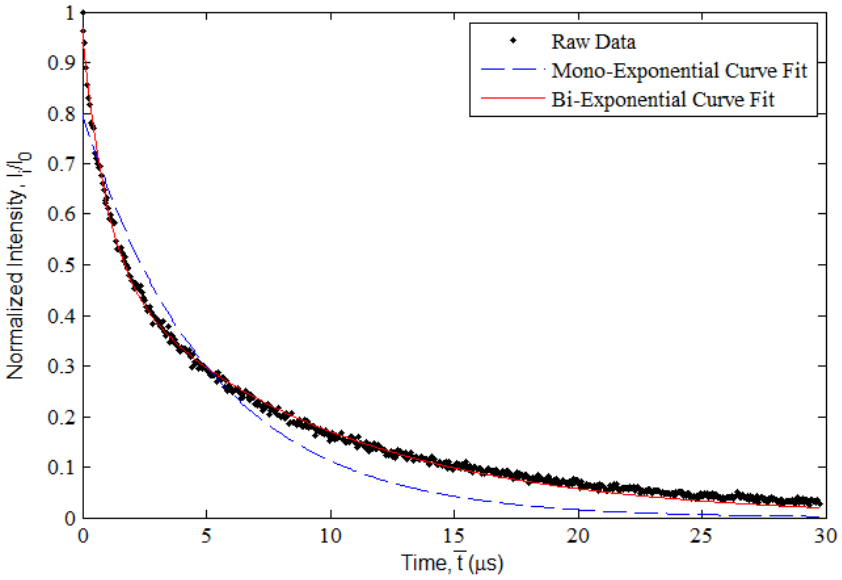

Figure 2.1.3: Curve Fitting a Multi-Exponential Decay Profile

2.2 New Concept for Calibration of TP

A. Development of Technique – Investigation into Phosphor Emission Behavior

Phase-plane techniques are used to provide physical insight into complex systems.[32-38] It has been applied across many scientific fields, such as neuroscience[39], quantum mechanics[40] and mechanical systems[41], to extract qualitative information about the characteristic system in terms of steady-state behaviors, stability and transient properties.[42] Similarly, the concept was applied in this work to study the complex dynamical system of phosphor fluorescence. A phase portrait was constructed to visualize the evolution of emission behavior in time and to observe possible areas of temperature dependence. In the phase portrait, each curve represents the fluorescence trajectory of the phosphor at a different thermal state.

The first investigation into phosphor emission behavior was done by analyzing Fig. 2.2.1, the first-order phase plane portrait involving $\frac{dI}{dt}(t)$ and $I(t)$. Prior to numerical differentiation, digital filtering of $I(t) \cong I_f(t)$ is done using a moving low-pass Gauss filter. This filtering process utilizes a cut-off frequency to remove bothersome high frequency content from the signal. It also generates a new continuous function that can be resampled at discrete time steps. More information about the filtering method can be found at Frankel et al.[43] The

first derivative of the filtered intensity response is evaluated by a straightforward finite difference method. As can be observed in the phase portrait, there are regions that display temperature sensitivity. The bottom portion of Fig. 2.2.1, which corresponds to the rising intensity portion of the TP as it is being irradiated by light, exhibits a change in curvature. The differentiated intensity trajectory slopes down to a distribution of distinct minimum vales. As the temperature increases, the intensity corresponding to the given minimum decreases. An interesting feature to note is that this temperature sensitivity is not reciprocated at the phase portrait maximum as shown in the upper portion of Fig. 2.2.1.

Though the phase plane portrait does display temperature dependent features, it does not offer an ideal alternative to the traditional method of TP calibration. Numerical differentiation is an inherently unstable process that amplifies perturbations in the tabulated data of the original function. To reduce these ill-posed effects, which are even further exasperated in the presence of experimental data, it is necessary to only differentiate the filtered intensity response, $I_f(t)$. However, digital filtering methods can adversely affect the physics of the original input signal and result in a loss of usable data. Furthermore, it makes the selection of new parameters, such as cut-off frequency and filter influence region, necessary during post-processing. In essence, the key parameters needed during traditional TP calibration are traded for others. Thus, an alternate calibration approach using values of the differentiated filter intensity response may not improve the complexity or large computation times required in the traditional scheme.

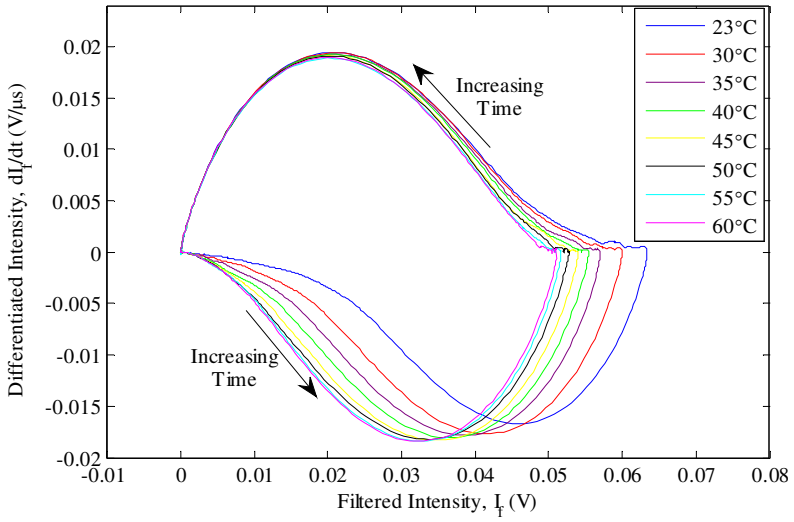

Figure 2.2.1: The Phase Plane Portrait

A second investigation into phosphor emission behavior was done by analyzing Figure 2.2.2, the integrated phase plane portrait involving $\int_{u=\gamma}^{t} I(u)du$, denoted by $\Psi(t)$, and $I(t)$. Here, γ represents the starting time of the fluorescence process. Direct integration of the intensity response, $I(t)$, is done using the rectangular rule. No pre-conditioning is necessary. As can be observed from the integrated phase portrait, there are two regions that exhibit temperature dependence and can be exploited for calibration. The first calibration region corresponds to the largest intensity portion of the fluorescence signal for each temperature curve. This segment, which occurs directly prior to the end time of the excitation pulse, was chosen because it takes advantage of data with a high signal-to-noise ratio. The second calibration region was chosen because it occurs at the highest integrated intensity value for each temperature curve. The total integral of the phosphor response, denoted by Ψ_T, encompasses all the temperature dependent properties that manifest in the temporal behavior of phosphor emission into a single value.

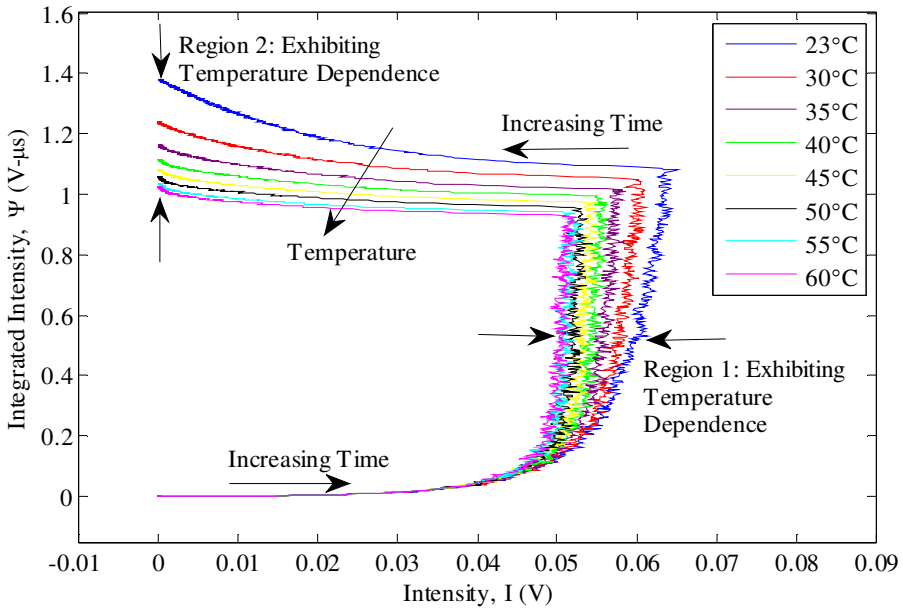

Figure 2.2.2: The Integrated Phase Plane Portrait

B. Slope Calibration

Figure 2.2.3 displays the integrated intensity response in time, $\Psi(t)$, overlaid on the original phosphor intensity response in time, $I(t)$. The vertical lines indicate the segments of each curve that correspond to the first region of temperature dependence previously observed in Figure 2.2.2. The calibration region 1 $I(t)$ segment is located in the rising portion of the luminescent signal prior to decay. It is important to note that using this portion of the intensity response is not an original concept. Investigations of the TP Y_2O_3:Eu has shown that rise time characteristics can be used for calibration.[44] The analysis generally involves fitting an exponential model to the rise portion of the phosphor signal via iterative numerical schemes analogous to those involving emission decay.[2,4,11] However, analyzing the linearity of the indicated $\Psi(t)$ segment suggests that an alternate methodology may be used to investigate the temperature-dependent features of calibration region 1.

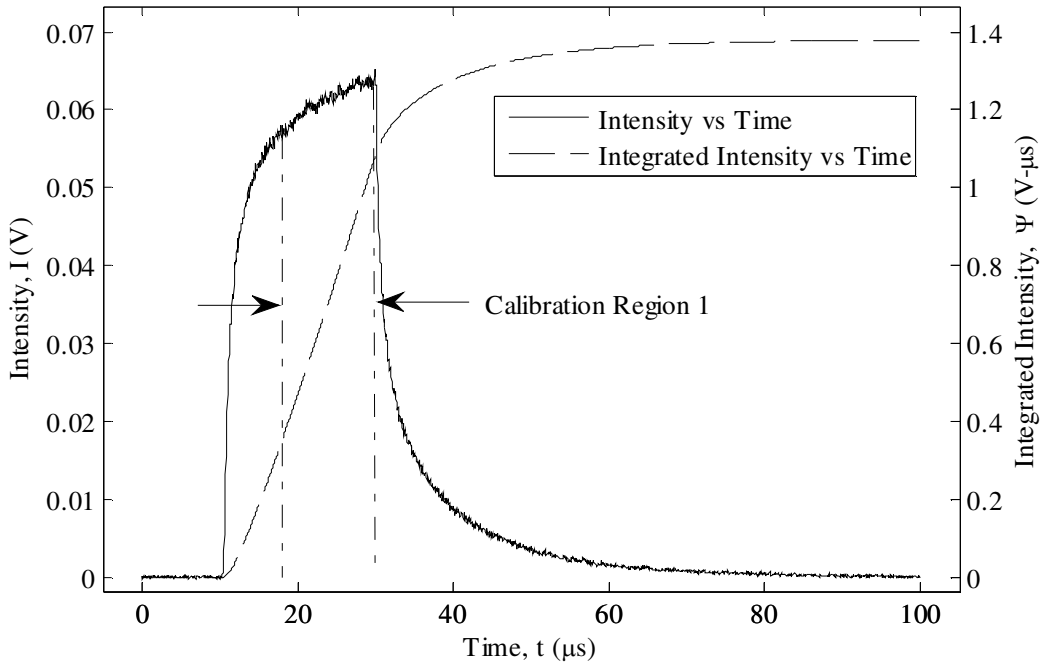

Figure 2.2.3: Integrated Intensity Response Overlaid on Intensity Response

Figure 2.2.4 displays the integrated intensity trajectories in time for $T \in [23°C, 60°C]$. As temperature increases, the integrated intensity portion contained in the calibration region of interest rises to the point corresponding to the maximum intensity value of the raw phosphor emission at a decreasing rate. Also, each distinct segment obeys the linear relationship,

$$\Psi(t) = \eta t + \Psi_{intercept}, \qquad t \in [t_{start}, t_{end}], \tag{2.2.1}$$

where η (V) is the slope of the linear line and $\Psi_{intercept}$ (V-μs) is a constant (the Ψ-intercept). The domain bounds of Eq. (2.2.1), namely $t \in [t_{start}, t_{end}]$, represent the start and end times of the calibration region. This remains fixed throughout the calibration process so that $t_{start} = 18\,\mu s$ and $t_{end} = 30\,\mu s$. For a single temperature the values of η and $\Psi_{intercept}$ are resolved by performing a linear least squares regression on the integrated intensity data within the domain of interest as shown in Fig. 2.2.5. This process is repeated at various steady-state temperatures. The final product of this process is a calibration curve that relates η, the slope of the linear portion of $\Psi(t)$, to temperature. A calibration curve representative of this technique can be seen in Fig. 2.2.6.

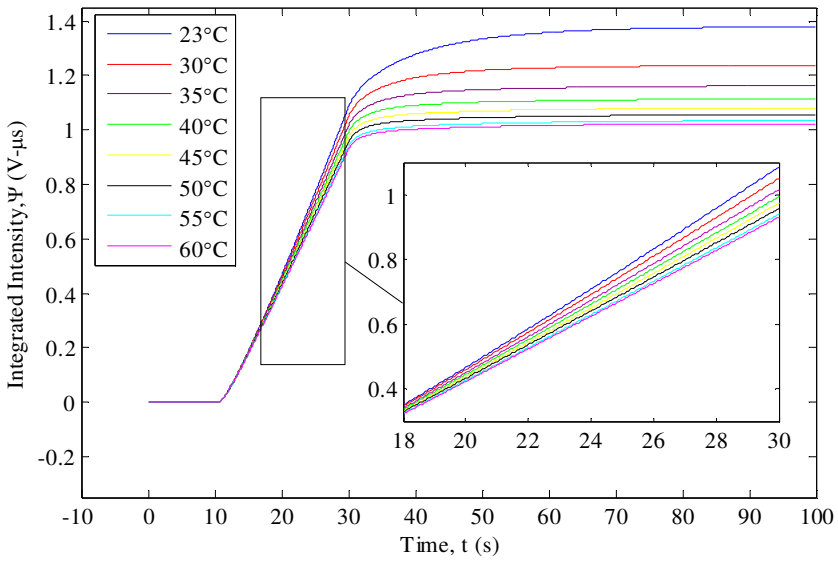

Figure 2.2.4: Integrated Intensity Trajectories in Time for Slope Calibration

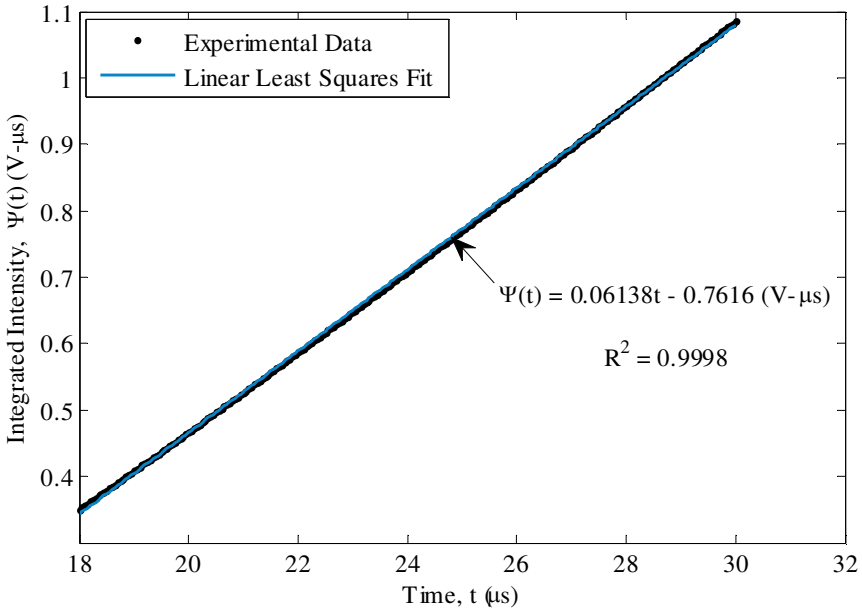

Figure 2.2.5: Linear Least-Squares Regression to Resolve Slope of Integrated Intensity Line

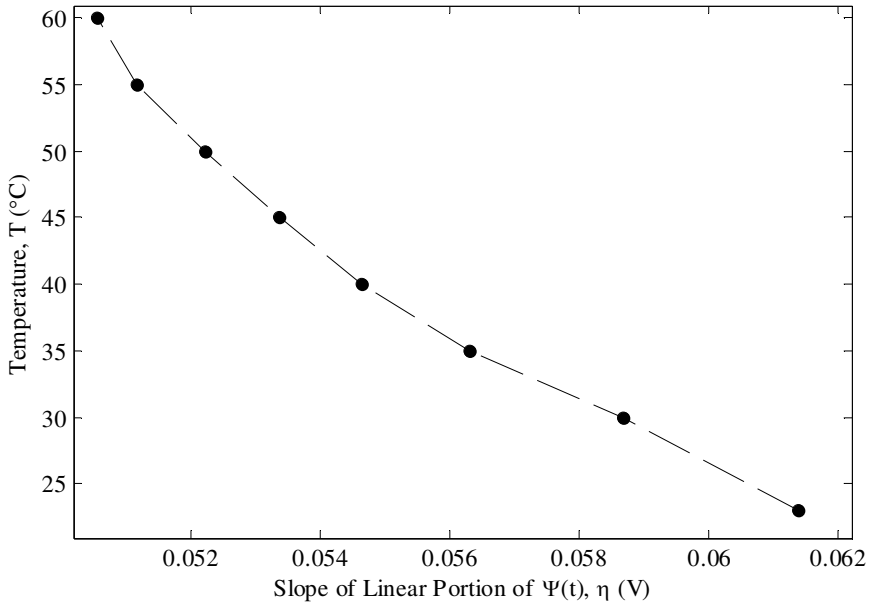

Figure 2.2.6: Calibration Curve Relating Slope to Temperature

C. Total Integral Calibration

Figure 2.2.7 indicates the total integral values taken from the $\Psi(t)$ curves at each steady-state temperature. For each temperature run, the integrated signal remains at approximately zero for about 10 μs. At this point, the phosphor becomes excited and the emission intensity increases to a maximum value. Similarly, the integrating intensity rapidly increases in a linear fashion until this maximum value point is reached at the end of excitation. The phosphor emission signal then decays back down to zero. At the onset of decay, the integrated intensity curve changes concavity. It then levels off to a single integrated intensity value, Ψ_T, which represents the total area under the phosphor emission signal. Since the shape of a distinct phosphor emission is made up by the temperature-dependent rise and decay portions of the signal, it follows that the value of Ψ_T is also temperature-dependent. Therefore, a calibration curve that relates Ψ_T to temperature may be formed. An example of this can be seen in Fig. 2.2.8.

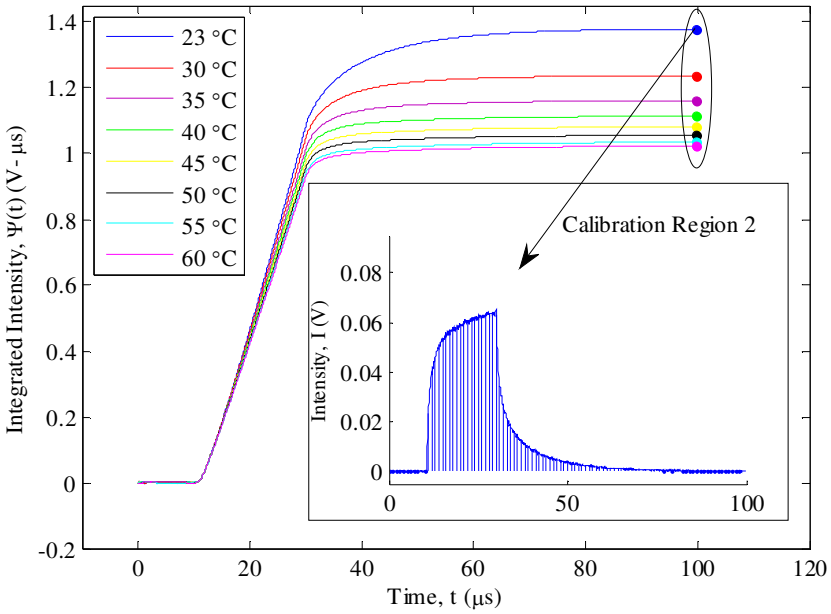

Figure 2.2.7: Description of Total Integral Calibration

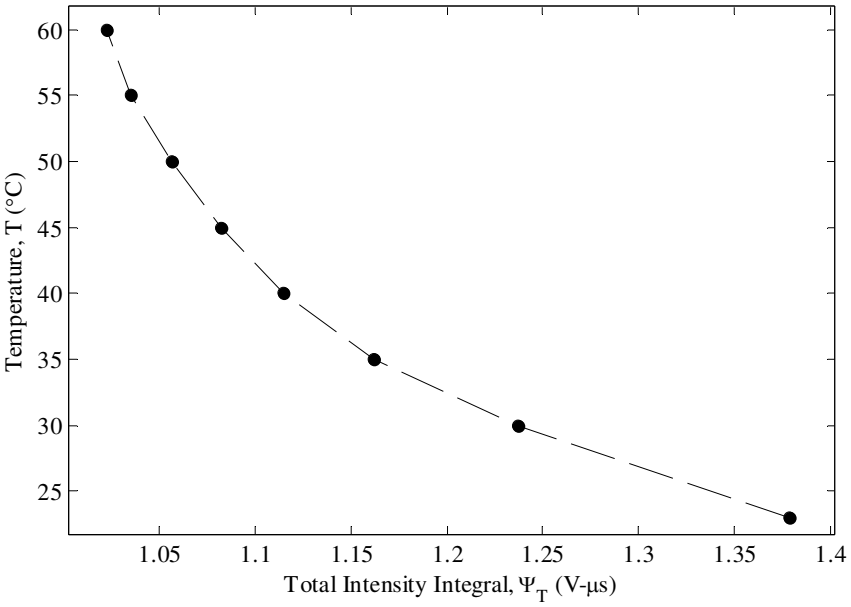

Figure 2.2.8: Calibration Curve Relating Total Intensity Integral to Temperature

Chapter 3: Experimental – Proof of Principle

As previously stated in Chapter 2.2, the integral of the phosphor emission response displays temperature dependent characteristics that may be used as a calibration technique for temperature recovery. However, this technique must be validated by experimental data. In order to do this, the experimental process must be two-fold. First, the phosphor emission response must be recorded at different steady-state temperatures so that the quantity of interest taken from the integrated phosphor signal can be measured under known and repeatable conditions. A calibration curve may then be developed and the uncertainty of the method can be investigated. Second, the phosphor response must be heated under transient conditions so that the calibration technique can be applied to resolve the temporal history of the test sample.

3.1 Experimental Equipment and Wiring

A phosphor-based optical thermometry system is generally made up of the following components: (1) a phosphor coated sample, (2) a means to control the temperature variation of the test material, (3) an alternative means of measuring temperature to provide a known standard that experimental results can be calibrated against, (4) a pulsed excitation source, (5) an optical detector to measure the fluorescence that is generated, and (6) a data acquisition system to monitor and record the phosphor signal.

In this work, the thermographic phosphor La_2O_2S:Eu painted on a 5.08 cm x 5.08 cm x 0.635 cm (2 in x 2 in x 0.25 in) copper plate was used as the test specimen. The phosphor was donated and coated onto the copper material by Emerging Measurements (emco). This was done by mixing the phosphor sample in powder form with water and a ceramic binder, namely VHT FlameProof^{TM} Coating. A thin, even coating was then painted on the clean, dry surface using an airbrush. The copper sample was previously hand-rubbed with sandpaper to give the surface a degree of roughness to which the phosphor coating could adequately bind. Once painted, the copper plate cured at room temperature for twenty-four hours.

During experimentation the copper plate was heated using a 5.08 cm x 5.08 cm (2 in x 2 in) strip heater that was flush against the copper surface. Figure 3.1.1 shows a cross-section of this copper-heater assembly housed in a cavity milled into a PVC substrate. A small hole was drilled into the PVC directly under the heater lead wire exit so that the leads were left exposed. The heater leads were wired to a variable AC power supply which, for the purposes of this experiment, supplied voltage between 0-10 VAC. A surface-mount RTD with self-adhesive backing was

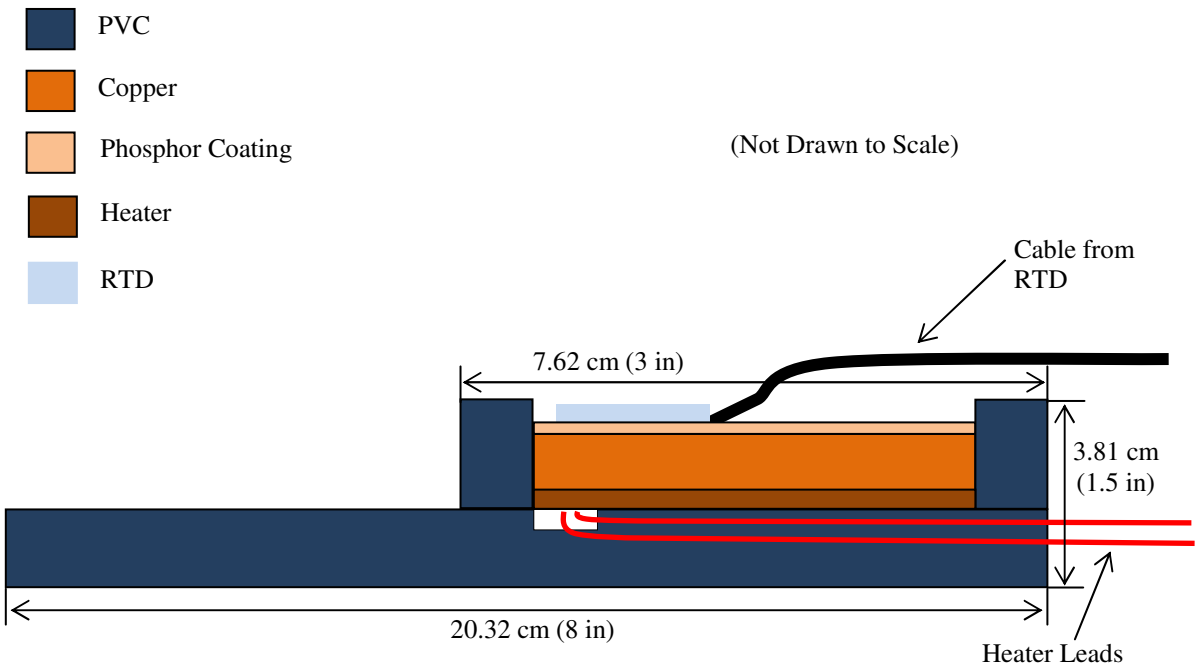

Figure 3.1.1: Cross-Section of Copper and Heater Assembly in PVC Housing

affixed on the phosphor (unheated) surface of the copper sample. Via DIN connector, the RTD sensor was connected to an input thermometer that translates the RTD voltage data to temperature measurements. The RTD meter was then connected to a PC controller for data acquisition.

As previously described from Fig. 3.3.1, the test phosphor La_2O_2S:Eu displays the desired temperature dependence around the 512 nm emission line when exposed to an excitation wavelength of 365 nm. Therefore, the optical excitation and detection components of the experimental arrangement consisted of a 365 nm pulsed LED and a photomultiplier tube (PMT) fitted with a 510 nm optical filter. The optical filter was used to isolate the phosphor emission from stray ambient light or reflection from the LED. Both the LED and PMT were placed inside separate plastic containers. The specific installation and wiring requirements of each instrument was done inside its individual housing. Wiring schematics from the PMT and LED modules can be seen in Fig. 3.1.2 and Fig. 3.1.3.

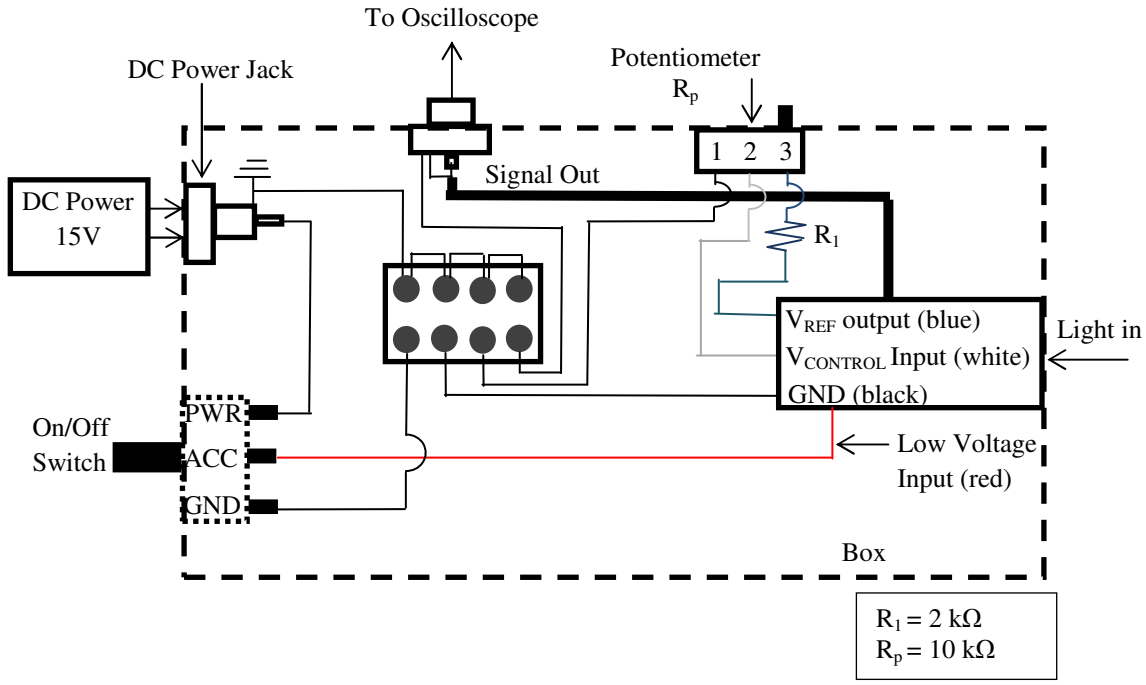

Figure 3.1.2: Experimental Wiring Diagram of PMT

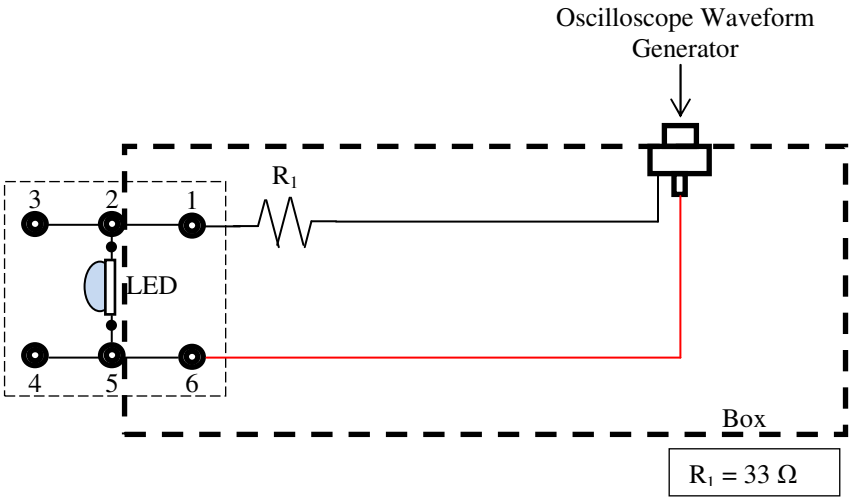

Figure 3.1.3: Experimental Wiring Diagram of LED.

Both the LED and PMT modules were connected to a single oscilloscope. The LED was specifically connected to the oscilloscope's built-in function generator to control the pulse modulation. The PMT was connected to a variable terminator at a 500 Ω setting. This setting of the variable terminator reduced high frequency noise without largely attenuating the fluorescence signal. The variable terminator was connected to the channel 4 input of the oscilloscope. The oscilloscope was connected to the PC controller for data acquisition.

An experimental rig was built to hold the optical instruments, LED and PMT, at a certain height and angle. The height and angle of each instrument could be adjusted as necessary. The rig was made up of 4 vertical posts held together by 4 horizontal posts so that it could be placed over the PVC plate with the copper sample centered in the middle. Figure 3.1.4 shows the first iteration of this concept without the attached optical instruments. Through multiple experimental iterations, it was found that an optimal phosphor fluorescence signal was measured when the PMT viewing window was placed at a minimized height normal to the copper sample. Also, a plano-convex lens was used to collimate the LED light at a target spot on the phosphor. Once the LED and PMT were attached to the experimental rig, the placement of these instruments was not changed throughout the entire experimental process. The complete experimental set up, both rig and PVC plate, were bolted to a wooden table to prevent movement from vibrations or jarring. A picture of the finalized setup can be seen in Fig. 3.1.5. Also, a summary of all equipment used during experimentation can be seen in Table 3.1.1.

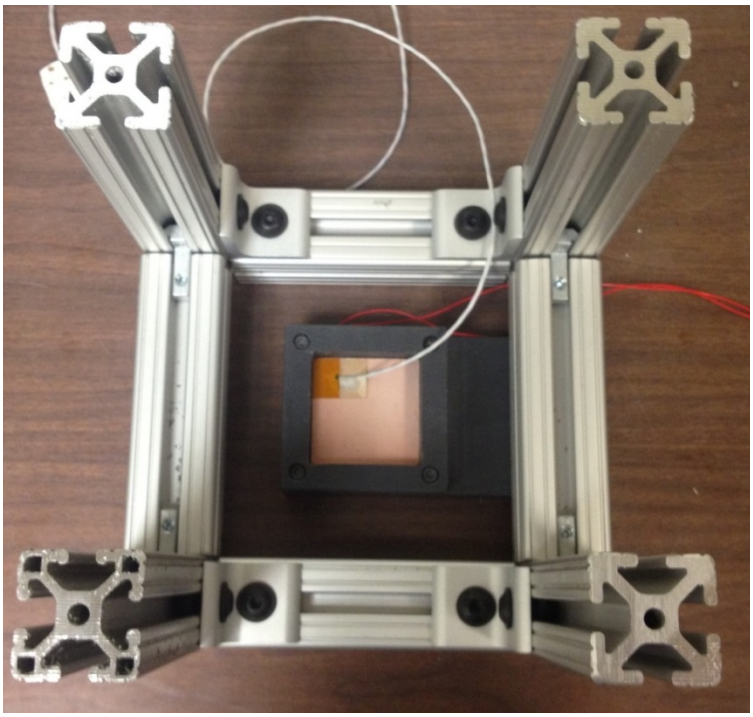

Figure 3.1.4: First Iteration of Experimental Rig Concept (Top Down View)

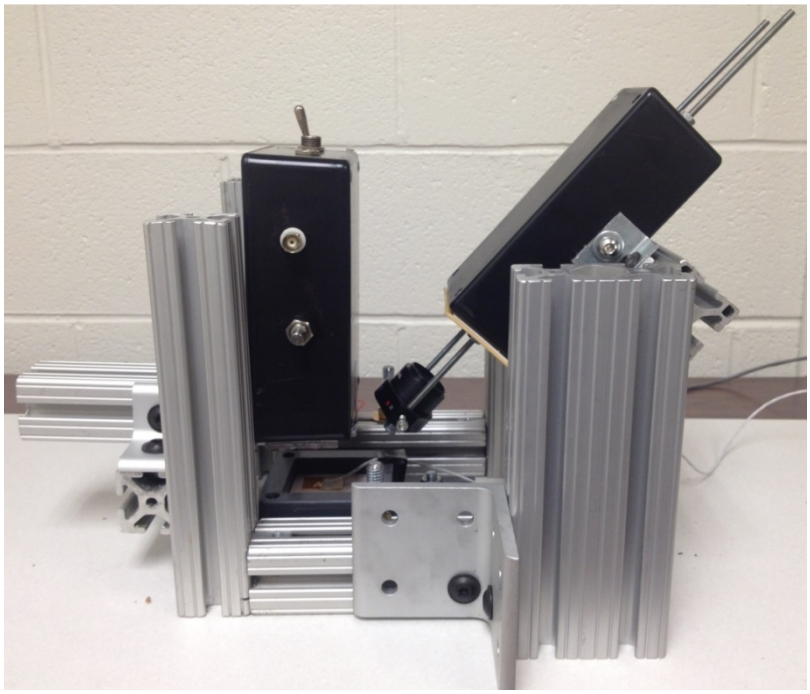

Figure 3.1.5: Finalized Setup of Experimental Rig Used in All Experimentation (Side View)

Table 3.1.1: List of Equipment

Instrument	Description	Purpose
Hamamatsu H5783-01	Photosensor module with spectral range of 300-850nm, 0.78ns rise time	Detection of fluorescence signal
Andover 510FS10-25	510nm (+3/-0nm) optical filter, 10nm (±2nm) bandwidth	Isolation of phosphor emission
LED Engin LZ1-10U600	365nm, 3W UV LED	Excitation of phosphor
Thor Labs LA4052	Plano-convex lens, 35mm focal length	Collimation of LED light
Thor Labs VT1	Step variable terminator	Reduction of high frequency noise in fluorescence signal
Agilent DSOX3034A	4 channel, 350MHz oscilloscope, 8 bit vertical resolution, 2.5ps horizontal resolution	LED modulation; fluorescence signal collection
Omega SA1-RTD	100Ω surface-mount RTD, ±0.06Ω at 0°C, 26AWG cable	Temperature probe
Omega HH804U	RTD input thermometer, 1 Hz, 0.1°C resolution	Temperature measurement
Omega KHLV202	2 in x 2 in Kapton insulated flexible heater, 28V	Variation of test sample temperature
UT AC Power Supply	Variable AC power supply, 115VAC	Heater power supply
ASUSTek U56E Laptop	PC with Visual Studio 2013 and 800 Multi Software	Data acquisition and control

3.2 Experimental Scheme and Data Acquisition

Figure 3.2.1 displays a summary of the general experimental scheme of this work. The experiment was able to be divided into the following: (1) the optical portion regarding the phosphor fluorescence, (2) temperature verification, and (3) temperature modulation. While both the optical and temperature verification portions of the experiment were run with the PC controller, it was necessary to regulate temperature modulation separately.

In the optical arrangement, the PC controller communicated with the oscilloscope over a USB interface. A Visual Studio 2013 C# program, which references the Agilent VISA COM library, opened the connection to the instrument and sent commands remotely so that the process was automated. Via the remote interface, the oscilloscope was first initialized to the state required for an individual experiment. This included clearing the memory buffer and also configuring the oscilloscope to the settings detailed in Table 3.2.1. Once initialized, the oscilloscope would drive the LED at 10 kHz with a 20% duty cycle while simultaneously using the signal derived from this excitation pulse to trigger the acquisition of the fluorescence signals. This coordinated the excitation/detection system to be a synchronous arrangement. During oscilloscope data collection, each captured acquisition of the phosphor emission occurring from a single excitation pulse was averaged together in a "running manner" over the desired number of responses as described in Fig. 3.2.2. In the "shot-averaging" progression, only the newly averaged waveform was displayed and stored in the acquisition memory in the oscilloscope. Shot-averaging was used in rapid succession owing to the small times involved. This contrasts time filtering of data that only requires one shot and low pass filtering to remove noise. The timespan required to capture a single phosphor emission was $\Delta t = 100\mu s.$ Therefore, the total time to obtain the final fluorescence signal, averaged over N waveforms, was $N(\Delta t).$ When the average count was completed, the data was transmitted to the PC controller in byte format. This yielded 8 bits of resolution. The data sent from the oscilloscope was then scaled according to Eqs. (3.2.1) and (3.2.2). The values used to interpret the data (X and Y references, X and Y origins, and X and Y increments) can be found in Table 3.2.2. The time and voltage data of the final waveform was then saved to the PC controller in text file format. These text files contained 2000 data values along with the timestamp corresponding to the start of phosphor emission capture.

$$Time = Xorigin + Xincrement\ (\ Xdata - Xreference\ ) \tag{3.2.1}$$

$$Voltage = Yorigin + Yincremet\ (Ydata - Yreference) \tag{3.2.2}$$

The second portion of the experimental scheme, temperature verification, was run concurrently with the optical portion. The PC controller was connected to the RTD input thermometer over a USB interface. A Windows software program, which was designed to communicate with the meter, triggered temperature readings to be taken by the RTD at a rate of 1 time per second. Each temperature measurement was then transmitted to the PC in real time. At the conclusion of the experiment, all temperature readings and their matching timestamps were saved in a text file format. In post-processing, it was necessary to synchronize the timestamps of each fluorescence signal to that of the temperature readings so that a proper temperature history could be assembled. The final portion of the experiment arrangement, which concerned the temperature modulation of the copper sample, was user-operated. The AC voltage source was adjusted by hand so that the power supplied to the strip heater would bring the copper sample to the desired temperature. Voltage measurements of a given experiment were not recorded.

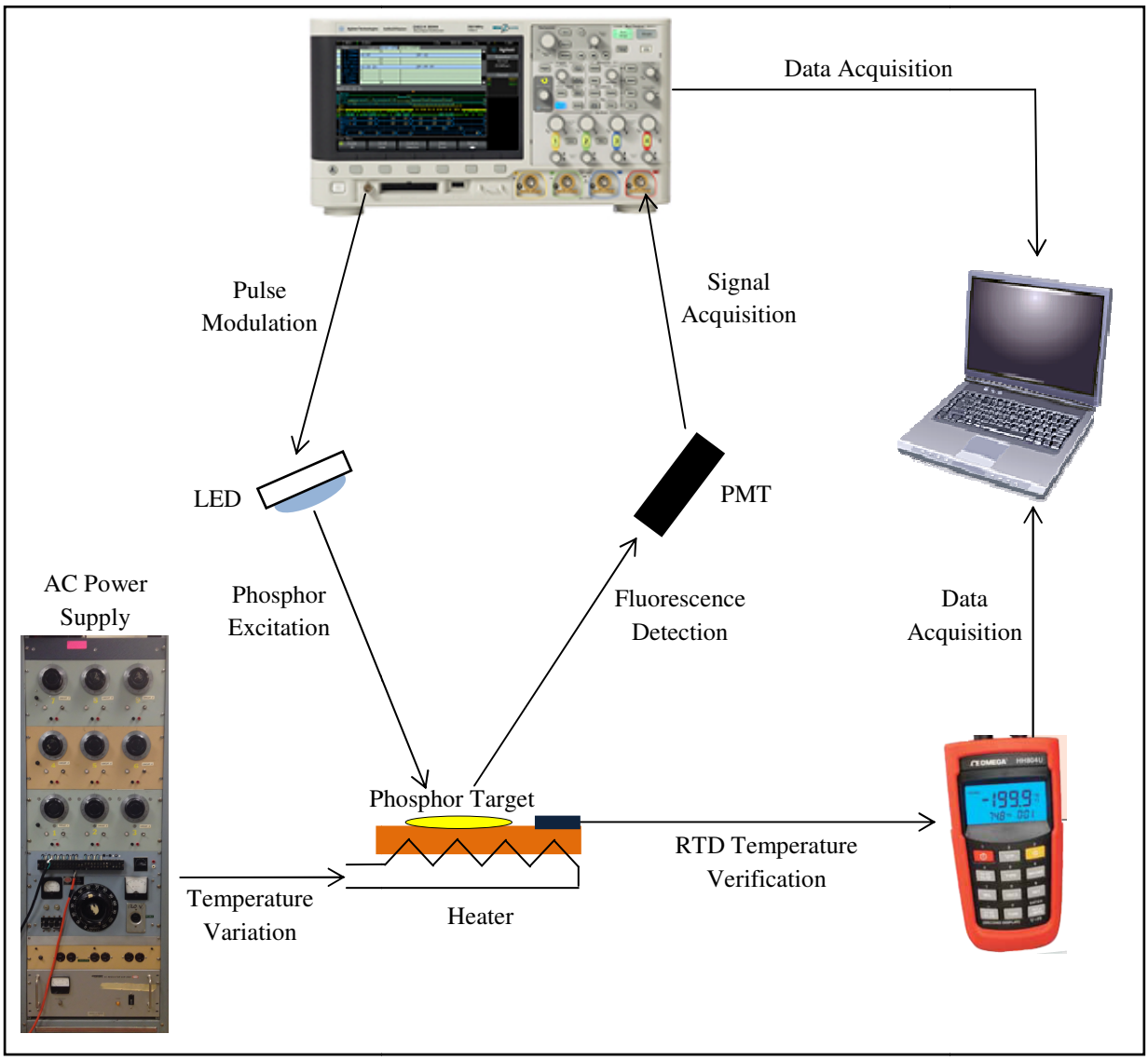

Figure 3.2.1: Summary of Experimental Scheme

Table 3.2.1: Oscilloscope Configuration Settings

Control Category	Configuration Settings
Horizontal	Normal mode, 10 µs/div, 120 µs delay, center time reference
Vertical	Channel 4 on, 10 mV/div, DC coupling, 33 mV position, 1 MΩ impedance, invert on
Waveform Generator	Pulse waveform, 10 kΩ frequency, 5 V high-level, 0 V low-level, 20 µs pulse width
Trigger	Sweep mode normal, DC coupling, 200 ns holdoff, trigger mode edge, source waveform generator, falling edge slope, 1.90 V level
Acquisition	Average mode, number averages {512, 128, 32, 8}, realtime on

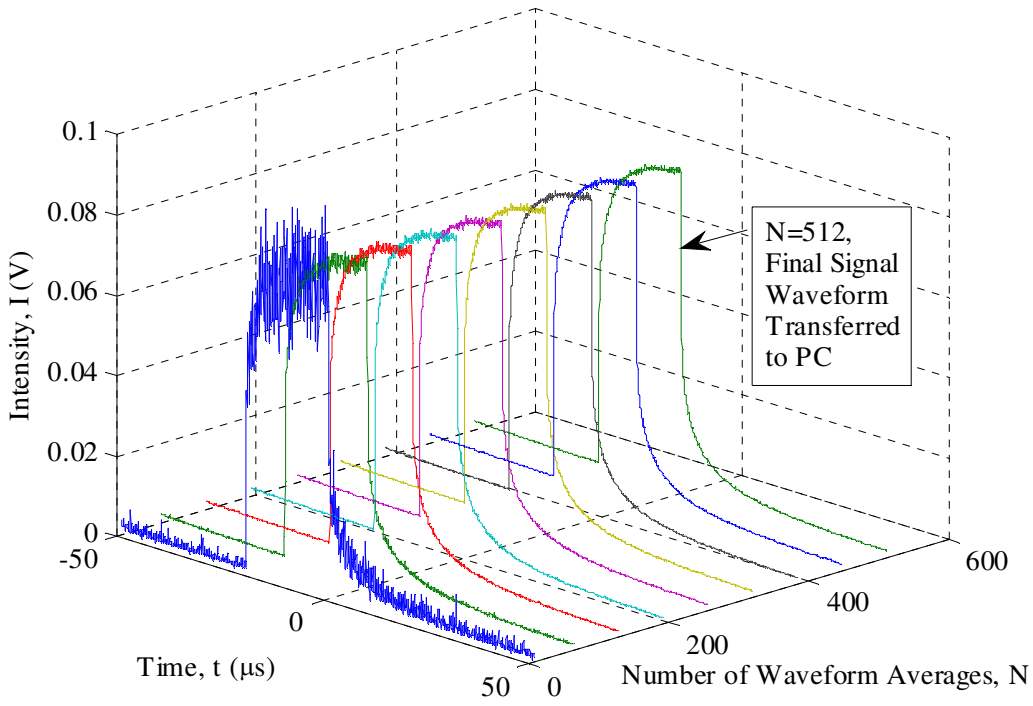

Figure 3.2.2: Graphical Description of Shot-Averaging Progression.

Table 3.2.2: Conversion Values Used to Interpret Waveform Data to Time and Voltage Values

Coefficient	Conversion Value	Unit
Xorigin	$7.000000(10^{-5})$	s
Xreference	0.000000	s
Xincrement	$5.000000(10^{-8})$	s
Yorigin	$3.30000(10^{-2})$	V
Yreference	0.000000	V
Yincrement	$1.570352(10^{-6})$	V

3.3 Experimental Procedure

The procedure for running an experiment was as follows. The connections of all experimental instrumentation were checked. The oscilloscope and RTD input thermometer were turned on and connected to the PC controller via USB cable. The driver programs for each respective instrument were run to ensure that all software settings were correct, all instruments performed properly, and data was saved. Since photomultiplier tubes are highly sensitive photodetectors, experiments of this nature yield the best results in environments with minimized ambient light. Therefore, the overhead lights of the experimentation room were turned off to prevent extraneous light leakage to the PMT. The PMT and LED were turned on and allowed to warm up for 30 minutes to 1 hour prior to collecting data. This increased the output stability of the PMT over the length of the test.[45]

For an experiment conducted at steady-state temperatures, the variable AC power supply was adjusted to the voltage setting that produced the desired temperature. This was done using circuit 6 on the power source. Fig. 3.3.1 displays these voltage settings for the various temperatures taken during a calibration run. Once the temperature had stabilized, a small amount of lead temperature measurements was collected from the RTD input thermometer before the oscilloscope driver program was triggered to begin data acquisition. This ensured that the start time temperature corresponding to the initial phosphor emission was captured. The steady state temperature was monitored during the entire the data collection process. Due to electrical instabilities, minor voltage adjustments were intermittently made.

Table 3.3.1 shows the three different cases of transient experimental runs that were conducted. Just as in the steady state experiments, lead temperature measurements were collected from the RTD before phosphor

emission acquisition commenced for each transient experiment. For the first transient case, once data collection had begun, the heater supply voltage was set to 9.5 VAC. The copper sample was heated from room temperature to about 60°C. Prior to conducting the second transient case, it was necessary to heat the copper sample to 60°C. Once data collection begun, the AC power source was turned off. Heat was no longer being supplied to the copper sample. Due to time constraints when running this particular experiment, data acquisition was stopped before the copper sample had completely reached ambient temperature. Therefore, this temperature range differed from that of the other transient cases by about 7°C. Following the start of data collection for the third transient case, the AC voltage was modulated throughout the experiment to produce a heating and subsequent cooling pattern. The temperature of the copper sample during this case spanned from room temperature to 60°C.

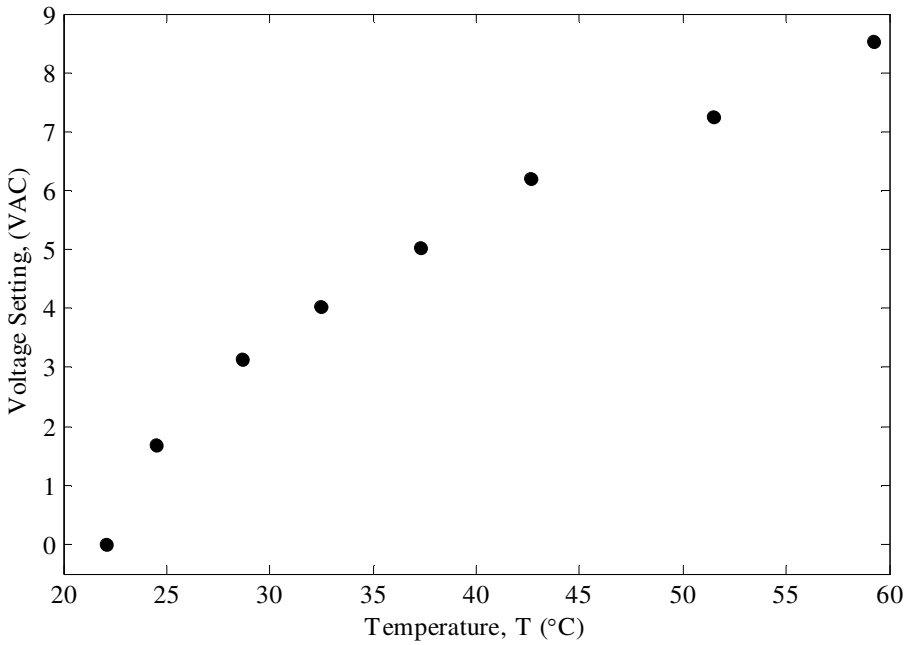

Figure 3.3.1: AC Voltage Setting Against Temperature for Calibration Experiment

Table 3.3.1: Three Cases of Transient Experimental Runs

Case	Experiment Type	Voltage Setting	Temperature Range (°C)
Transient Run 1	Constant Voltage Heating	9.5 VAC	$T \in [RoomTemp,60]$
Transient Run 2	Sample Cool Down	--	$T \in [30,60]$
Transient Run 3	Heating/Cooling Pattern	Variable	$T \in [RoomTemp,60]$

Chapter 4: Experimental Results

The aim of this chapter is to present the experimental results that validate the alternative calibration techniques discussed in Chapter 2.2. The steady-state experiments are used to create a calibration curve that can be applied to the transient tests. The steady-state portion of experimentation represents the calibration study of the TP La_2O_2S:Eu. Multiple experimental measurements were collected under known and repeatable conditions to characterize the physical behavior of this phosphor over the desired temperature range. The calibration data are used to generate a steady-state model (calibration curve) that predicts temperature. The effectiveness of the derived calibration curve as a temperature measurement system is investigated from two different avenues. First, the uncertainty in the collected calibration data is quantified through various statistical parameters. The second area of effectiveness is explored in the transient portion of experimentation. It must be shown that the calibration model can be applied in practical testing scenarios to resolve the temporal temperature history of a test sample.

4.1 Description of Experimental Data

Prior to presenting the results of this work, it is necessary to note certain characteristics and post-processing details common to steady-state and transient experimental data. The measurement window for a given TP emission spans 100 μs. Each signal contains 10 μs of lead data prior to the start of the excitation pulse. After a pulse width of 20 μs, the LED turns off and the excited phosphor then decays back to its ground state. Figure 4.1.1 displays a characteristic phosphor response to the excitation pulse seen on the oscilloscope. Both the emission signal and LED pulse have been averaged over 512 waveforms. As can be observed in Fig. 4.1.1, the LED does not obey a distinct on and off time but instead exhibits a rise and decay portion of data that subsequently manifests in the phosphor emission signal. The effect on the signal is constant across all experimental data collection and therefore does not require special consideration during post-processing. However, it is important to note that the LED decay time does act as the minimum decay time value of the TP emission. Temperature effects are no longer able to be resolved from the decay portion of the signal past this point.

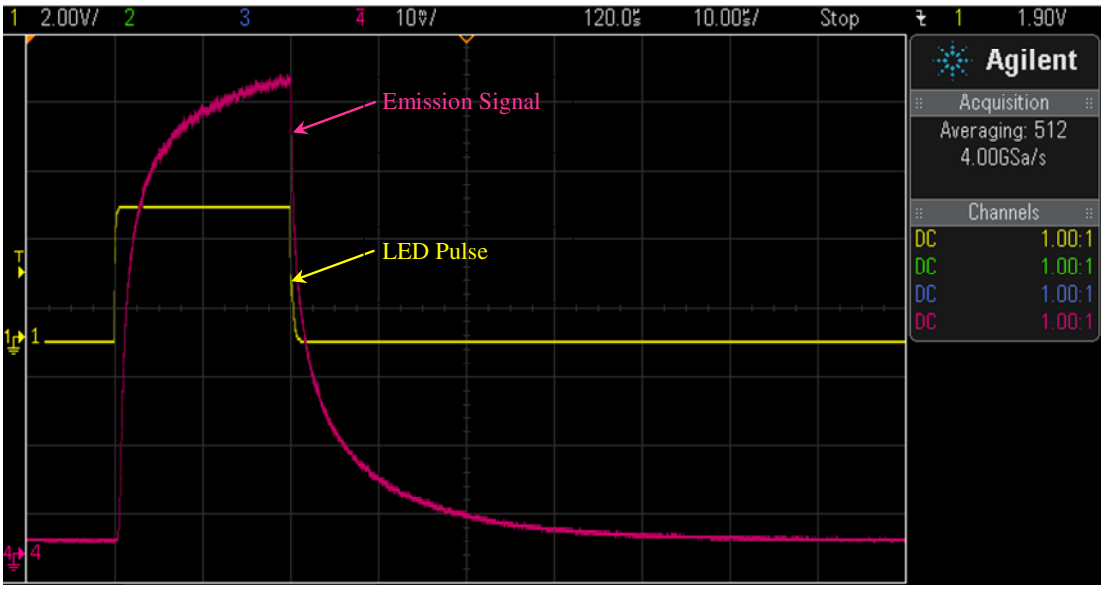

Figure 4.1.1: Oscilloscope Display of Representative Phosphor Emission Signal and LED Pulse

The oscilloscope has a maximum sample rate of 4 GSa/s, which translates to a sample taken every 250 ps. This raw measurement record, as seen on the oscilloscope display window in Fig. 4.1.1, does not comprise the waveform record that is analyzed in post-processing. Once a signal acquisition is complete, the collected data are resampled at certain time buckets and transferred to the PC controller. The extra samples are decimated. The chosen amount of data points represents a compromise between the time resolution needed to pick up the quick changes in TP behavior and the speed of data transfer. In these experiments, the final waveform is resampled at $\Delta t = 50ns$ so that the waveform record saved to the PC contains 2000 time-voltage pairs and requires approximately 2-3 s of transit time. Every saved signal contains a characteristic baseline voltage shift that results from current leakage in the PMT and also the ambient light environment of the experimentation room. This offset in emission intensity is corrected for all signals in both steady-state and transient experiments during post-processing. The portion of lead data spanning the first 8.7 μs of data collection is averaged together to obtain a single mean value. The mean value is subtracted from the entire phosphor signal as seen in Fig. 4.1.2.

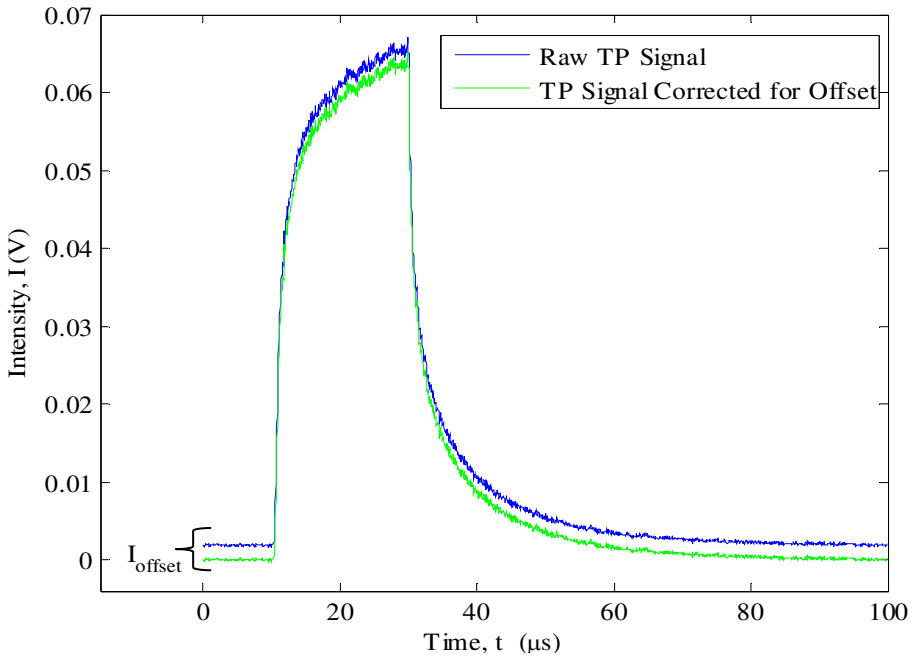

Figure 4.1.2: Phosphor Emission Intensity over Time Corrected for Light Leakage

4.2 Steady-State Results

It has already been demonstrated in Chapter 2.2 that portions of the integrated phosphor response exhibit temperature dependence. These regions include the linear portion of the integrated intensity curve, which can be characterized by its slope, η, and the total integral value of the signal, Ψ_T. Figures 2.2.6 and 2.2.7 displayed a curve relating each respective calibration parameter to temperature for a single set of fluorescence emissions. These curves were shown solely for demonstration purposes and are not an adequate representation of TP behavior as a function of temperature. A true calibration procedure involves extracting the desired measured output from numerous collected phosphor emissions taken at distinctive temperature steps. The number of captured signals represents the data sample size, W.

For the purposes of this thesis, calibration of the TP La_2O_2S:Eu over the temperature range $T \in [Room\,Temp, 60°C]$ was done using the experimental scheme detailed in Chapter 3. A total of $W = 230$ experimental runs were conducted at eight temperature steps in order to develop an accurate representation of TP behavior across the desired range. For each experimental run, the captured phosphor response was shot-averaged over $N = 512$ waveforms. Figure 4.2.1 displays all 230 phosphor signals present at each desired temperature step that were used in calibration. Each emission was then integrated according to a simple rectangular rule given as

$$\int_{t=0}^{t_{tot}} I(t)dt \approx \Psi(t) = \Delta t \sum_{i=1}^{m'} I(t_i), i = 1,2,...,m', \tag{4.2.1}$$

where Δt represents the phosphor emission time increment of 50 ns and m' is the total number of data points in each sample run. All integrated intensity trajectories in time for each temperature can be seen in Fig. 4.2.2.

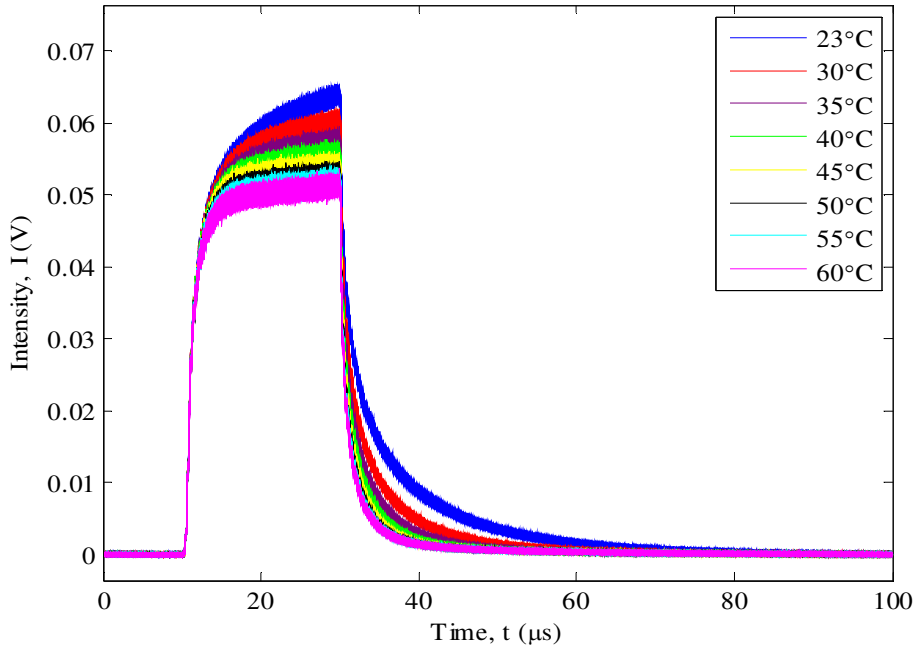

Figure 4.2.1: All Phosphor Emissions Used in Calibration Study (W=230)

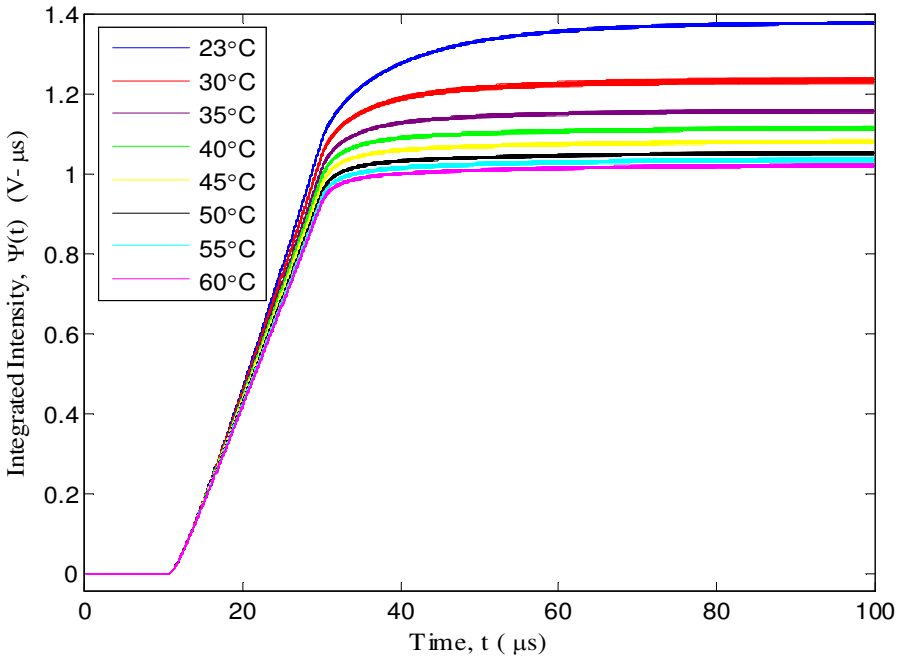

Figure 4.2.2: Integrated Intensity Curves Used in Calibration Study (W=230)

Both the slope, η, and the total integral, Ψ_T, were extracted from each integrated intensity curve using the methods detailed in Chapter 2.2. Also, a RTD temperature measurement was taken to correspond to each captured curve. Therefore, there are eight data sets with $W = 230$ measurements for both calibration parameters and the calibration standard. The best estimate for the calibration value used in the steady-state model was taken to be the mean of the data set. The temperature standard average at each temperature step becomes

$$T_{standard} = \overline{T}_{RTD} = \frac{1}{W}\sum_{i=1}^{W} T_i, \quad i = 1,2,\ldots,W. \tag{4.2.2}$$

In this fashion, at each $T_{standard}$, the slope calibration value becomes

$$\eta_{best} = \overline{\eta} = \frac{1}{W}\sum_{i=1}^{W} \eta_i, \quad i = 1,2,\ldots,W, \tag{4.2.3}$$

where η_{best} is the best representation of any given data set of η. The total integral calibration value becomes

$$\Psi_{T,best} = \overline{\Psi}_T = \frac{1}{W}\sum_{i=1}^{W}\Psi_{T,i}, \quad i = 1,2,\ldots,W. \tag{4.2.4}$$

where $\Psi_{T,best}$ is the best representation of any given data set of Ψ_T.

In order to quantify the validity of the calibration data and also justify the use of the mean as the best characterization of a data set, the statistical parameters of standard deviation, variance, and precision interval must be presented alongside the collected data.[46] In the following discussion of these values, the set of the temperature standard calibration measurements, $\{T_i\}_{i=1}^{W}$, as well as the sets of the both calibration parameters, $\{\eta_i\}_{i=1}^{W}$ (slope) and $\{\Psi_{T,i}\}_{i=1}^{W}$ (total integrated intensity), are collectively denoted as a general calibration set $\{c_i\}_{i=1}^{W}$ that can be characterized by mean $\overline{c}$. The unbiased standard deviation, σ, represents the width of the data distribution about the mean value and is defined by

$$\sigma = \sqrt{\frac{1}{W-1}\sum_{i=1}^{W}(c_i - \overline{c})^2}, \quad i = 1,2,\cdots,W. \tag{4.2.5}$$

The sample variance, σ^2, which represents the precision of the measured calibration measurements, is defined as

$$\sigma^2 = \frac{1}{W-1}\sum_{i=1}^{W}(c_i - \overline{c})^2, \quad i = 1,2,\cdots,W. \tag{4.2.6}$$

Finally, the uncertainty of using the mean value $\overline{c}$ as the calibration parameter is established using an uncertainty interval. Assuming a normal distribution of errors, this parameter indicates the interval that will contain the next calibration measurement c_i given a certain probability level, P. For $P = 95\%$, that interval for c_i becomes

$$c_i = \overline{c} \pm 2\sigma. \tag{4.2.7}$$

The final product of the calibration study is a calibration curve that develops a functional relationship in the form of

$$T = f(\eta), \quad T \in [RoomTemp, 60°C], \tag{4.2.8}$$

for the slope calibration technique, and

$$T = f(\Psi_T), \quad T \in [RoomTemp, 60°C], \tag{4.2.9}$$

for the total integral calibration technique. The process of curve fitting involves finding the set of coefficients $\{p_i\}$, for a prescribed model structure that minimize uncertainty between the actual data, T_i, and the function fit, $T_M(c_i)$. The accuracy of different functional models is compared based on important metrics that indicate the "goodness" of a fit to the calibration data. The sum of squares of the deviation, D_M, of the fitted model from the actual calibration measurements for all values of T_i, $i = 1,2,\cdots,m,$ is

$$D_M = \sum_{i=1}^{m} [T_i - T_M(c_i)]^2. \tag{4.2.10}$$

A value of D_M closer to 0 indicates that the model has a smaller random error component. Another measure for the goodness of fit is the correlation coefficient, R_M^2, which is expressed as

$$R_M^2 = \frac{\sum_{i=1}^{m} (T_M(c_i) - \hat{T})^2}{\sum_{i=1}^{m} (T_i - \hat{T})^2}, \tag{4.2.11}$$

where $\hat{T}$ is the arithmetic mean of the samples and is given as

$$\hat{T} = \frac{1}{m} \sum_{i=1}^{m} T_i. \tag{4.2.12}$$

This statistic measures how successful the fit is in explaining the variation of the data. A value closer to 1 indicates that a greater proportion is accounted for by the model. However, the R_M^2 value can be misleading because increasing the equation order, M, of the fit can increase this parameter without effectively improving the fit. This deficiency is rectified by using the value of $R_{adj,M}^2$, which account for the degrees of freedom, v, of the particular model. The $R_{adj,M}^2$ statistic is given as

$$R^2_{adj,M} = 1 - \frac{\sum_{i=1}^{m}(T_i - T_M(c_i))^2}{\sum_{i=1}^{m}(T_i - \hat{T})^2}\frac{(m-1)}{v}, \tag{4.2.13}$$

where v is the residual degrees of freedom and can be defined as

$$v = m - d_M, \tag{4.2.14}$$

where m denotes the number of calibration data points d_M denotes the number of fitted coefficients for the given regression model. A goodness-of-fit metric is root-mean-square error, denoted by rms_M, and is given by

$$rms_M = \sqrt{\frac{\sum_{i=1}^{m}[(T_i - T_M(c_i)]^2}{v}}. \tag{4.2.15}$$

This parameter is an estimate of the standard deviation of the random component in the data. As with the statistical parameter, D_M, a value closer to 0 indicates a better fit. A final useful parameter in evaluating the best curve is to analyze the numerical results of the fitted model. The 95% confidence bounds, CB, for a certain fitted coefficient, p_i in the set $i = M_{\min},\ldots,M$ ($M_{\min} = 0,1$) is given as

$$CB = p_i \pm t_{v,95}S_{p_i}, \tag{4.2.16}$$

where t is taken from the *Student-T distribution* and S_{p_i} is the standard error of fitted coefficient p_i. Equation (4.2.16) indicates the uncertainty in each model coefficient. The choice of a "good fit" model would be one in which the model coefficients can be estimated with little uncertainty.

As detailed above, the level of accuracy for a developed calibration curve depends on the uncertainty in the temperature standard (Eqs. 4.2.2,5-7), the uncertainty in the selected calibration parameter (Eqs. 4.2.3-7), and the uncertainty in the data reduction method used to fit the calibration data to a function relationship (Eqs. 4.2.8-16). The previously described statistical metrics are used to quantify these uncertainties and judge their effect on the quality of the calibration method used to predict the temperature response. The latter two error sources vary depending on the given calibration technique and must be presented in its given section. However, the uncertainty in the RTD temperature standard is unchanging. An a priori investigation may be done.

RTD temperature measurements are taken at the start of each phosphor emission collection to provide a known standard to be calibrated against. The temperature was assumed to remain constant through the total time given as $N(t_{tot}) = 51.2\,ms$ needed to acquire each of the final averaged fluorescent signals. It was desired that a temperature measurement be taken approximately every 5 degrees to provide an adequate estimation of TP behavior across the entire temperature range, $T \in [Room\,Temp, 60°C]$. The RTD temperature measurements corresponding to each captured phosphor waveform, W, of all temperature steps across the full calibration region can be seen in Fig. 4.2.3. Small variations do exist around the mean RTD temperature line caused by electrical instabilities in the heater power source. This introduces uncertainty into the steady-state model. The set of standard temperatures values used for both calibration techniques are taken from the mean RTD measurements, $\overline{T}_{RTD}$. These results are detailed in Table 4.2.1. In general, there is a slight increase in the values of σ and σ^2 at higher temperature levels, which indicates a small increase in both the precision error and in the width of the data distribution about the mean. However, this increase still only translates to a maximum 2σ probability interval of $\pm 0.2°C$ which corresponds to $\overline{T}_{RTD} = 59.9°C$. Since this uncertainty level is on the same order as the RTD thermometer resolution of $0.1°C$, it can be assumed that the variation of temperature at each step has a small effect on the overall accuracy of the temperature standard. Thus, from this point on, all values given by $\left\{\overline{T}_{RTD}\right\}$ are assumed to represent the steady state temperatures used in calibration.

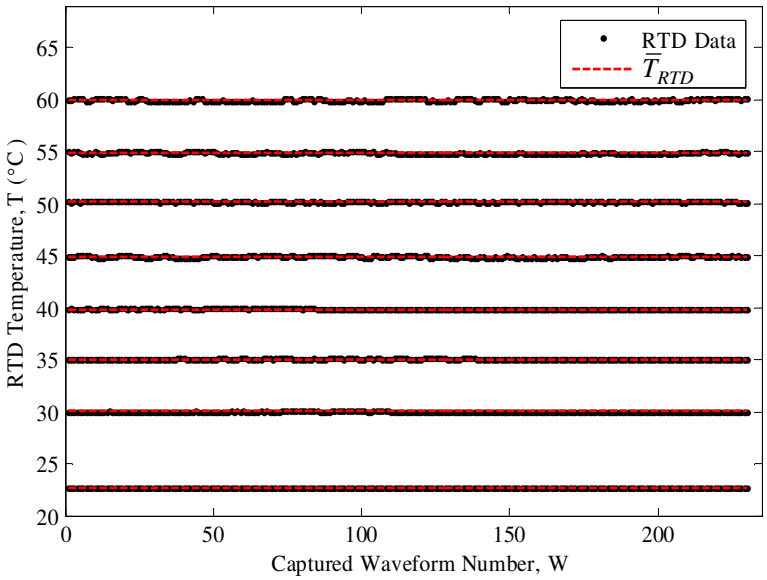

Figure 4.2.3: RTD Data Distribution (W=230) About the Mean Temperature

Table 4.2.1: RTD Temperature Results

Desired Temperature	$\overline{T}_{RTD}$	σ (°C)	σ^2 (°C)^2	±2σ
Room Temperature	22.6 °C	0.050	0.003	±0.1 °C
30 °C	30.0 °C	0.037	0.001	±0.1 °C
35 °C	35.0 °C	0.041	0.002	±0.1 °C
40 °C	39.8 °C	0.044	0.002	±0.1 °C
45 °C	44.9 °C	0.071	0.005	±0.1 °C
50 °C	50.1 °C	0.045	0.002	±0.1 °C
55 °C	54.9 °C	0.077	0.006	±0.2 °C
60 °C	59.9 °C	0.088	0.008	±0.2 °C

A. Calibration Based on Slope of Linear Portion of Integral Trajectory

The linear portion of all integrated intensity trajectories seen in Fig. 4.2.2 has been analyzed according to the process previously detailed in Chapter 2.2B. The calibration value η is resolved for each captured waveform by performing a linear least squares regression on the integrated intensity data in the fixed window of $t \in [18\mu s, 30\mu s]$. Figure 4.2.4 presents the distribution of this value across the mean line for each temperature time step. The mean of the slope, $\overline{\eta}$, is reported as the calibration value. Table 4.2.2 displays these results. It can be seen that the data values are scattered evenly across the mean with small precision errors in each distribution. The 2σ values presented in table can also be seen graphically in Fig. 4.2.5. The calibration slope $\pm 2\sigma$ error bars for are overlaid on the individual slope-temperature data values. The temperature error bars calculated in Table 4.2.1 were not able to be perceived on the temperature axis scale of Fig. 4.2.5 and are not displayed. These results show that the slope calibration parameter is indeed a repeatable measurement that possess sensitivity across $T \in [Room\,Temp, 60°C]$. Each evaluated temperature-slope calibration pair found in $\{\overline{T}_{RTD,i}, \overline{\eta}_i\}_{i=1}^{m}$ can now be used to generate a calibration curve.

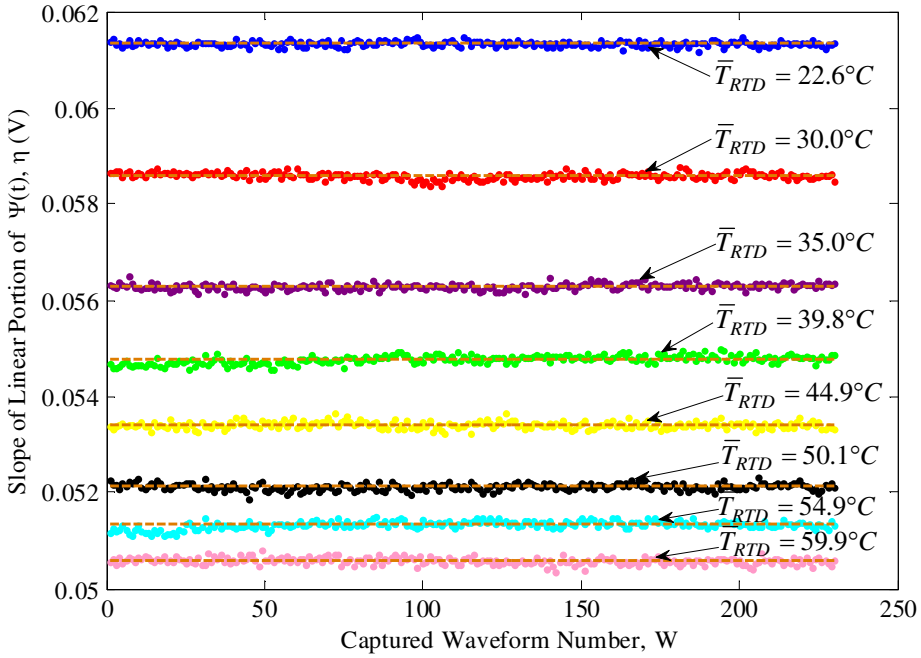

Figure 4.2.4: Slope Data Distribution (W=230) About the Mean Calibration Value

Table 4.2.2: Slope Calibration Parameter Results

$\overline{T}_{RTD}$	$\overline{\eta}$	σ (V)	σ^2 (V^2)	±2σ
22.6 °C	0.0613 V	$0.5(10^{-4})$	$0.3(10^{-8})$	±0.0001 V
30.0 °C	0.0586 V	$0.7(10^{-4})$	$0.5(10^{-8})$	±0.0001 V
35.0 °C	0.0563 V	$0.6(10^{-4})$	$0.4(10^{-8})$	±0.0001 V
39.8 °C	0.0548 V	$0.9(10^{-4})$	$0.7(10^{-8})$	±0.0002 V
44.9 °C	0.0534 V	$0.7(10^{-4})$	$0.5(10^{-8})$	±0.0001 V
50.1 °C	0.0521 V	$0.7(10^{-4})$	$0.5(10^{-8})$	±0.0001 V
54.9 °C	0.0513 V	$0.8(10^{-4})$	$0.6(10^{-8})$	±0.0002 V
59.9 °C	0.0506 V	$0.7(10^{-4})$	$0.5(10^{-8})$	±0.0001 V

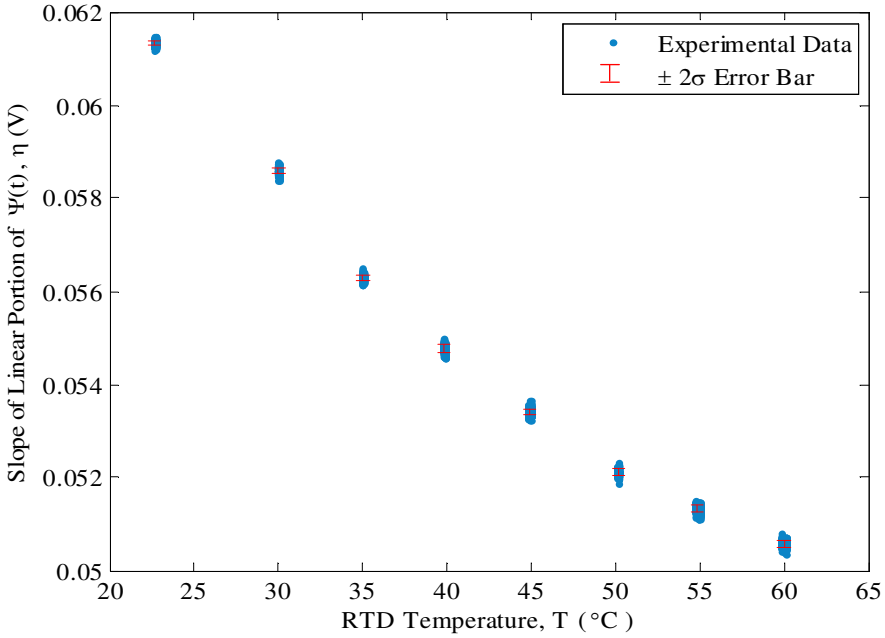

Figure 4.2.5: Slope Calibration Error Bars Overlaid on All Slope-Temperature Values

Figure 4.2.5 presents slope values as a function of steady-state temperature in order to more easily display the data distribution of η for each temperature step. In a true calibration curve, however, the relationship must be presented such that the input value of the temperature standard is the controlled independent variable, while the measured output value becomes the dependent variable of the calibration as seen in Eq. (4.2.8). An investigation into various functional models must now be conducted in order to find the model that best characterizes the calibration data, $\{\eta_i, T_i\}_{i=1}^{m}$ in the operating range. Various forms of the three different regression models (polynomial, rational, and exponential) are used to approximate the representative curve of this slope calibration technique. The curve-fitting statistics defined in Eqs. (4.2.10-4.2.16) are included with each fit. In total, the description and results of six different fits will be presented for this technique. A comparison of these fits will conclude the section.

The first fit assumes that the real-valued functional relationship $T = f(\eta)$ can be expanded as

$$T(\eta) = \sum_{j=0}^{\infty} p_j B_j(\eta), \quad T \in [RoomTemp, 60°C], \tag{4.2.17}$$

where $B_j(\eta)$ are the monomial basis functions and p_j are the unknown coefficients. Let $T_M(\eta)$ denote the M-degree polynomial approximate solution to $T(\eta)$ for the m discrete calibration values in $\{\eta_i, T_i\}_{i=1}^{m}$, i.e.,

$$T(\eta) \approx T_M(\eta) = \sum_{j=0}^{M} p_j \eta^j, \quad T \in [RoomTemp, 60°C]. \tag{4.2.18}$$

To obtain the unknown expansion coefficients $\{p_j\}_{j=0}^{M}$, the linear least-squares method minimizes the sum squares of the deviation, D_M, given in Eq. (4.2.10). For the polynomial fit, Eq. (4.2.10) becomes

$$D_M = \sum_{i=1}^{m} \left[T_i - p_0 - p_1\eta_i - p_2\eta_i^2 - \cdots - p_M \eta_i^M\right]^2, \quad T \in [RoomTemp, 60°C], \tag{4.2.19}$$

for a polynomial of degree M with m discrete calibration values.

For this analysis, both the second-degree polynomial, $M = 2,$ and the third-degree polynomial, $M = 3,$ are used to model the raw calibration data. Figure 4.2.6 and Table 4.2.3 display the results of the polynomial using the raw slope calibration data. From observing these outputs, it can be seen that the third-degree polynomial, denoted "Fit 2" in the figure and table, provides a better fit to the calibration points than the second-degree polynomial on all statistical counts.

The second curve fit assumes that the calibration data may be approximated by a rational function model. Rational models are defined as ratios of polynomials[47] and are given as

$$T_{M,L}(\eta) = \frac{P_M(\eta)}{Q_L(\eta)}, \quad T \in [RoomTemp, 60°C], \tag{4.2.20}$$

where $P_M(\eta)$ and $Q_L(\eta)$ are polynomials of degree M and $L,$ respectively. By expanding the polynomials, Eq. (4.2.20) becomes

$$T_{M,L}(\eta) = \frac{\sum_{j=0}^{M} p_j \, \eta^j}{\eta^L + \sum_{k=0}^{L-1} q_k \, \eta^k}, \quad T \in [RoomTemp, 60°C]. \tag{4.2.21}$$

It is important to note that the coefficient associated with η^L is assumed to be 1 in order to ensure that the numerator and denominator are unique when the polynomial degrees are the same. The $M + L + 1$ unknown expansion coefficients of $[p_0, p_1, \ldots, p_M, q_0, q_1, \ldots, q_{L-1}]$ are resolved using nonlinear least-squares. Two different calibration curves are generated from using Eq. (4.2.21) to model the raw calibration data $\{\eta_i, T_i\}_{i=1}^{m}$. The first curve employs a second-degree $(M = 2)$ numerator polynomial, while the other uses a first-degree $(M = 1)$ polynomial. Both have a first-degree $(L = 1)$ polynomial in the denominator. Figure 4.2.7 displays the two curves, and the tabulated results can be found in Table 4.2.4. From observing these outputs, it can be seen that the function with the second-degree numerator polynomial, denoted "Fit 1" in the figure and table, provides a better fit to the calibration points than the function using a first-degree polynomial numerator for all statistical counts.

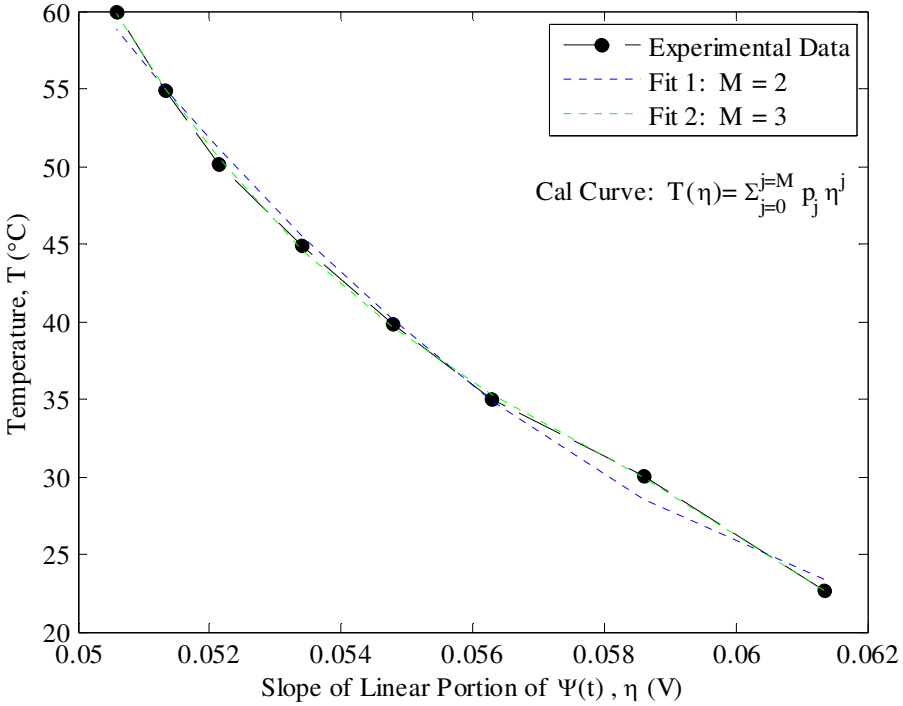

Figure 4.2.6: Polynomial Calibration Curves Using Slope Calibration Data

Table 4.2.3: Tabulated Results from Polynomial Curve Fit Using Slope Calibration Data

	Fit 1	Fit 2	Units
p_0 (95% CB)	779.4 (501.4, 1058)	5592 (3726,7458)	°C
p_1 (95% CB)	$-2.328(10^4)$ $(-3.328(10^4),-1.328(10^4))$	$-2.828(10^5)$ $(-3.833(10^5),-1.822(10^5))$	°C/V
p_2 (95% CB)	$1.786(10^5)$ $(8.904(10^4), 2.681(10^5))$	$4.831(10^6)$ $(3.029(10^6),6.633(10^6))$	°C/V^2
p_3 (95% CB)	--	$-2.774(10^7)$ $(-3.848(10^7),-1.7(10^7))$	°C/V^3
D_M	5.744	0.4147	(°C)^2
R_M^2	0.9949	0.9996	--
$R_{adj,M}^2$	0.9929	0.9994	--
rms_M	1.072	0.322	°C

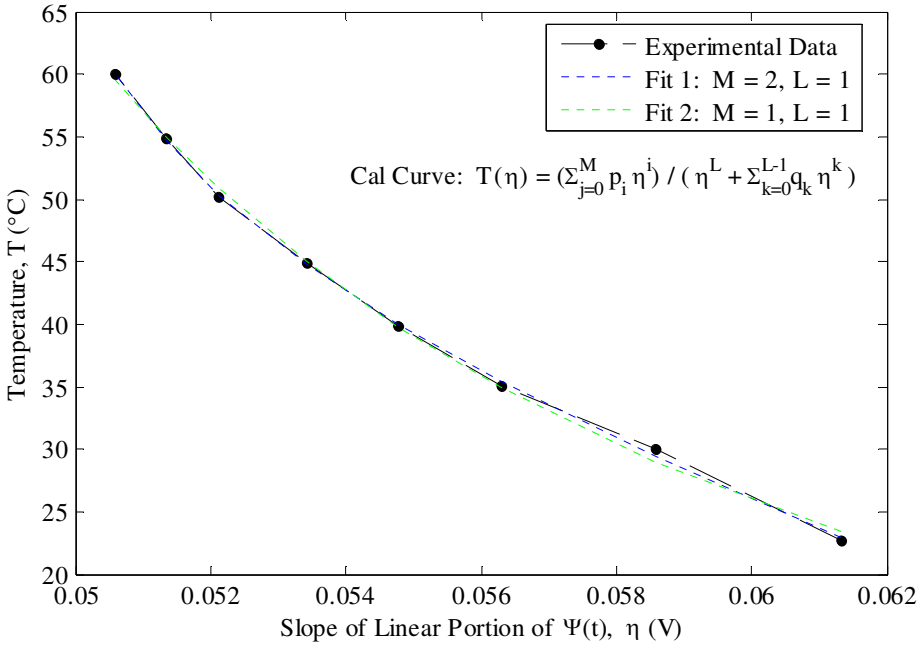

Figure 4.2.7: Rational Function Calibration Curves Using Slope Calibration Data

Table 4.2.4: Tabulated Results from Rational Function Curve Fit Using slope Calibration Data

	Fit 1	Fit 2	Units
p_0 (95% CB)	-6.212 (-9.59,-2.835)	1.62 (0.4392, 2.802)	°C
p_1 (95% CB)	222.7 (116.3,329.1)	-17.66 (-35.5,0.1838)	°C/V
p_2 (95% CB)	-1893 (-2574,-1031)	--	°C/V^2
q_0 (95% CB)	-0.0471 (-0.05049,-0.04371)	-0.03836 (-0.04327,-0.0334)	°C
D_M	0.7322	2.432	(°C)^2
R_M^2	0.9994	0.9979	--
$R_{adj,M}^2$	0.9989	0.997	--
rms_M	0.4278	0.6975	°C

The final investigation involves fitting the calibration data points $\{\eta_i, T_i\}_{i=1}^{m}$ to an exponential model as given by

$$T_M(\eta) = \sum_{j=1}^{M} a_j e^{b_j \eta}, \quad T \in [RoomTemp, 60°C]. \tag{4.2.22}$$

Specifically for this analysis, the one-term $(M = 1)$ and two-term $(M = 2)$ exponentials are used. Following the previous example, the unknown coefficients $\{a_j\}_{j=1}^{M}$ and $\{b_j\}_{j=1}^{M}$ are resolved using nonlinear least-squares. The solutions of these two models are the calibration curves graphically displayed in Fig. 4.2.8. Also, the tabulated results associated with the curve fitting routine can be seen in Table 4.2.5. From observing these outputs, it can be seen that the bi-exponential model, denoted "Fit 2" in the figure and table, provides a better fit to the calibration points than the mono-exponential for all statistical counts.

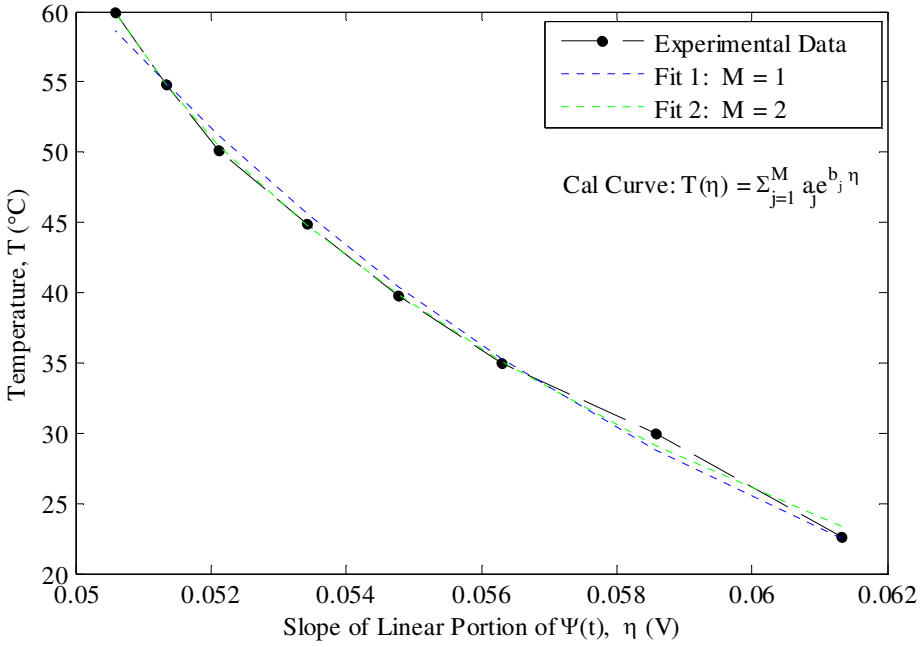

Figure 4.2.8: Exponential Function Calibration Curves Using Slope Calibration Data

Table 4.2.5: Tabulated Results from Exponential Function Curve Fit Using Slope Calibration Data

	Fit 1	Fit 2	Units
a_1 (95% CB)	5318 (3381, 7255)	3344 (491.3,6197)	°C
a_2 (95% CB)	--	$1.487(10^{17})$ ($-1.114(10^{19})$,$1.143(10^{19})$)	°C
b_1 (95% CB)	-89.09 (-95.95,-82.24)	-80.96 (-95.67,-66.25)	V^{-1}
b_2 (95% CB)	--	-753.1 (-2277,770.7)	V^{-1}
D_M	5.201	1.37	$(°C)^2$
R_M^2	0.9954	0.9988	--
$R_{adj,M}^2$	0.9947	0.9979	--
rms_M	0.931	0.5852	°C

The best fit for each regression function model were chosen from comparison of the goodness-of-fit statistics pertaining to that model type only. The stark difference in the statistical parameters between the two related fits can be easily perceived and thus a more thorough investigation is not warranted. This is not the case, however, when comparing all regression fit models. Upon first examination, it can be seen that the third-degree polynomial function model possess the best measure for the sum of squares of deviation and root mean square error since $D_M = 0.4147(°C)^2$ and $rms_M = 0.322\ (°C)$ are the closest values to zero across the fits. Together these statistical parameters represent the error of the fitting algorithm and thus can be influenced by the nature of the approximation process. Generally, nonlinear models are more difficult to fit than the linear regression method employed for the polynomial fit. In nonlinear least squares the unknown coefficients cannot be directly estimated and instead rely on an iterative process based on reasonable starting values to direct the fit approximation in the desired direction. Therefore, direct comparison of D_M and rms_M does not necessarily indicate the candidate for best fit. It is generally deduced that the fit error associated with each regression model is sufficiently small. Next, it is informative to examine how the fit predicts the behavior of the actual response value. The best R_M^2 value is associated with the polynomial model. As previously mentioned, however, this parameter can be misleading for models with added coefficients. Thus, the $R_{adj,M}^2$ is a better indicator of fit quality for this case. It can be can be observed that the value of this parameter is on the order of $R_{adj,M}^2 = 0.99$. No functional models are yet rejected.

The next step in this analysis is to examine the confidence bounds of the fit coefficients. The 95% confidence bounds listed in the tabulated results of each fit are used to generate the upper and lower prediction so that the accuracy of this numerical measure may be observed graphically. Figures 4.2.9-4.2.11 present the 95% prediction bounds on the third-degree polynomial curve fit, rational function curve fit, and the bi-exponential curve fit, respectively. As can be seen the polynomial model follows the variation in the calibration data best compared to the other models. The prediction bounds seen in Fig. 4.2.9 also show that this fit possess the smallest amount of uncertainty in the resolved coefficients. This suggests that the polynomial model presents the best choice fit choice. However, it is important to note that all these functional relationships are generated based on the assumption that the calibration data represents the exact behavior of the phosphor response at each steady-state temperature in the given range. On the other hand, a true calibration curve must reflect the physics of the measured data and not just be an arbitrary fit to various data pairs. Using this logic, the curves presented in Fig. 4.2.10 and Fig. 4.2.11 might be a better representation of the trend of the phosphor response despite a larger uncertainty in the resolved model. Special consideration should especially be given to the bi-exponential model since the behavior in the rise portion of the data, which comprises the calibration region of an individual phosphor emission in this slope calibration technique, is generally known to be exponential in nature. Thus, the final decision of the functional model that best represents the calibration curve characteristic for this slope calibration method must be based on its ability to resolve temperatures in a transient test. This avenue of fit effectiveness will be investigated in Section 4.3.

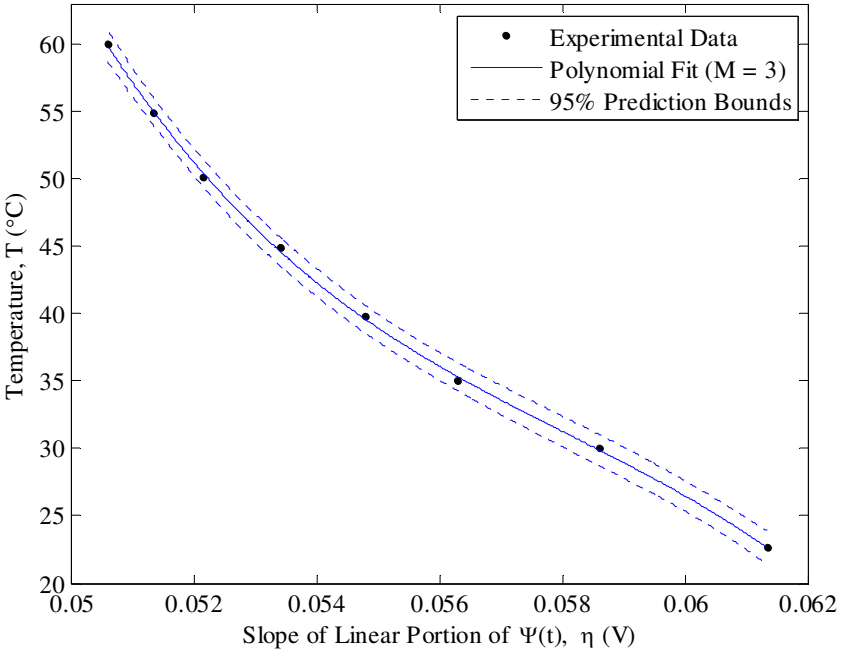

Figure 4.2.9: Prediction Bounds on Polynomial Fit to Observed Slope Calibration Data (Table 4.2.3, Fit 2)

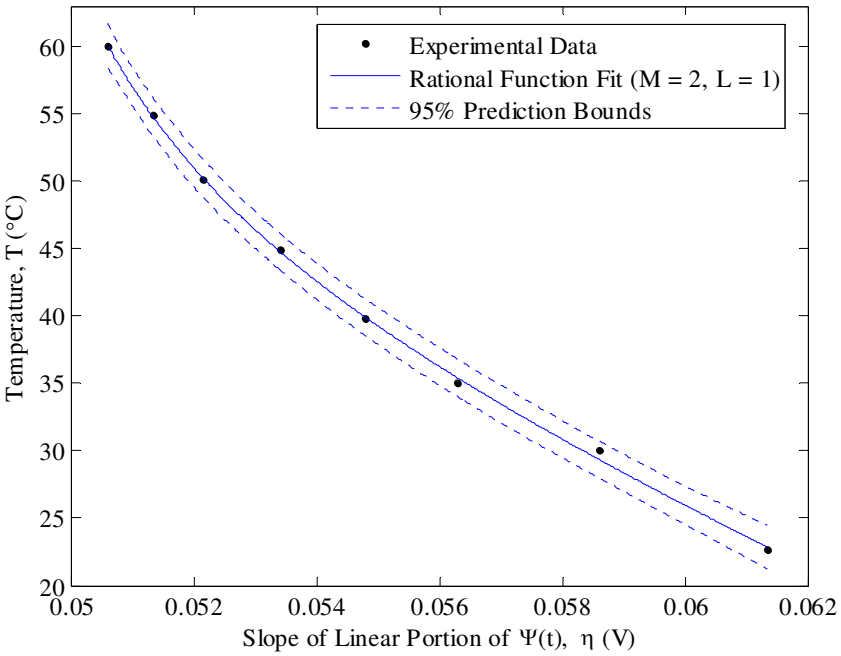

Figure 4.2.10: Prediction Bounds on Rational Function Fit to Observed Slope Calibration Data (Table 4.2.4, Fit 1)

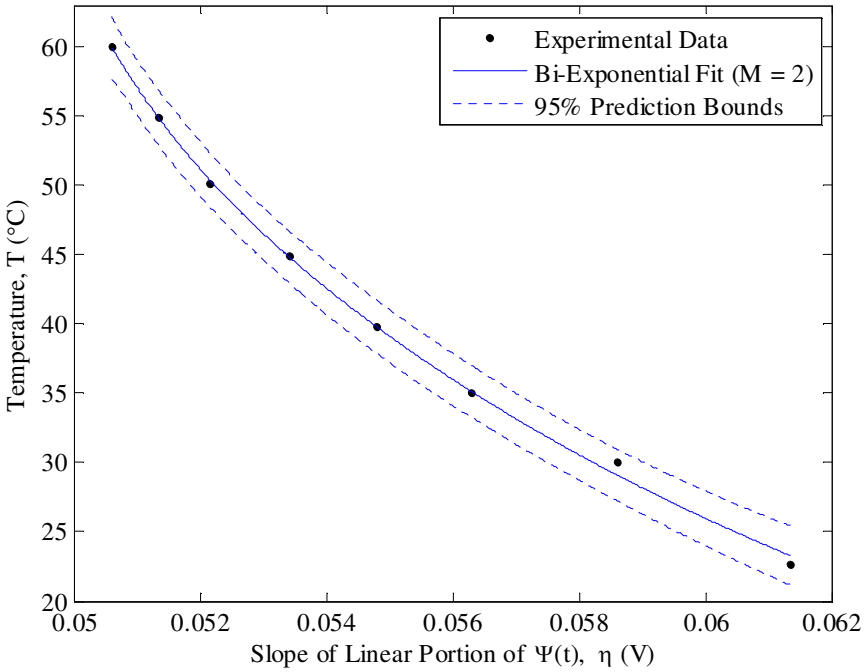

Figure 4.2.11: Prediction Bounds on Bi-Exponential Function Fit to Observed Slope Calibration Data (Table 4.2.5, Fit 2)

B. Calibration Based on Total Integral

This calibration technique involves taking the final value of each $\Psi(t)$ curve seen in Fig. 4.2.2 as the calibration parameter. As previously stated in Chapter 2.2C, this total integrated intensity value, Ψ_T, encompasses the change in the shape of an entire phosphor emission with temperature. Following the investigative procedure into of the previous calibration method, the distribution of all values of Ψ_T resolved from a $W = 230$ sample size of phosphor emission curves must be presented to show that the parameter of interest is a repeatable measurement at a given temperature level. The variation of this distribution across the mean line at each steady-state temperature level can be seen in Fig. 4.2.12. The mean of the total integral, $\overline{\Psi}_T$, is reported as the calibration value. Table 4.2.6 displays these results. It can be seen that the data values are scattered evenly across the mean with small precision errors in each distribution. The 2σ values presented in table can also be seen graphically in Fig. 4.2.13. The calibration integral $\pm 2\sigma$ error bars are overlaid on the individual total integral-temperature data values. The

temperature error bars calculated in Table 4.2.1 were not able to be perceived on the temperature axis scale of Fig. 4.2.13 and are not displayed. These results show that the slope calibration parameter is indeed a repeatable measurement that possess sensitivity across $T \in [Room\,Temp, 60°C]$. Each evaluated temperature-total integral calibration pair found in $\left\{\overline{T}_{RTD,i}, \overline{\Psi}_{T,i}\right\}_{i=1}^{m}$ can now be used to generate a calibration curve.

Once all the calibration data is found, an investigation into various functional models must be conducted. The same various forms of the three different regression models (polynomial, rational, and exponential) previously presented for the slope calibration method are employed to approximate the representative curve of this total integral calibration technique. In total, six different fits along with the pertinent curve-fitting statistics are presented. A comparison of these fits will conclude the section.

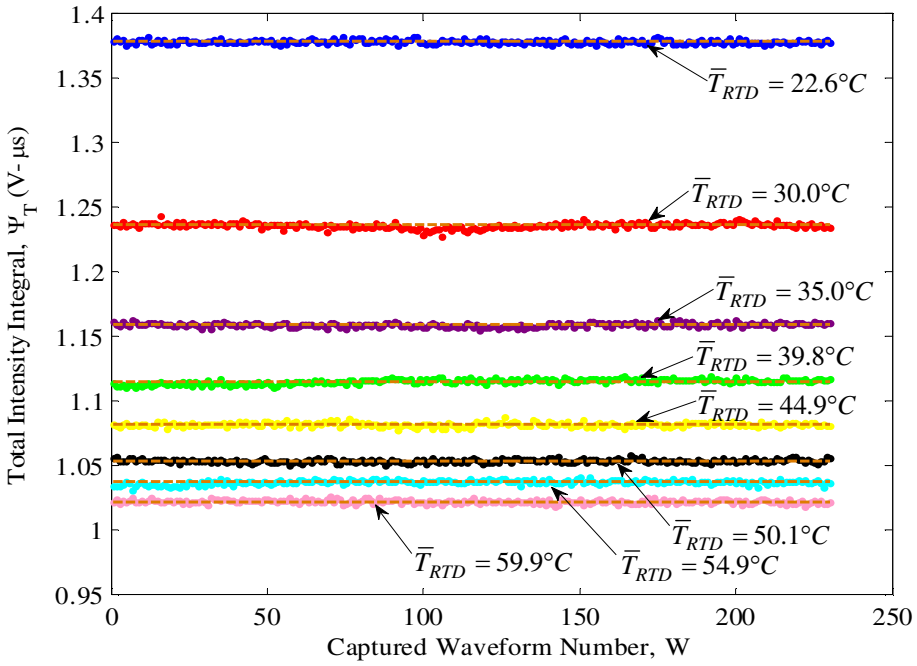

Figure 4.2.12: Total Integral Data Distribution (W=230) About the Mean Calibration Value

Table 4.2.6: Total Integral Calibration Parameter Results

$\overline{T}_{RTD}$	$\overline{\Psi}_T$	σ (V-μs)	σ^2 (V-μs)^2	±2σ
22.6 °C	1.3787 V-μs	1.4(10^{-3})	2.1(10^{-6})	±0.0029 V-μs
30.0 °C	1.2364 V-μs	2.0(10^{-3})	4.2(10^{-6})	±0.0041 V-μs
35.0 °C	1.1594 V-μs	1.5(10^{-3})	2.2(10^{-6})	±0.0029 V-μs
39.8 °C	1.1157 V-μs	1.9(10^{-3})	3.5(10^{-6})	±0.0038 V-μs
44.9 °C	1.0824 V-μs	1.6(10^{-3})	2.4(10^{-6})	±0.0031 V-μs
50.1 °C	1.0543 V-μs	1.3(10^{-3})	1.7(10^{-6})	±0.0026 V-μs
54.9 °C	1.0377 V-μs	1.6(10^{-3})	2.7(10^{-6})	±0.0033 V-μs
59.9 °C	1.0226 V-μs	1.4(10^{-3})	2.0(10^{-6})	±0.0028 V-μs

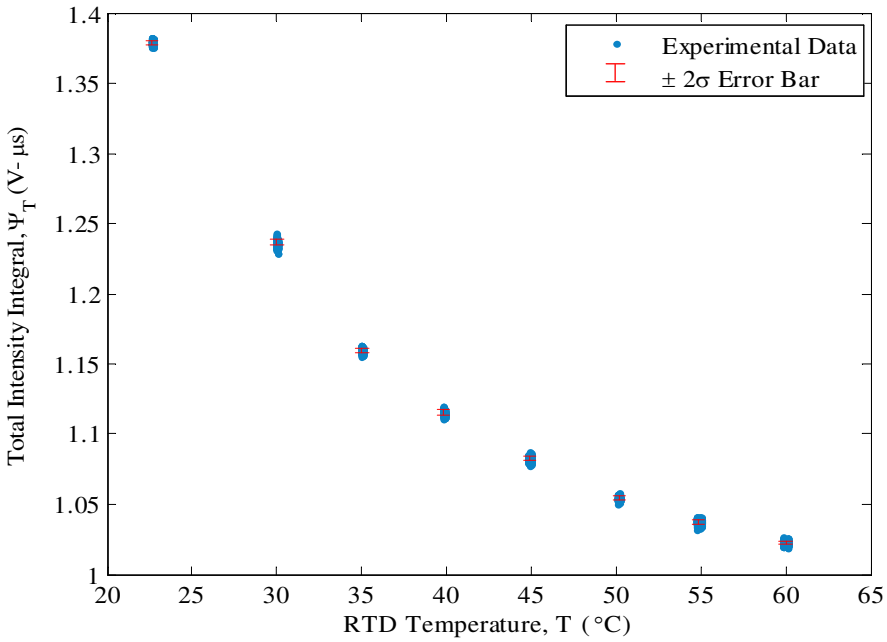

Figure 4.2.13: Total Integral Calibration Error Bars Overlaid on All Integral-Temperature Values

The regressional analysis techniques used for this calibration method are analagous to those used in the previous section. Therefore, the forms of the functional relationship $T = f(\Psi_T)$ used in this investigation will be presented with no background information. The involved fit types used to approximate the m values of the calibration data contained in $\left\{ \Psi_{T,i}, T_i \right\}_{i=1}^{m}$ include the polynomial regression model, as given by

$$T_M(\Psi_T) = \sum_{j=0}^{M} p_j \, \Psi_T^j, \quad T \in [RoomTemp, 60°C], \tag{4.2.23}$$

the rational function regression model, as given by

$$T_{M,L}(\Psi_T) = \frac{\sum_{j=0}^{M} p_j \, \Psi_T^j}{\Psi_T^L + \sum_{k=0}^{L-1} q_k \, \Psi_T^k}, \quad T \in [RoomTemp, 60°C], \tag{4.2.24}$$

and the exponential regression model, as given by

$$T_M(\Psi_T) = \sum_{j=1}^{M} a_j \, e^{b_j \Psi_T}, \quad T \in [RoomTemp, 60°C]. \tag{4.2.25}$$

Figure 4.2.14 and Table 4.2.6 display the results for the second-degree $(M = 2)$ polynomial fit and the third-degree $(M = 3)$ polynomial fit. Comparison of the ouput statistics indicate that "Fit 2" is the better quality polynomial fit. The graphical display and numerical results of the rational function fits can be observed in Fig. 4.2.17 and Table 4.2.7. This first rational function fit is done using a numerator polynomial of degree $M = 2,$ while the second is done using a numerator polynomial of degree $M = 1.$ Both fits have a denominator polynomial of degree $L = 1.$ The first fit, denoted "Fit 1" in this model type, is found to be the better candidate. The final exponential fitting routine is done using a mono-exponential fit $(M = 1)$ and a bi-exponential fit $(M = 2).$ The results of these two fits are summarized in Fig. 4.2.18 and Table 4.2.8. The better approximation of the calibration data in this particular case involves the double exponential summation, which is denoted as "Fit 2" in the output results.

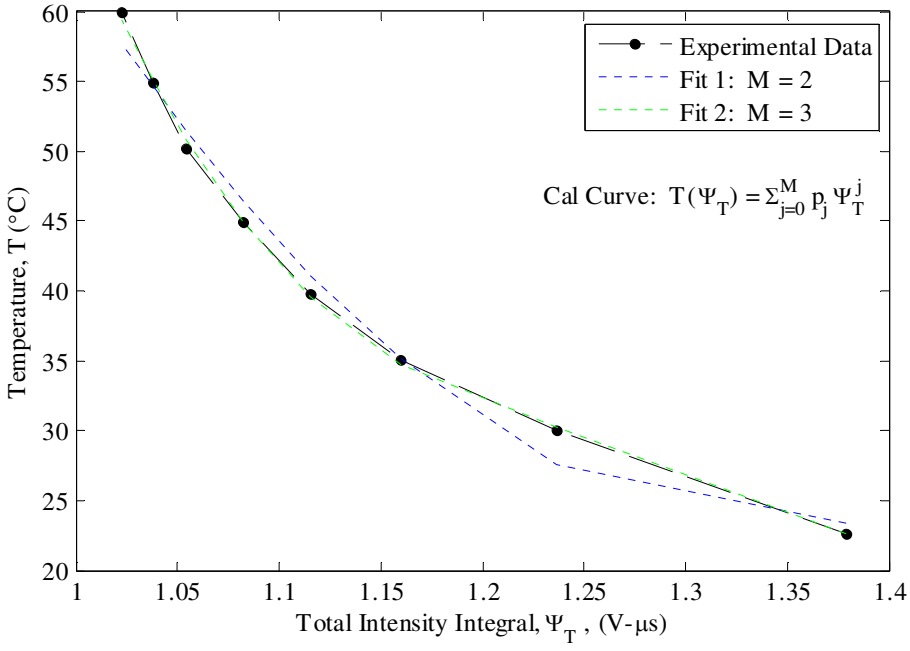

Figure 4.2.14: Polynomial Calibration Curves Using Total Intensity Calibration Data

Table 4.2.7: Tabulated Results from Polynomial Function Curve Fit Using Total Integral Calibration Data

	Fit 1	Fit 2	Units
p_0 (95% CB)	596.8 (394.4,799.3)	3207 (2267,4147)	°C
p_1 (95% CB)	-846.6 (-1188,-505)	-7480 (-9867,-5094)	°C/(V-μs)
p_2 (95% CB)	312.4 (169.7, 455.1)	5897 (3890,7905)	°C/(V-μs)^2
p_3 (95% CB)	--	-1557 (-2117,-997.7)	°C/(V-μs)^3
D_M	17.24	1.082	(°C)^2
R_M^2	0.9848	0.999	--
$R_{adj,M}^2$	0.9788	0.9983	--
rms_M	1.857	0.5202	°C

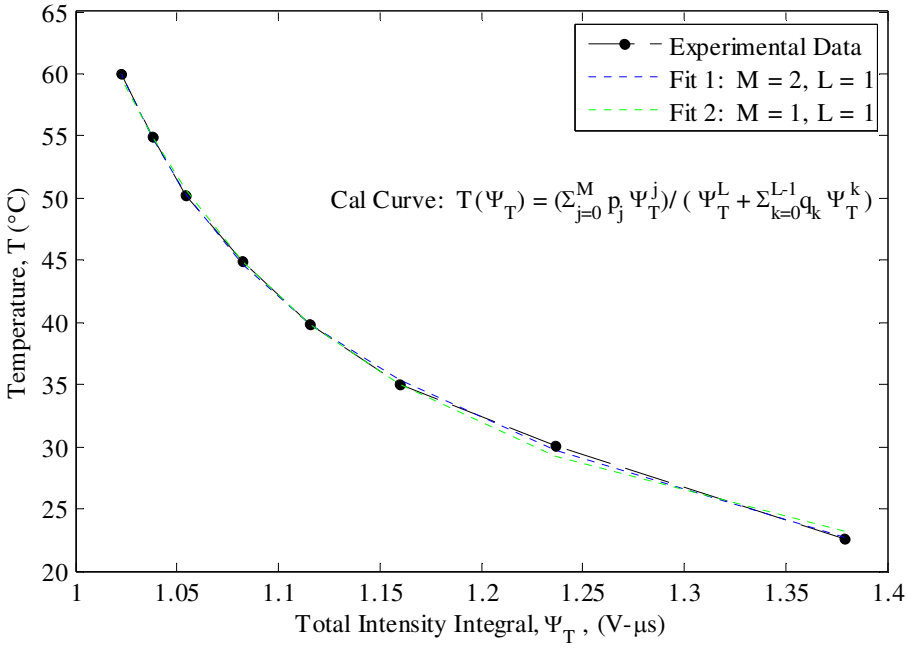

Figure 4.2.15: Rational Function Calibration Curves Using Total Intensity Calibration Data

Table 4.2.8: Tabulated Results from Rational Function Curve Fit Using Total Integral Calibration Data

	Fit 1	Fit 2	Units
p_0 (95% CB)	-40.28 (-64.72,-15.84)	1.209 (-4.474,6.891)	°C
p_1 (95% CB)	69.4 (32.71,106.1)	7.652 (-3.646,11.66)	°C/(V-μs)
p_2 (95% CB)	-23.72 (-37.96,-9.488)	--	°C/(V-μs)^2
q_0 (95% CB)	-0.9246 (-0.9561,-0.8932)	-.8712 (-0.9005,-0.842)	°C
D_M	0.285	1.295	(°C)^2
R_M^2	0.9997	0.9989	--
$R_{adj,M}^2$	0.9996	0.9984	--
rms_M	0.2669	0.509	°C

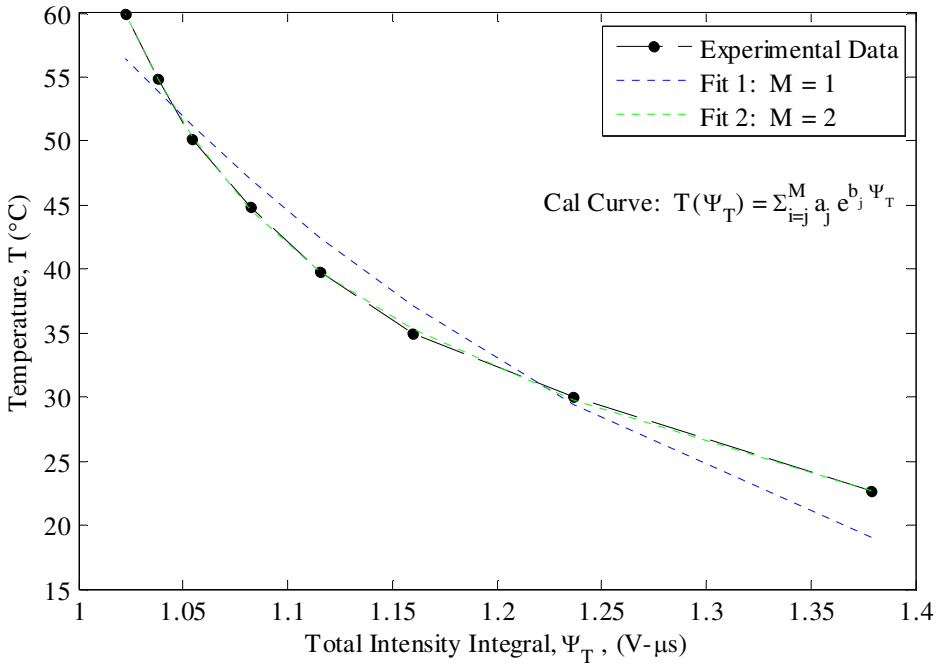

Figure 4.2.16: Exponential Function Calibration Curves Using Total Integral Calibration Data

Table 4.2.9: Tabulated Results from Exponential Function Curve Fit Using Total Integral Calibration Data

	Fit 1	Fit 2	Units
a_1 (95% CB)	1271 (256,2285)	$2.002(10^9)$ ($-7.465(10^9)$,$1.147(10^{10})$)	°C
a_2 (95% CB)	--	288.3 (185.6,391)	°C
b_1 (95% CB)	-3.046 (-3.781,-2.311)	-18.22 (-23.02,-13.42)	$(V\text{-}\mu s)^{-1}$
b_2 (95% CB)	--	-1.844 (-2.118,-1.571)	$(V\text{-}\mu s)^{-1}$
D_M	44.34	0.2519	$(°C)^2$
R_M^2	0.961	0.9998	--
$R_{adj,M}^2$	0.9545	0.9996	--
rms_M	2.719	0.251	°C

Once the best fit associated with each function type model has been established, these remaining curve fits must then be compared to help determine the best candidate to represent the total integral calibration curve. Upon first examination of the errors associated with the fitting algorithm, it can be seen that both the rational fit and the exponential fit have values of $D_M < 0.3\ (°C)^2$ and $rms_M < 0.27\ (°C)$ This signifies that both of these fit errors are sufficiently small for a quality curve fit. The values of the same statistical outputs associated with the third-degree polynomial fit are slightly larger than its other fit counterparts with $D_M = 1.082\ (°C)^2$ and $rms_M = 0.502\ (°C)$. Though this could be an indicator that this fit model can be rejected, the observed values of R_M^2 and $R_{adj,M}^2$ show that the polynomial fit does explain the variation in calibration data well. In fact, these parameters are on the order of $R_M^2 \approx 0.99$ and $R_{adj,M}^2 \approx 0.99$ for all function fits.

Since it has been established that none of the fit models can be rejected purely based on the goodness-of-fit statistics, the numerical uncertainty of each fit must be compared. As in the previous analysis involving the slope calibration, the confidence bounds on the fitted model coefficients can be graphically observed from the 95% prediction bounds for a given regression model. These bounds on the third-degree polynomial curve fit, rational function curve fit, and the bi-exponential curve fit are respectively shown in Figs. 4.2.17-4.2.18. The polynomial approximation possesses a larger amount of uncertainty than the rational and exponential models. The prediction interval for this particular model is wide at lower temperatures and becomes narrower at increased temperatures. The large uncertainty band indicates that the polynomial regression model is the worst case fit to represent the calibration curve and most likely will be rejected. However, in order to be thorough, this function relationship should be testing in the transient sense. On the other hand, the exponential fit seems to present the best fit choice. The prediction uncertainty intervals are sufficiently small and also the trend of this fit reflects the exponential nature of the rise and decay portion of the phosphor emission, which gives the model physical significance. Even after noting these observations about the fit quality, it is still necessary to evaluate the effectiveness of each steady-state model when applied in a transient setting. These results are seen in Section 4.3.

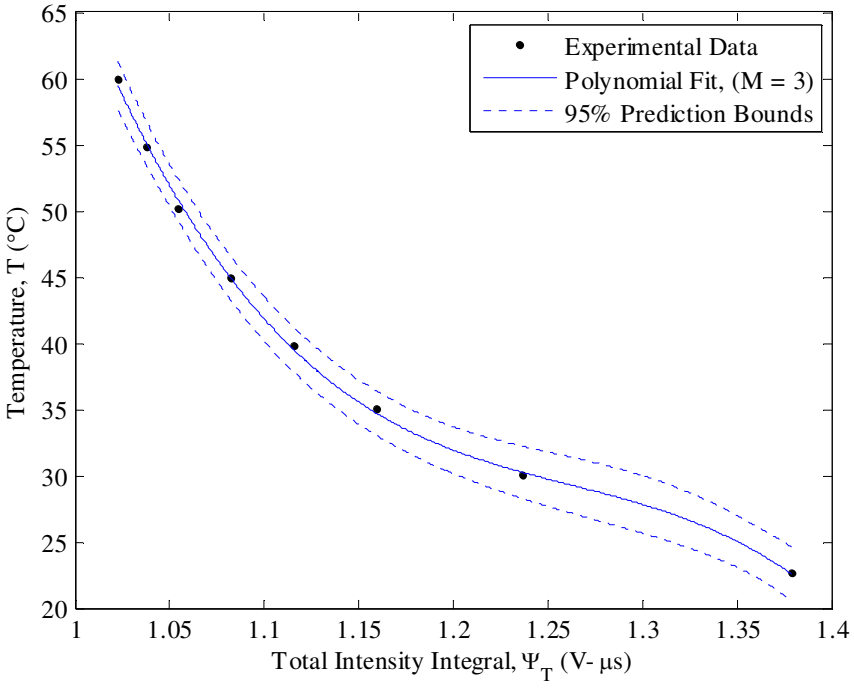

Figure 4.2.17: Prediction Bounds on Polynomial Function Fit to Observed Total Integral Calibration Data (Table 4.2.7, Fit 2)

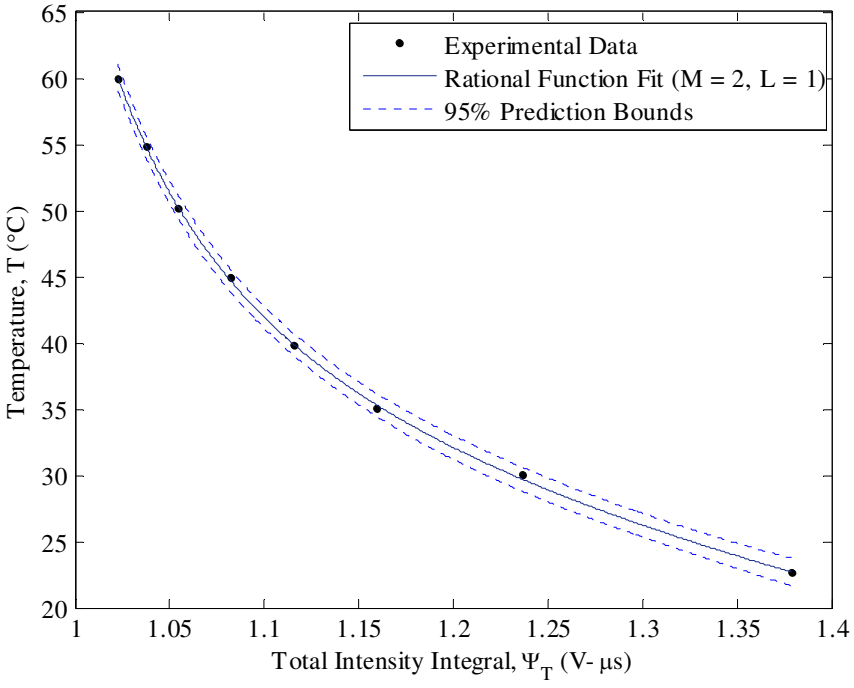

Figure 4.2.18: Prediction Bounds on Rational Function Fit to Observed Total Integral Calibration Data (Table 4.2.8, Fit 1)

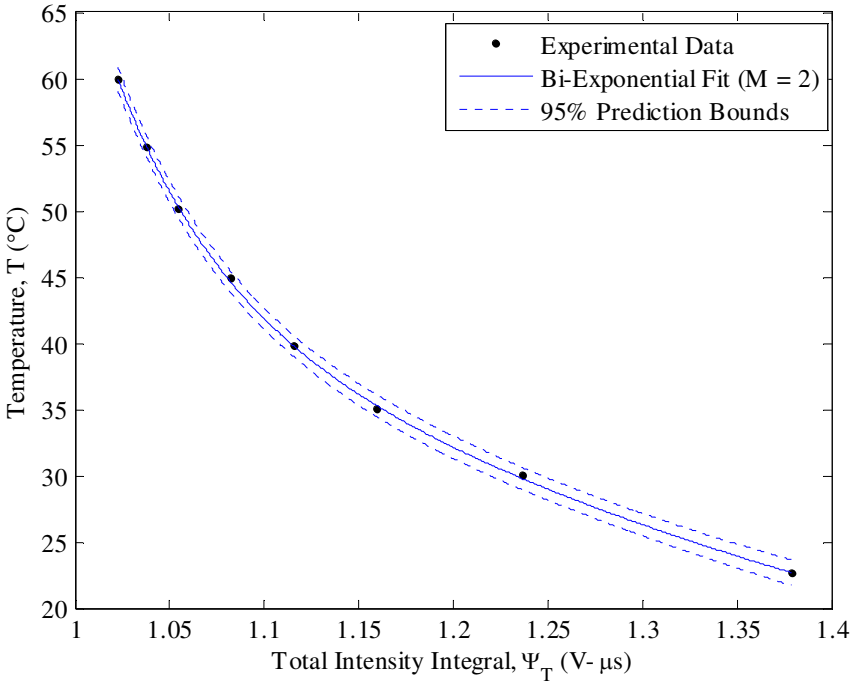

Figure 4.2.19: Prediction Bounds on Bi-Exponential Fit to Observed Total Integral Calibration Data (Table 4.2.9, Fit 2)

4.3 Transient Results

In order to completely investigate the effectiveness of the various steady-state models associated with both the slope calibration technique and the total integral calibration technique, it is necessary to apply each curve fit in a transient setting to resolve the temperature history of the test sample. In order to instill a sense of randomness in the collected transient data, three tests, which involve monitoring three different temperature trends, were conducted across three different days. This verifies that the design of both calibration methods display continued reliability over time with minimal sensitivity to external influences. As previously summarized in Table 3.3.1, the transient experimental runs involve a constant heating process, a sample cool down process and an arbitrary heating/cooling process which only span temperature measurements in the calibration range of $T \in [Room\ Temp, 60°C]$. This can be observed in Figs. 4.3.1-4.3.3, which present the RTD temperature measurements collected during each transient test. The time of data collection for each transient experiment varies, and thus the total amount of collected waveforms, each averaged over $N = 512$ successive shots, also varies. The constant heating case, seen in Fig. 4.3.1, takes place

over 5807 s, which corresponds to 2052 phosphor signal acquisitions. The experimentation time of the cool down run is 3251 s, which corresponds to 1149 collected signals. Finally, the last transient case, which involves the heating/cooling pattern presented in Fig. 4.3.3, spans a total time of 5424 s in which a total of 1907 signal waveforms are collected. For each transient case, this translates to a phosphor emission approximately being collected every 2.8 s. These collected waveforms represent the phosphor responses that are used in the transient analysis.

For each transient run, both calibration parameters of interest are resolved from the integrated curve of each phosphor emission, $\Psi(t)$. In the slope calibration method, the calibration value η is resolved from the linear portion of $\Psi(t)$, which pertains to the region of $t \in [18\mu s, 30\mu s]$. In the total integral calibration method, the value Ψ_T is resolved from the final value of each $\Psi(t)$ trajectory. These processes have been previously described in detail in Chapter 2.2B and 2.2C. These resolved calibration parameters are used in the final step of the best fit analysis in order to determine the best steady-state regression model to represent the calibration curve. The fit model equations in question for the slope calibration method and the total integral calibration method can be seen in Table 4.3.1 and Table 4.3.2, respectively. Each equation for the given technique is evaluated using the applicable calibration values. This produces a predicted temperature measurement at each time step of the transient run. The accuracy of a particular function is evaluated from the residuals, R, between the RTD temperature data and the predicted temperature response as given by

$$R(t) = T_{RTD}(t) - T_P(t),\ t \in [0, t_{\max}], \tag{4.3.1}$$

where T_{RTD} denotes the actual temperature value and T_P represents the predicted temperature response.

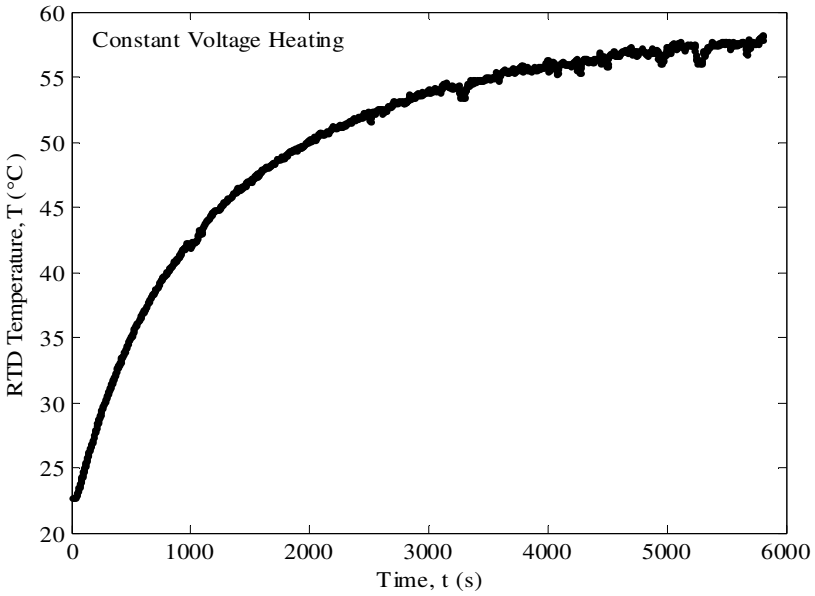

Figure 4.3.1: RTD Temperature Data for Constant Voltage Heating Transient Case

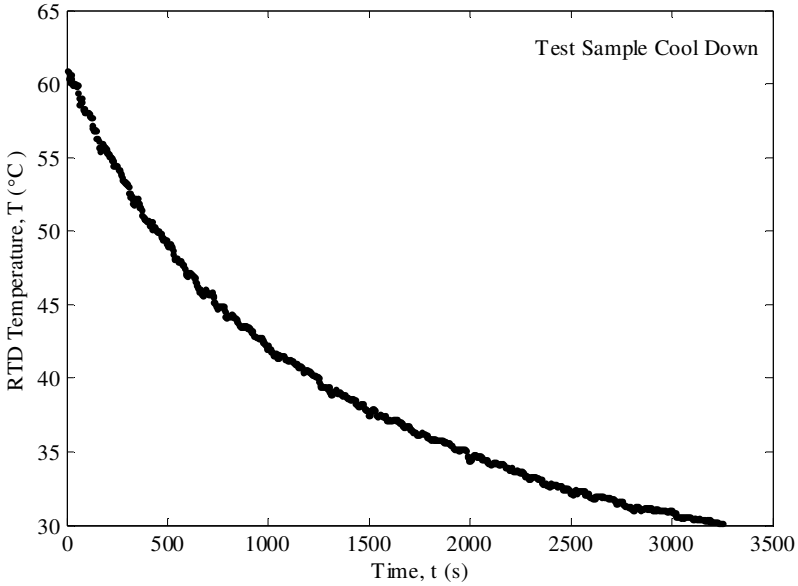

Figure 4.3.2: RTD Temperature Data for Sample Cool Down Transient Case

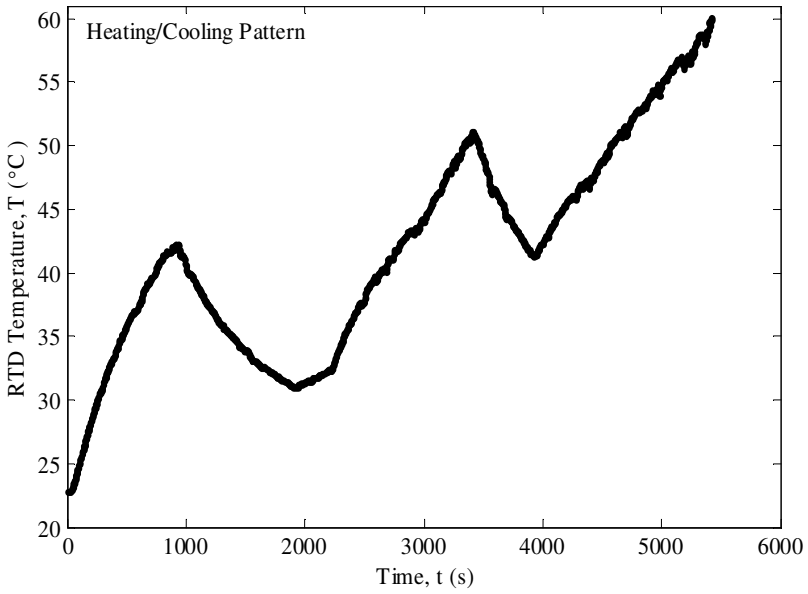

Figure 4.3.3: RTD Temperature Data for Heating/Cooling Pattern Transient Case

Table 4.3.1: Fitted Function Equations from Slope Calibration Technique

	Function Model Type	Fitted Equation	
a)	Polynomial	$T(\eta) = -2.774(10^7)\eta^3 + 4.831(10^6)\eta^2 - 2.828(10^5)\eta + 5592$	(°C)
b)	Rational	$T(\eta) = \dfrac{-1893\eta^2 + 222.7\eta - 6.212}{\eta - 0.0471}$	(°C)
c)	Exponential	$T(\eta) = 3344e^{-80.96\eta} + 1.487(10^{17})e^{-753.1\eta}$	(°C)

Table 4.3.2: Fitted Function Equations from Total Integral Calibration Technique

	Function Model Type	Fitted Equation	
a)	Polynomial	$T(\Psi_T) = -1557\,\Psi_T^3 + 5897\,\Psi_T^2 - 7480\,\Psi_T + 3207$	(°C)
b)	Rational	$T(\Psi_T) = \dfrac{-23.72\,\Psi_T^2 + 69.4\,\Psi_T - 40.28}{\Psi_T - 0.9246}$	(°C)
c)	Exponential	$T(\Psi_T) = 2.002(10^9)e^{-18.22\,\Psi_T} + 288.3e^{-1.844\,\Psi_T}$	(°C)

The first set of transient temperature profiles are generated using the slope calibration technique. Figures 4.3.4a-f present the temperature histories and corresponding local residuals predicted from the third-degree polynomial regression model for the three proposed test cases (i) constant heating, (ii) cooling, and (iii) oscillating test, respectively. From observing these curves it can be seen that the model consistently underestimates the temperature value by approximately 2.5°C – 3.0°C. Though this issue might be resolved by employing some type of constrained least-squares approximation, this fit is rejected because the polynomial model does not sufficiently reflect the physics of the calibration curve. This specific function overfits the data and does not provide a generalized trend. Though the statistical outputs seen in Table 4.2.3 indicate a high quality fit, the actual model describes the fluctuations (error) in the observed data more than the underlying relationship.

In order to indicate the best fit option between the remaining slope calibration models, the trends in the local residual plots must be observed and directly compared. An ideal residual curve oscillates around the zero value with small amplitude. Figures 4.3.5a-f present results derived from using the rational representation given in Table 4.3.1(b) for the identical three test cases associated with Fig 4.3.5 for the slope calibration method. The rational function form clearly outperforms the corresponding polynomial expression in both reconstruction of the transient temperature and local residual behaviors. A similar set of remarks can be made when comparing the bi-exponential calibration equation results (Figs. 4.3.6a-f) with the polynomial calibration equation results (Figs. 4.3.4a-f). The temperature predictions of the rational function model shown in Fig. 4.3.5 (Table 4.3.1b) and the bi-exponential model presented in Fig. 4.3.6 (Table 4.3.1c) provide suitable results, especially for the constant heating and sample cool down cases. A general observation of these transient runs is that rational function model tends to minimize about the zero value for a larger portion of the constant heating and sample cool down cases. However, the residuals of both models dive to distinct values in the lower temperature range. The difference in this behavior between the fits lies in the fact that the residual shift in the exponential model has an amplitude of ±1°C whereas the maximum of the rational function deviation is generally on the order of ±0.5°C. This observation is not surprising considering the exponential model prediction bounds widen to a larger degree than that of the rational function model in this temperature range. Another minor differentiating aspect of the models can be seen in the predictions of the heating/cooling pattern seen in last plots of Fig. 4.3.5c and Fig. 4.3.6c. Though both models tend to underestimate the relatively “quick” changes of the exact temperature curve, the deviations are generally smaller in the rational function model.

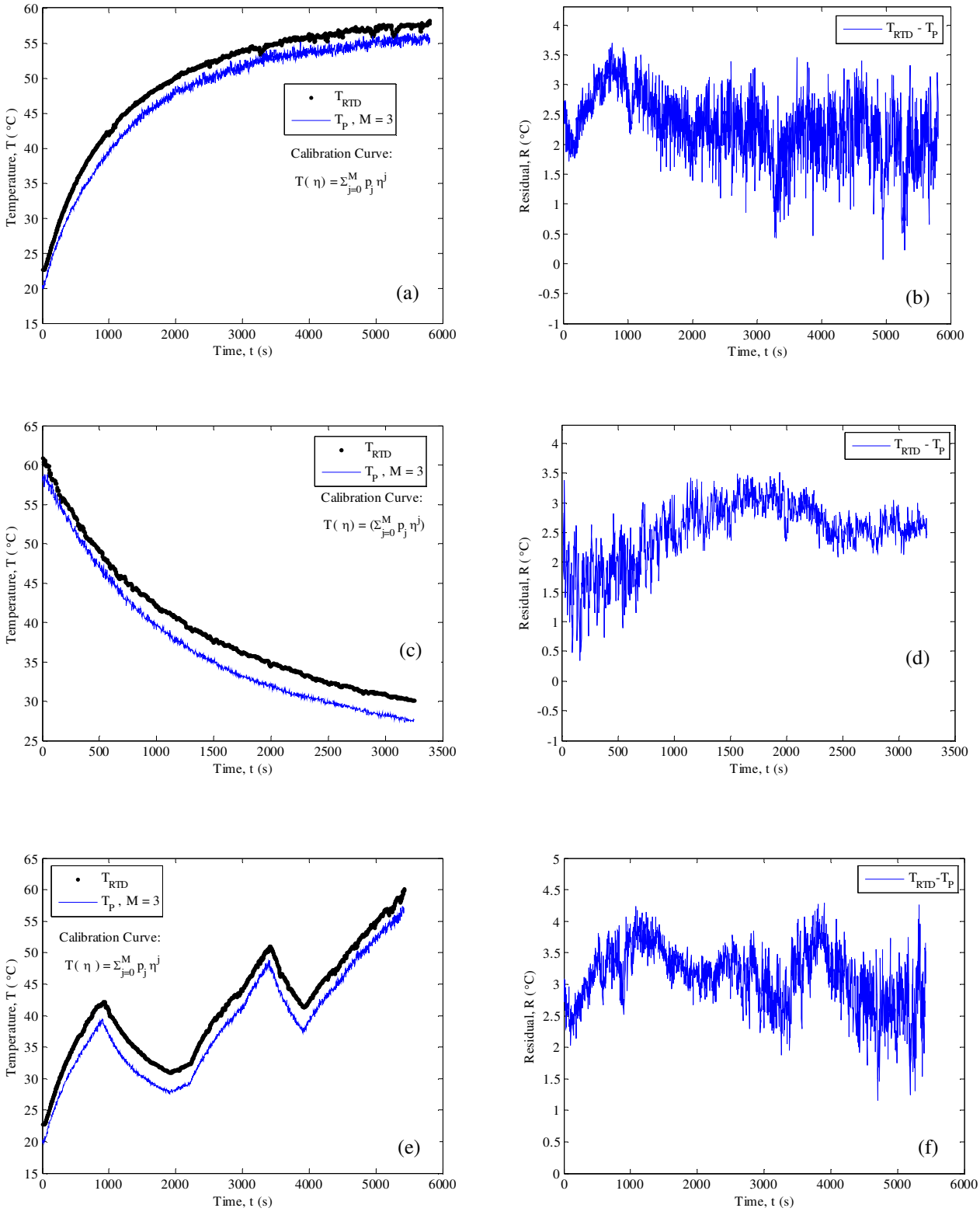

Figure 4.3.4: All Transient Temperature Predictions and Corresponding Residuals Resolved Using Polynomial Regression Model of Slope Calibration (Coefficients found in Table 4.3.1a) for (a-b) Constant Heating, (c-d) Sample Cool Down, and (e-f) Heating/Cooling Pattern

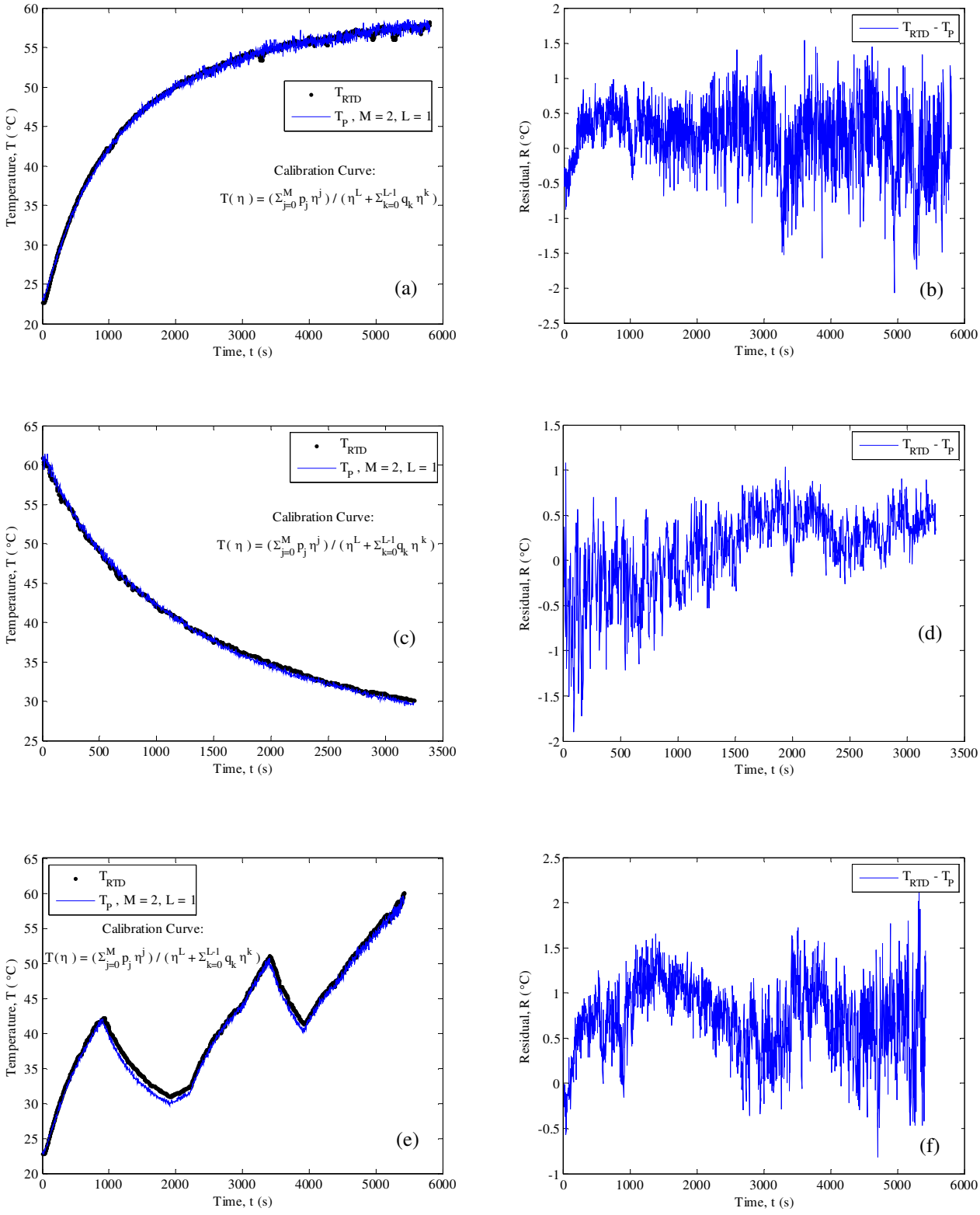

Figure 4.3.5: All Transient Temperature Predictions and Corresponding Residuals Resolved Using Rational Function Regression Model of Slope Calibration (Coefficients found in Table 4.3.1b) for (a-b) Constant Heating, (c-d) Sample Cool Down, and (e-f) Heating/Cooling Pattern

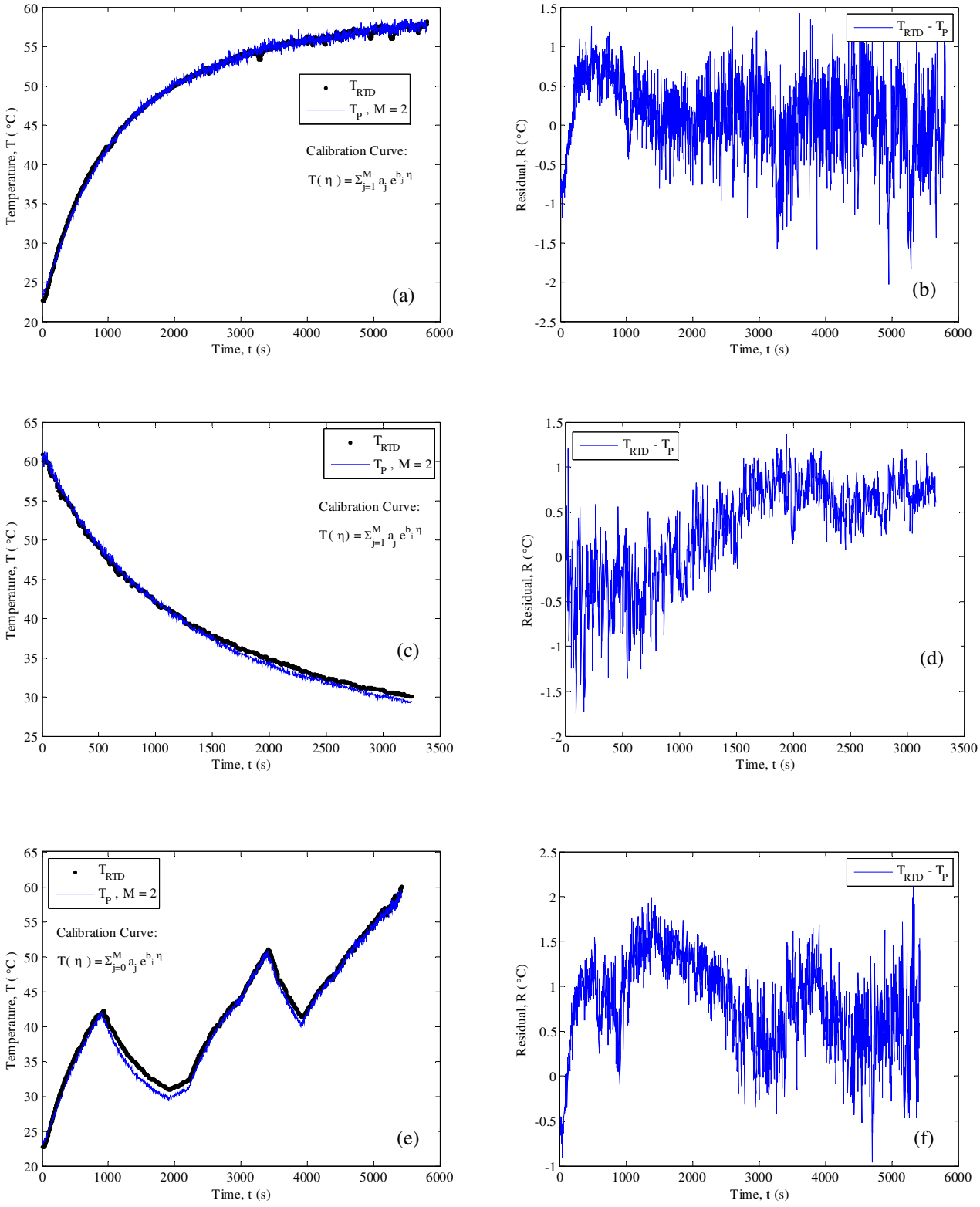

Figure 4.3.6: All Transient Temperature Predictions and Corresponding Residuals Resolved Using Exponential Regression Model of Slope Calibration (Coefficients found in Table 4.3.1c) for (a-b) Constant Heating, (c-d) Sample Cool Down, and (e-f) Heating/Cooling Pattern

The plots seen in Figs. 4.3.7-4.3.9 are all generated using the total integration calibration technique. Here, Figs. 4.3.7-4.3.9 describe the various calibration functional forms applied to the similar test data described using the slope calibration method. The regression functions involved in this analysis are found in Table 4.3.2(a-c). At first glance of all the transient temperature profiles, it can be seen that all the function models produce relatively good predictions.

Unlike the slope calibration technique, there are no glaring offsets in the polynomial model as noted in Fig. 4.3.7. Upon closer investigation of Fig. 4.3.7, however, there are still undesirable characteristics associated the polynomial function results. The residual plots for all the three transient test cases appear to be slightly periodic in nature. Though it is less pronounced than in the slope calibration method (Fig. 4.3.4), this behavior is still indicative that the calibration model does not have physical meaning. The over and under behavior of the fitted curve defines the randomness in the steady-state calibration data points instead of explaining the generalized system relationship.

On the other hand, both the rational function regression model (Fig. 4.3.8) and the bi-exponential regression model (Fig. 4.3.9) are used to accurately reproduce the temperature measurement history. The residuals for both the constant heating and sample cool down curves generally oscillate around zero at an interval of approximately ±0.5°C for the lower temperatures and ±1.0°C for the higher temperature values. Both models do tend to underestimate the temperatures in the heating/cooling patter by about 0.5°C. This can be observed from both residual plots. Thus, it can be said that both of these functional models produce almost synonymous results from the both the goodness-of-fit statistics, seen in the steady-state portion of the results section, and the transient results seen below. Either curve would make a good choice as the calibration curve.

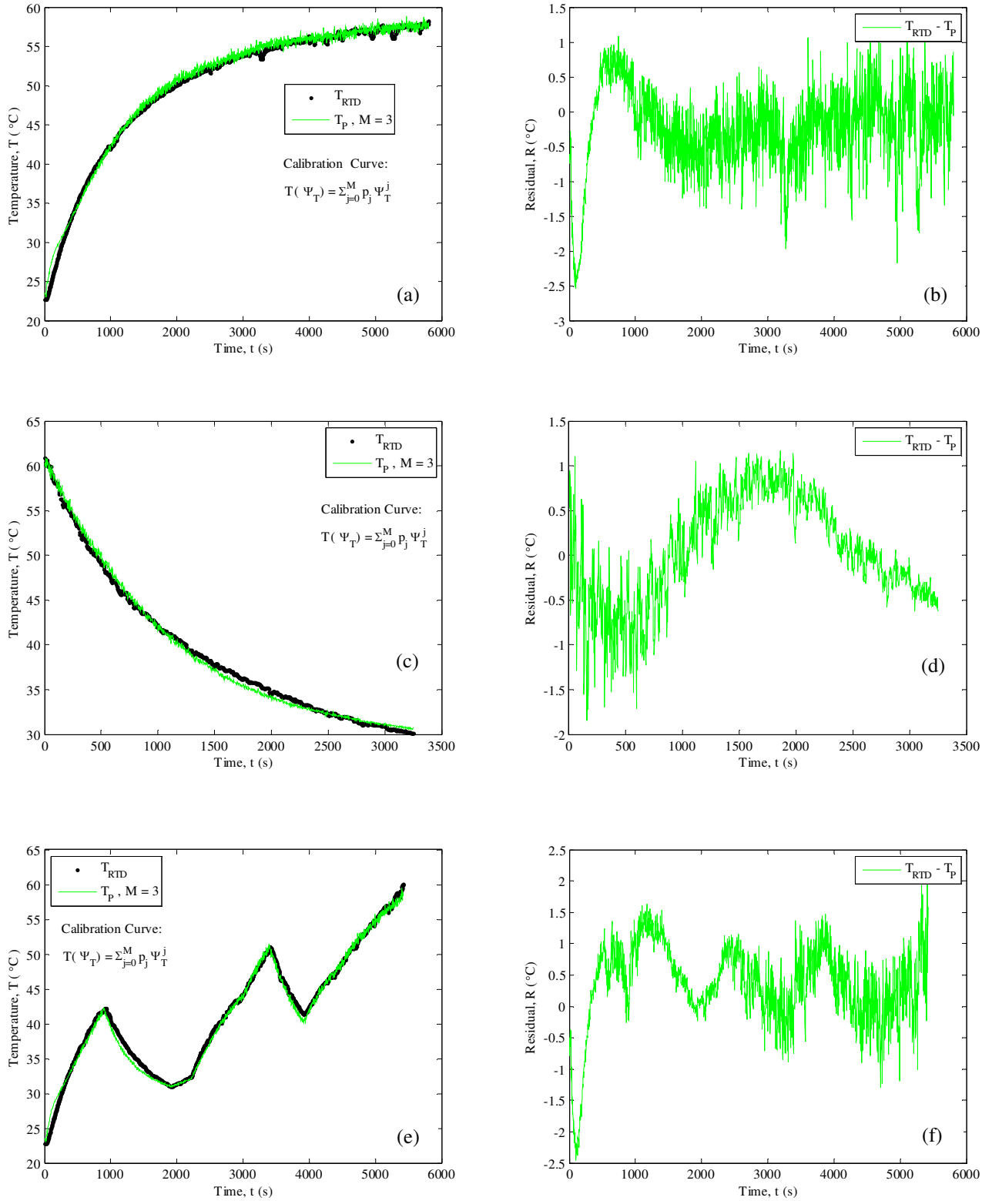

Figure 4.3.7: All Transient Temperature Predictions and Corresponding Residuals Resolved Using Polynomial Regression Model of Total Integral Calibration (Coefficients found in Table 4.3.2a) for (a-b) Constant Heating, (c-d) Sample Cool Down, and (e-f) Heating/Cooling Pattern

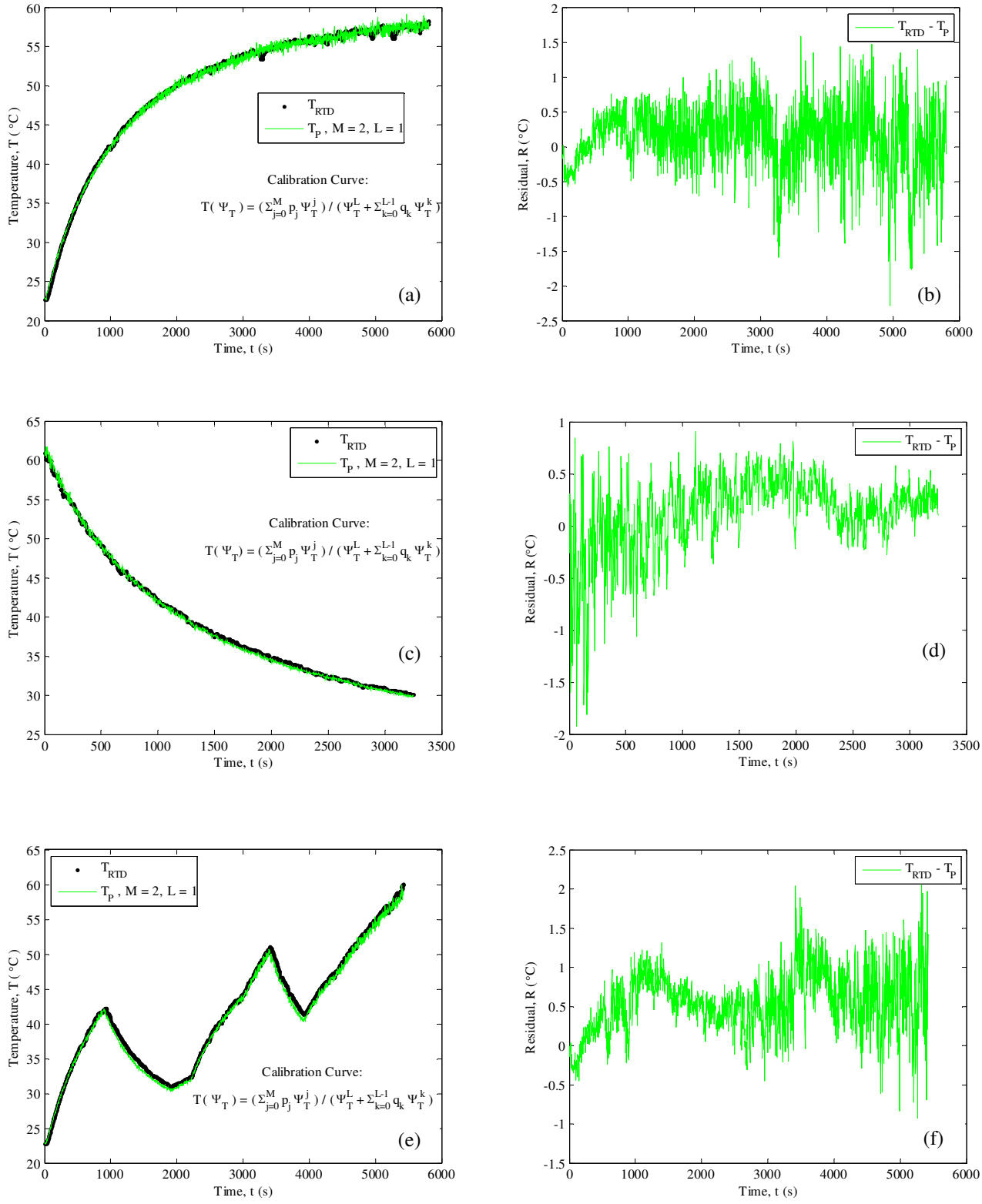

Figure 4.3.8: All Transient Temperature Predictions and Corresponding Residuals Resolved Using Rational Function Regression Model of Total Integral Calibration (Coefficients found in Table 4.3.2b) for (a-b) Constant Heating, (c-d) Sample Cool Down, and (e-f) Heating/Cooling Pattern

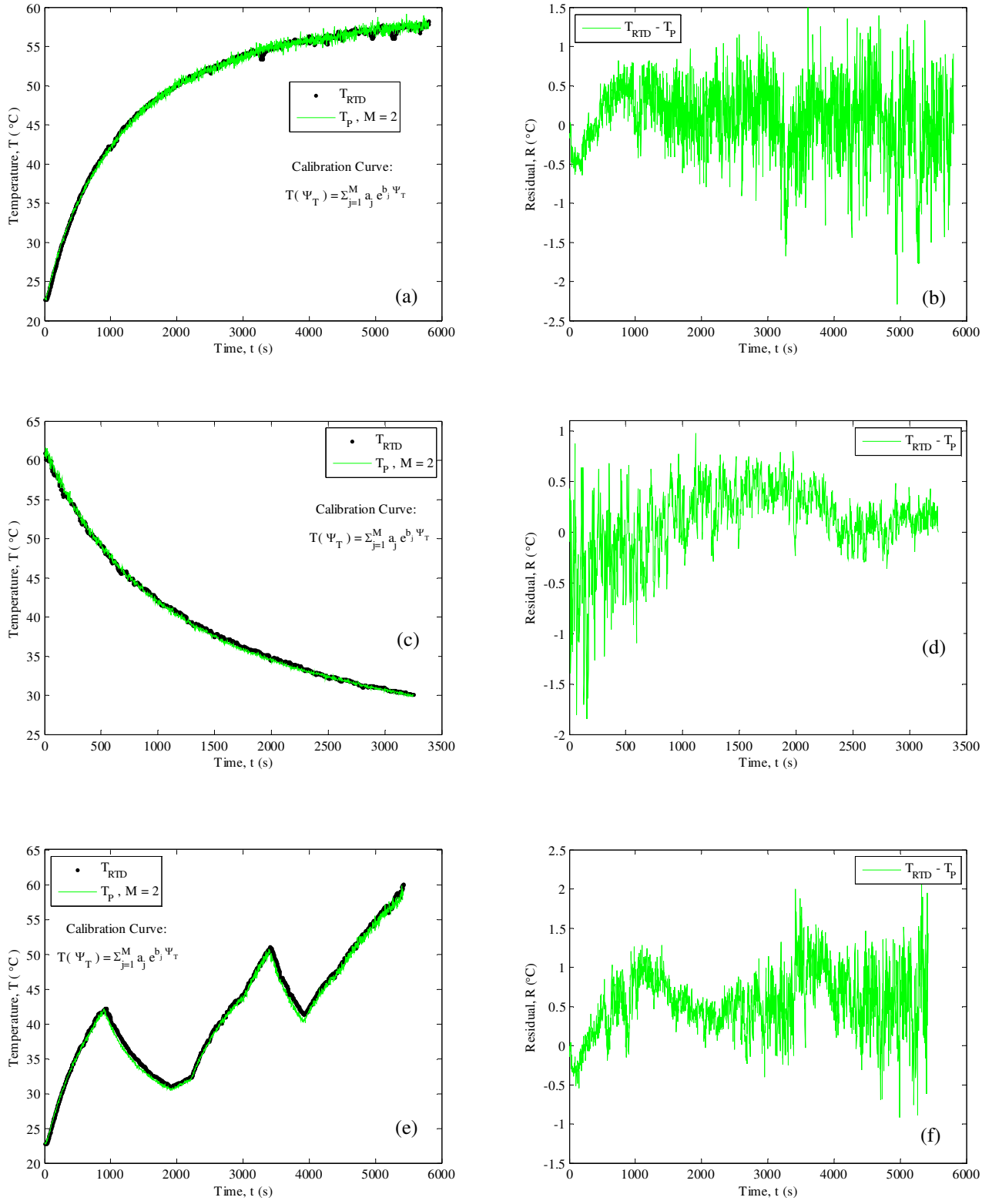

Figure 4.3.9: All Transient Temperature Predictions and Corresponding Residuals Resolved Using Exponential Function Regression Model of Total Integral Calibration (Coefficients found in Table 4.3.2c) for (a-b) Constant Heating, (c-d) Sample Cool Down, and (e-f) Heating/Cooling Pattern

As a final assessment of the proof-of-principle concept, Tables 4.3.3 and 4.3.4 provide the RMS of each calibration model and calibration equation based on the choice of expansion. This RMS value is calculated such that

$$RMS = \sqrt{\frac{\sum_{i=1}^{m} R_i^2}{m}}, \quad i = 1,2,...,m, \tag{4.2.22}$$

where R is the residual defined in Eq. (4.3.1) and m represents the number of data points present in each of the transient runs. Table 4.3.3 illustrates that the slope calibration model possess a significantly higher RMS error when compared to the total calibration model given in Table 4.3.4.

To close this section, the new concept of the total integral calibration method has been validated in an experimental setting to possess good sensitivity to temperature. It has been established as a reliable method to resolve temperature measurements in both steady-state and transient environments. The calibration process requires little computational effort and is derived from the raw physical data of the phosphor emission.

Table 4.3.3: RMS Error Associated with Each Regression Function Model of All Transient Heating Test Cases for the Slope Calibration

Slope Calibration Equation (Table 4.3.1)	RMS (°C)
(A) Heating	
Polynomial	2.3597
Rational	0.5094
Bi-Exponential	0.5236
(B) Cooling	
Polynomial	2.5725
Rational	0.4564
Bi-Exponential	0.6345
(C) Oscillatory	
Polynomial	3.1397
Rational	0.8296
Bi-Exponential	0.9581

Table 4.3.4: RMS Error Associated with Each Regression Function Model of All Transient Heating Test Cases for the Total Integral Calibration Method

Total Integral Calibration Equation (Table 4.3.2)		RMS (°C)
(A) Heating		
	Polynomial	0.6562
	Rational	0.4902
	Bi-Exponential	0.4845
(B) Cooling		
	Polynomial	0.5961
	Rational	0.3854
	Bi-Exponential	0.3856
(C) Oscillatory		
	Polynomial	0.7458
	Rational	0.6817
	Bi-Exponential	0.6825

Chapter 5: Conclusions and Recommendations

The overall goal of this work was to provide an alternate approach of TP calibration to temperature that eliminates the complexities associated with resolving lifetime measurements from non-ideal experimental data using a first-order system assumption for the emission decay. To this end, the two proposed calibration methods did not require knowledge of key parameters prior to data processing, nor did they involve complicated numerical schemes that attempt to fit data in the low signal-to-noise region of the phosphor response. The slope calibration technique and the total integral calibration technique were developed without making any previous assumptions as to the nature of the phosphor fluorescence signal. In fact since both concepts evolved from an investigation into phosphor emission behavior, these approaches of TP calibration to temperature are based in the actual physics of the luminescing material instead of processes of data reduction. One key concept associated with complex dynamical systems, such as fluorescence, is that phase-plane techniques can be used to extract qualitative information about how characteristic behaviors of the system change in time. This idea was employed in this work in order to gain physical insight into the experimental data. In Chapter 2, it was shown through the integrated phase portrait that indeed the phosphor exhibited regions of temperature dependence in advantageous portions of the emission signal. The slope calibration parameter was resolved from the maximum intensity portion of the fluorescence curves (high signal-to-noise ratio), and the total integral calibration parameter was taken from the largest integrated intensity value of the integral curve. In addition, the calibration processes involve integrating the full phosphor response signal. Since integrating is a naturally smoothing process, the raw collected intensity data can be used without digital filtering.

Chapter 3 presented the setup of a physical experiment which was used to validate the calibration procedures formulated in Chapter 2. A summary of the instrumentation used during testing as well as the systematic progression of data collection through the experimental arrangement was detailed. In order to determine the merit of the proposed calibration methods, the experimental process was two-fold. First, the phosphor emission response was recorded at different steady-state temperatures in order to form a calibration curve. Second, the phosphor was heated under transient conditions and the calibration technique was applied to resolve the temporal temperature history of the test sample. The experimental procedure associated with both test types was provided.

Chapter 4 detailed the experimental results for both alternate calibration techniques. From this work, it was noted that despite producing statistical outputs indicative of a high quality fit to the observed calibration data, a polynomial expansion presented an unsuitable functional relationship of the calibration curve. This was common for both the slope calibration and the total integral calibration. Instead, a rational function fit or a bi-exponential function fit must be employed. Using either regression model as the representative calibration curve, it was shown that the steady-state results for both the slope calibration technique and the total integral calibration technique were used to accurately resolve the temporal history of a test sample.

5.1 Experimental Conclusions and Remarks

In order to justly conclude this work, it is necessary to compare the performance of the alternative techniques to the traditional calibration method that was described in Chapter 2.1. Thus, all the phosphor emission curves used in this experiment to validate the slope method and the total integral method were also analyzed in terms of the emission decay behavior. These results are given in Appendix A.1. It can be seen that both the techniques formulated in this thesis do not only offer a less numerically intensive option for phosphor calibration but further provide a more accurate calibration of the TP La_2O_2S:Eu for the full temperature range of $T \in [RoomTemp, 60°C]$. The decay time method does not possess temperature sensitivity in the desired range of this application. In fact, it was only able to resolve transient temperature measurements on the same order of uncertainty as the new methods in a temperature range $T \in [RoomTemp, 35°C]$, which is approximately a 10°C-15°C temperature span. It can be observed in Figs. A.1.5-A.1.7, that once outside the temperature sensitivity range, the local residuals corresponding to each transient test increased approximately one, or in certain cases two, orders of magnitude from the start time of the experiment to the end time.

It has been established that both the slope value and the total integral value offer a more effective means of calibration compared to the decay method. However, there are certain inherent characteristics of the integral method that offer practical advantages. In using this technique, all assumptions concerning the behavior of the phosphor response are removed. This is a differentiating factor from both the slope and the lifetime measurements which rely on curve fitting techniques to resolve the respective calibration parameter, which once again must be subject to curve fitting techniques in order to develop a calibration curve. This in turn increases the generalized error associated with the calibration model. Instead, the only numerical manipulation of the raw physical experimental

data involves integrating the signal. In addition to this being a less rigorous computational method, integration is a naturally smoothing process which helps to eliminate the emission signal noise that originates from the high frequency nature of any general optical system.

5.2 Potential Applications of Research

The outcome of this work is highly encouraging and indicates that these techniques could be found useful in certain applications. The simplified calibration model was shown to be flexible and robust in non-ideal testing scenarios. The stability of the generated data was not affected by nearby construction, which occasionally caused the experimental rig to be disturbed by vibrational interferences without any form of shielding. Therefore, the technique presented might be ideal in certain mechanical settings where it is necessary to monitor equipment temperatures. The fact that this procedure could be applied using a fairly low cost experimental arrangement is another attractive feature for situations of this regard.

Another possible application avenue would explore the idea of using TPs in the inverse heat conduction problem. Recently, Frankel et al.[48] and Elkins et al.[49] proposed a new calibration-based approach for estimating the surface heat flux by calibrating the entire sample using a known heat flux source. Additionally, Frankel et al.[50] proposed a similar concept for estimating the surface temperature. In this new method, the surface temperature is required during the calibration stage of the analysis. TP thermometry could be used in this stage to provide the information to resolve the required surface temperature needed for the proposed inverse calibration method for estimating surface temperatures in the unknown test case.

Prior to extending the results of this work to be used in such a capacity, it is necessary to make certain investigative improvements to the experimental scheme. As previously mentioned, this intensity-dependent calibration method requires that the optical detector (PMT) remain at a fixed, minimized distance from the sample. In the hostile thermal environments where inverse heat methods are the most applicable, however, the temperatures might exceed thresholds of the optics and cause damage to the instrumentation. A high heat capacity optical fiber would need to be employed in these scenarios such that it would be able to remain fixed above the sample. Employing a fiber optic with a dual light guide (excitation/detection) would be best for ensuring that the measured phosphor target remains constant.

Another important issue that must be resolved for this application is the speed of data collection. Throughout this thesis, the various times associated with each step of the data acquisition process has been indicated. It was stated there is a characteristic time for the completion of the signal-averaging procedure, $N(\Delta t)$, and there is a certain time value associated with the oscilloscope data transfer process. Therefore, the method to decrease this total time of transfer is two-fold. First, the amount of waveform signal averages could be decreased. This was explored as a sideline of the work in this thesis and the results are summarized in Appendix A.2. The investigation indicated, however, that the time of waveform averaging is not the limiting factor. In this regard, the oscilloscope transfer time must be decreased. In future work, the result of collecting less data values must be investigated. Though this would normally drastically effect the uncertainty in the estimated calibration parameter from the signal, the nature of the integral calibration method might decrease these ill effects. Given the high promise of this method, significant effort should be dedicated to the further development of this calibration technique to extend the use of this simplified model to other practical scenarios.

LIST OF REFERENCES

[1]Yen, W.M., Shionoya, S., and Yamamoto, H., *Phosphor Handbook*, 2nd ed., CRC Press, Taylor and Francis Group, New York, 2007, Chaps. 1,2.

[2]Khalid, A.H., and Kontis, K., "Thermographic Phosphors for High Temperature Measurements: Principles, Current State of the Art and Recent Applications," *Sensors*, Vol. 8, No. 9, 2008, pp. 5673-5744.

[3]Leverenz, H.W., *An Introduction to Luminescence of Solids*, John Wiley & Sons, New York, 1950.

[4]Allison, S.W., and Gillies, G.T., "Remote Thermometry with Thermographical Phosphors: Instrumentation and Applications," *Review of Scientific Instruments*, Vol. 68, No. 7, 1997, pp. 2615-2650.

[5]Skoog, D.A., Holler, F.J., and Crouch, S.R., *Principles of Instrumental Analysis,* 6th ed., Thompson Brooks/Cole, Canada, 2007, Chap. 15.

[6]Bell, J.H., Schairer, E.T., Hand, L.A., and Mehta, R.D., "Surface Pressure Measurements Using Luminescent Coatings," *Annual Review of Fluid Mechanics,* Vol. 33, 2001, pp. 155-206.

[7]Becker, R.S., *Theory and Interpretation of Fluorescence and Phosphorescence*, John Wiley & Sons, New York, 1969, Chap. 1.

[8]Urbach, F., Nail, N.R., and Pearlman, D., "The Observation of Temperature Distributions and of Thermal Radiation by Means of Non-Linear Phosphors," *Journal of the Optical Society of America,* Vol. 39, No. 12, 1949, pp. 1011-1019.

[9]Bradley III, L.C., "A Temperature-Sensitive Phosphor Used to Measure Surface Temperature in Aerodynamics," *The Review of Scientific Instruments,* Vol. 24, No. 3, 1953, pp. 219-220.

[10]Goldberg, P., *Luminescence of Inorganic Solids,* Academic Press, New York, 1966.

[11]Feist, J.P., "Development of Phosphor Thermometry for Gas Turbines," Ph.D. Dissertation, The University of London, London, UK, 2001.

[12]Heyes, A.L., Seefeldt, S., and Feist, J.P., "Two-Colour Phosphor Thermometry for Surface Temperature Measurement," *Optics and Laser Technology,* Vol. 38, 2006, pp. 257-265.

[13]Dieke, G.H., and Crosswhite, H.M., "The Spectra of the Doubly and Triply Ionized Rare Earths," *Applied Optics,* Vol. 2, No. 7, 1963, pp. 675-686.

[14]Goss, L.P., Smith, A.A., and Post, M.E., "Surface Thermometry by Laser-Induced Fluorescnece," *Review of Scientific Instruments,* Vol. 60, No. 12, 1989, pp. 3702-3706.

[15]Allison, S.W., Boatner, L.A., and Gillies, G.R., "Characterization of High-Temperature Thermographic Phosphors: Spectral Properties of $LuPO_4$Dy(1%),Eu(2%)," *Applied Optics,* Vol. 34, No. 25, 1995, pp. 5624-5627.

[16]Kusama, H., Sovers, O.J., and Yoshioka, T., "Line Shift Method for Phosphor Temperature Measurements," *Japanese Journal of Applied Phyics,* Vol. 15, No. 12, 1976, pp. 2349-2358.

[17]Choy, K.L., Feist, J.P., Heyes, A.L., and Su, B., "Eu-Doped Y_2O_3 Phosphor Films Produced by Electrostatic-Assisted Chemical Vapor Deposition," *Journal of Material Research,* Vol. 14, No. 7, 1999, pp. 3111-3114.

[18]Yap, S.V., Ranson, R.M., Cranton, W.M., and Koutsogeorgis, D. "Decay Time Characteristics of La_2O_2S:Eu and La_2O_2S:Tb for Use Within an Optical Sensor for Human Skin Temperature Measurement," *Applied Optics*, Vol. 47, No. 27, 2008, pp. 4895-4899.

[19]Mannik, L., Brown, S.K., and Campbell, S.R., "Phosphor-Based Thermometry of Rotating Surfaces," *Applied Optics,* Vol. 26, No. 18, 1987, pp. 4014-4017.

[20]Feist, J. P., Heyes, A. L., and Seefeldt, S., "Thermographic Phosphors for Gas Turbines: Instrumentation Development and Measurement Uncertainties," *11th International Symposium on Application of Laser Techniques to Fluid Mechanics,* Lisbon, Portugal, 2002.

[21]Curie, D. *Luminescence in Crystals,*John Wiley & Sons, New York, 1960.

[22]Chambers, M.D., and Clarke, D.R., "Doped Oxides for High-Temperature Luminescence and Lifetime Thermometry," *Annual Review of Materials Research,* Vol. 39, 2009, pp. 325-359.

[23]Figliola, R.S., and Beasley, D.E., *Theory and Design for Mechanical Measurements,* 4th ed., John Wiley & Sons, New York, 2006.

[24]McKeever, S.W.S, *Thermoluminescence of Solid*, Cambridge University Press, Cambridge, UK, 1985.

[25]Liu, Z., Hunt, H., Vaughan, M., Hostetler, C., McGill, M., Powell, K., Winker, D., and Hu, Y., "Estimating Random Errors due to Shot Noise in Backscatter Lidar Observations," *Applied Optics*, Vol. 45, No. 18, 2006, pp. 4437-4447.

[26]Hale, P.D., Wang, C.M., Remley, K.A., and Wepman, J.D., "Compensation of Random and Systematic Timing Errors in Sampling Oscillloscopes," *Instrumentation and Measurement*, Vol. 55, No. 6, 2006, pp. 2146-2154.

[27]Allison, S.W., and Gillies, G.T. "Phosphor Thermometry Signal Analysis and Interpretation," Oak Ridge National Laboratory, 2013.

[28]Brübach, J., Janicka, J., and Dreizler, A., "An Algorithm for the Characterisation of Multi-Exponential Decay Curves," *Optics and Lasers in Engineering*, Vol. 47, No. 1, 2009, pp. 75-79.

[29]Dowell, L.J., and Gillies, G.T., "Errors Cased by Baseline Offset and Noise in the Estimation of Exponential Lifetimes," *Review of Scientific Instruments*, Vol. 62, No. 1, 1991, pp. 242-243.

[30]Sun, T., Zhang, Z.Y, Grattan, K.T.V., and Palmer, A.W., "Analysis of Double Exponential Fluorescence Decay Behavior for Optical Temperature Sensing," *Review of Scientific Instruments*, Vol. 68, No. 1, 1997, pp. 58-63.

[31]Dowell, L.J., and Gillies., G.T., "Precision Limits of Lifetime Estimation Algorithms as Determined by Monte Carlo Simulation: A Comparison of Theory and Experiment," *Review of Scientific Instruments*, Vol. 59, No. 8, 1988, pp. 1310-1315.

[32]Riseberg, L.A., and Moos, H.W., "Multiphonon Orbit-Lattice Relaxation of Excitated States of Rare-Earth Ions in Crystals," *Physical Review,* Vol. 174, No. 2, 1968, pp. 429-438.

[33]Struck, C.W. and Fonger, W.H., "Unified Model of the Temperature Quenching of Narrow-Line and Broad-Band Emissions," *Journal of Luminescence,* Vol. 10, 1975, pp. 1-10.

[34]Weber, M.J., "Multiphonon Relaxation of Rare-Earth Ions in Yttrium Orthoaluminate," *Physical Review,* Vol. 8, No. 1, 1973, pp. 54-64.

[35]Poincaré, H., "Mémoire sur les courbes définies par une equation différentielle (II)," *Journal de mathématiques pures et appliquées*, 1882, pp. 251-296.

[36]Zhao, F. "Computational Dynamics: Modeling and Visualizing Trajectory Flows in Phase Space," *Annals of Mathematics and Artifical Intelligence,* Vol. 8, No.3-4, 1993, pp. 285-300.

[37]Broomhead, D.S., and King, G.P., "Extracting Qualitative Dynamics from Experimental Data," *Physica D: Nonlinear Phenomena,* Vol. 20, No. 2, 1986, pp. 217-236.

[38]Abelson, H., Eisenberg, M., Halfant, M., Katzenelson, J., Sacks, E., Sussman, G.J., Wisdom, J., and Yip, K., "Intelligence in Scientific Computing," *Communications of the ACM,* Vol. 32, No. 5, 1989, pp. 546-562.

[39]Tchernichovski, O., and Golani, I., "A Phase Plane Representation of Rat Exploratory Behavior," *Journal of Neuroscience Methods,* Vol. 62, 1995, pp. 21-27.

[40]Tannor, D. J., *Introduction to Quantum Mechanics,* University Science Books, 2007, Chap. 5.

[41]Peterka, F., and Vacik, J., "Transition to Chaotic Motion in Mechanical Systems with Impacts," *Journal of Sound and Vibration,* Vol. 154, No. 1, 1992, pp. 95-115.

[42]Zhao, F. "Extracting and Representing Qualitative Behavior of Complex Systems in Phase Space," *Artificial Intelligence,* Vol. 69, No. 1, 1994, pp. 51-92.

[43]Frankel, J.I., and Keyhani, M., "Moving Low-Pass Gauss Filter with Automatically Defined Influence Region for Diffusive Studies," *Journal of Thermophysics and Heat Transfer,* Vol. 26, No. 1, 2012, pp. 176-181.

[44]Ranson, R.M., Evangelou, E., and Thomas, C.B., "Modeling of Fluorescence Lifetime of Y_2O_3:Eu," *Applied Physics Letters,* Vol. 72, No. 21, 1996, pp. 2663-2664.

[45]*Photomultiplier Tubes: Basics and Applications,* 3rd ed., Hamamatsu Photonics, 2006, Chap. 4.

[46]Taylor, J.R., *An Introduction to Error Analysis: The Study of Uncertainties in Physical Measurements*, Oxford University Press, 1982.

[47]Gerald, C.R., Wheatley, P.O., *Applied Numerical Analysis*, 5th ed., Addison-Wesley Publishing Company, 1994.

[48]Frankel, J.I., Keyhani, M., Elkins, B.E., "Surface Heat Flux Prediction Through Physics-Based Calibration, Part 1: Theory," *50th Aerospace Sciences Meeting and Aerospace Exposition,* Nashville, TN, 2012 (Paper Number: AiAA-2012-0222).

[49]Elkins, B. E., Keyhani, M., and Frankel, J. I., "Surface Heat Flux Prediction Through Physics-Based Calibration, Part 1: Experimental Verification," *50th Aerospace Sciences Meeting and Aerospace Exposition,* Nashville, TN, 2012 (Paper Number: AiAA-2012-0223).

[50]Frankel, J.I., Allison, S.W., Beshears, D.L., "Design of Phosphor Thermometry System for Transient High Heat Flux Surface Thermometry," *58th International Instrumentation Symposium*, San Diego, CA, 2012.

APPENDIX

A.1 Summary of Results from Lifetime Calibration Method

The main purpose of this work involved validating the two alternative calibration techniques, which used the slope of the linear portion of the integrated curve and the total integrated intensity as the respective calibration parameters. However, it is still important to analyze the collected experimental data using the lifetime calibration method that was described in Chapter 2.1 so that all methods may be compared. The following results were generated using the same procedure as the experimental results in Chapter 4.

As previously indicated in Fig. 2.1.3, the collected emission data did not obey a mono-exponential decay and was better characterized as a bi-exponential decay. Two arbitrary emission decays at two different temperatures were chosen to further demonstrate this behavior. As can be seen in Fig. A.1.1, each signal is comprised of two distinct decays. The short-lived decay that occurs at the onset of the decay process is denoted as τ_1. At increased times a longer decay, denoted by τ_2, dominates the emission. Both values were evaluated from all observed phosphors signals in order to determine the best choice of the calibration parameter. The short decay results are summarized in Table A.1.1 and Fig. A.1.2. The long decay results are summarized in Table A.1.2 and Fig. A.1.3. Based on these results, it was noted that the short decay was characterized by large amounts of uncertainty across the entire temperature region. Thus, the long decay time, τ_2, was chosen as the experimental calibration parameter.

The calibration curve was developed using the average, $\bar{\tau}_2$, of all the decay times resolved at a given temperature step. It can be seen from the generated calibration curve presented in Fig. A.1.4, that at elevated temperatures the decrease in the decay time becomes less pronounced until at approximately 50°C the sensitivity drops off completely and the temperature effects can no longer be resolved. Thus, the calibration curve was generated for $T \in [RoomTemp, 50^{\circ}C]$. The statistical outputs corresponding to this curve fit can be seen in Table A.1.3. This calibration curve was then applied to the transient test cases. These results can be found in Figs. A.1.5-A.1.7.

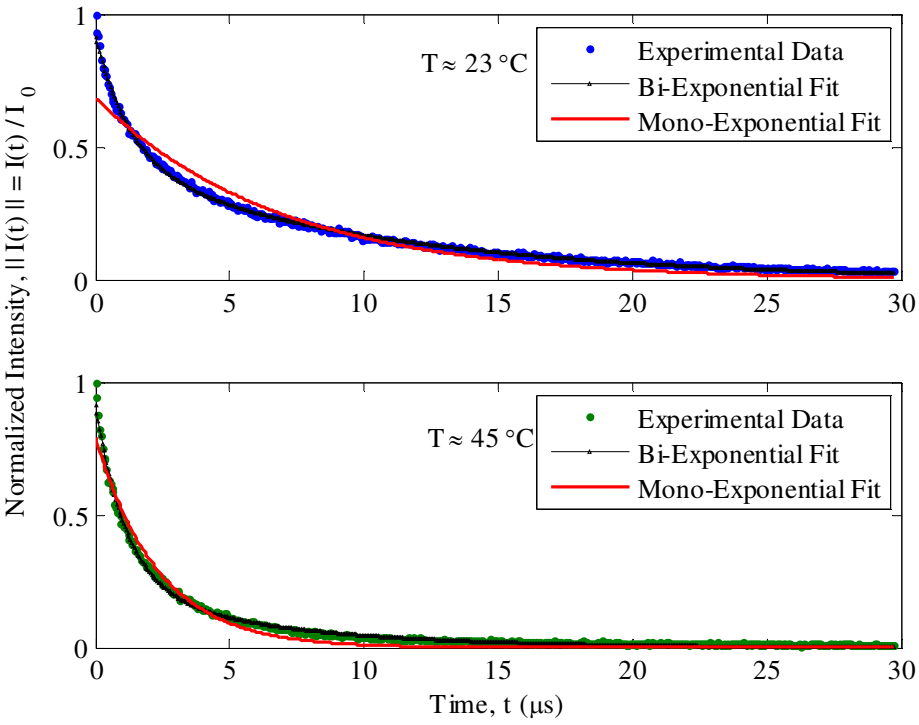

Figure A.1.1: Two Characteristic Emission Decays Taken at Various Temperatures to Show the Bi-Exponential Behavior

Table A.1.1: Short Decay Time Results

$\overline{T}_{RTD}$	$\overline{\tau}_1$	σ (μs)	σ^2 (μs)^2	±2σ
22.6 °C	0.9606 μs	0.0419	0.0018	±0.084 μs
30.0 °C	0.7450 μs	0.0496	0.0025	±0.099 μs
35.0 °C	0.6209 μs	0.0505	0.0025	±0.101 μs
39.8 °C	0.5447 μs	0.0507	0.0026	±0.101 μs
44.9 °C	0.5082 μs	0.0519	0.0027	±0.104 μs
50.1 °C	0.5086 μs	0.0533	0.0028	±0.107 μs
54.9 °C	0.5169 μs	0.0555	0.0031	±0.111 μs
59.9 °C	0.5257 μs	0.0476	0.0023	±0.095 μs

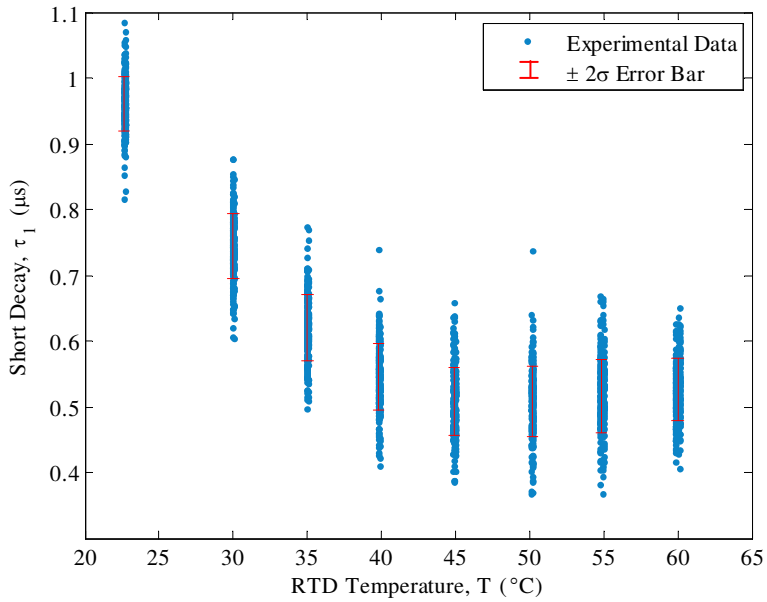

Figure A.1.2: Short Decay Time Calibration Error Bars Overlaid on All Short Decay Time-Temperature Values

Table A.1.2: Long Decay Time Results

$\overline{T}_{RTD}$	$\overline{\tau}_2$	σ (μs)	σ^2 (μs)^2	±2σ
22.6 °C	9.0704 μs	0.1294	0.0167	±0.2588 μs
30.0 °C	5.7694 μs	0.1462	0.0214	±0.2923 μs
35.0 °C	4.3513 μs	0.1242	0.0154	±0.2484 μs
39.8 °C	3.5670 μs	0.1246	0.0155	±0.2492 μs
44.9 °C	3.1739 μs	0.1309	0.0171	±0.2619 μs
50.1 °C	3.0491 μs	0.1414	0.0200	±0.2828 μs
54.9 °C	3.0759 μs	0.1749	0.0306	±0.3498 μs
59.9 °C	3.1716 μs	0.1683	0.0283	±0.3376 μs

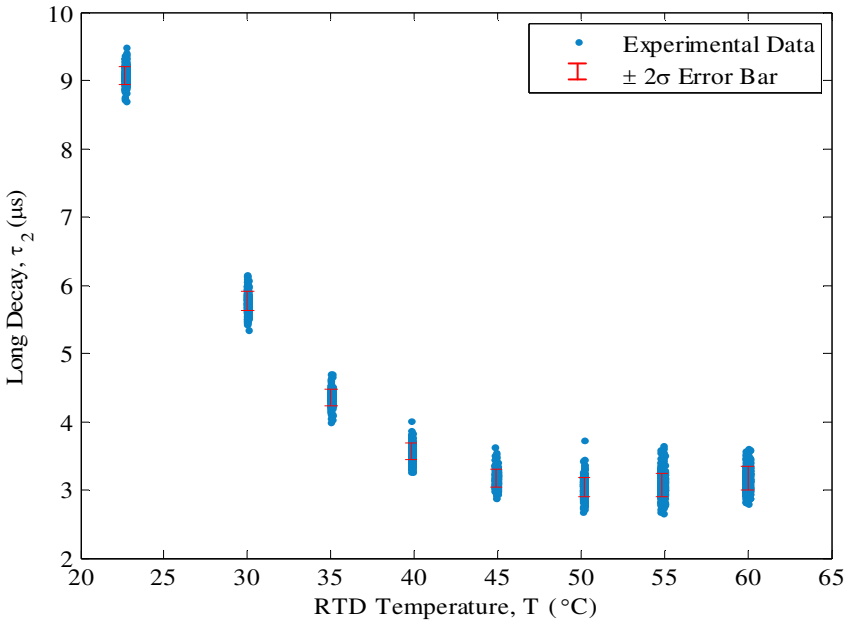

Figure A.1.3: Long Decay Time Calibration Error Bars Overlaid on All Short Decay Time-Temperature Values

Table A.1.3: Tabulated Results from Bi-Exponential Curve Fit Using Lifetime Calibration Data

	Bi-Exponential Fit for τ_2	Units
a_1 (95% CB)	$1.131(10^6)$ ($-1.693(10^7)$,$1.919(10^7)$)	(°C)
a_2 (95% CB)	52.95 (40.19,65.72)	(°C)
b_1 (95% CB)	-3.808 (-9.116,1.501)	μs^{-1}
b_2 (95% CB)	-0.09512 (-0.1352,-0.05508)	μs^{-1}
D_M	1.36	$(°C)^2$
R_M^2	0.9973	--
$R_{adj,M}^2$	0.9932	--
rms_M	0.8245	°C

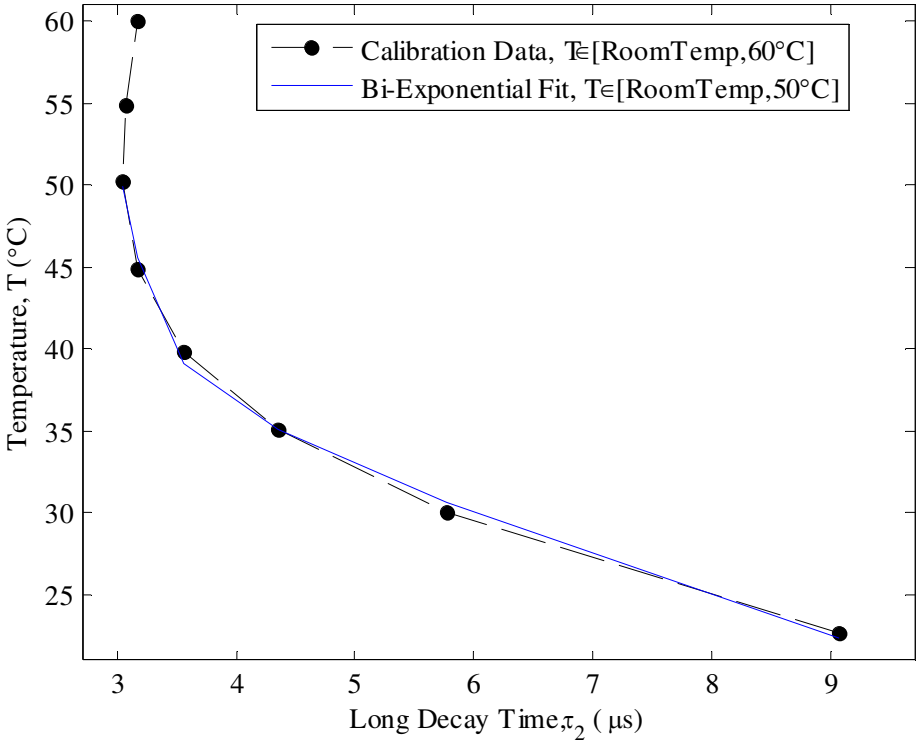

Figure A.1.4: Bi-Exponential Calibration Curve Using the Lifetime Technique

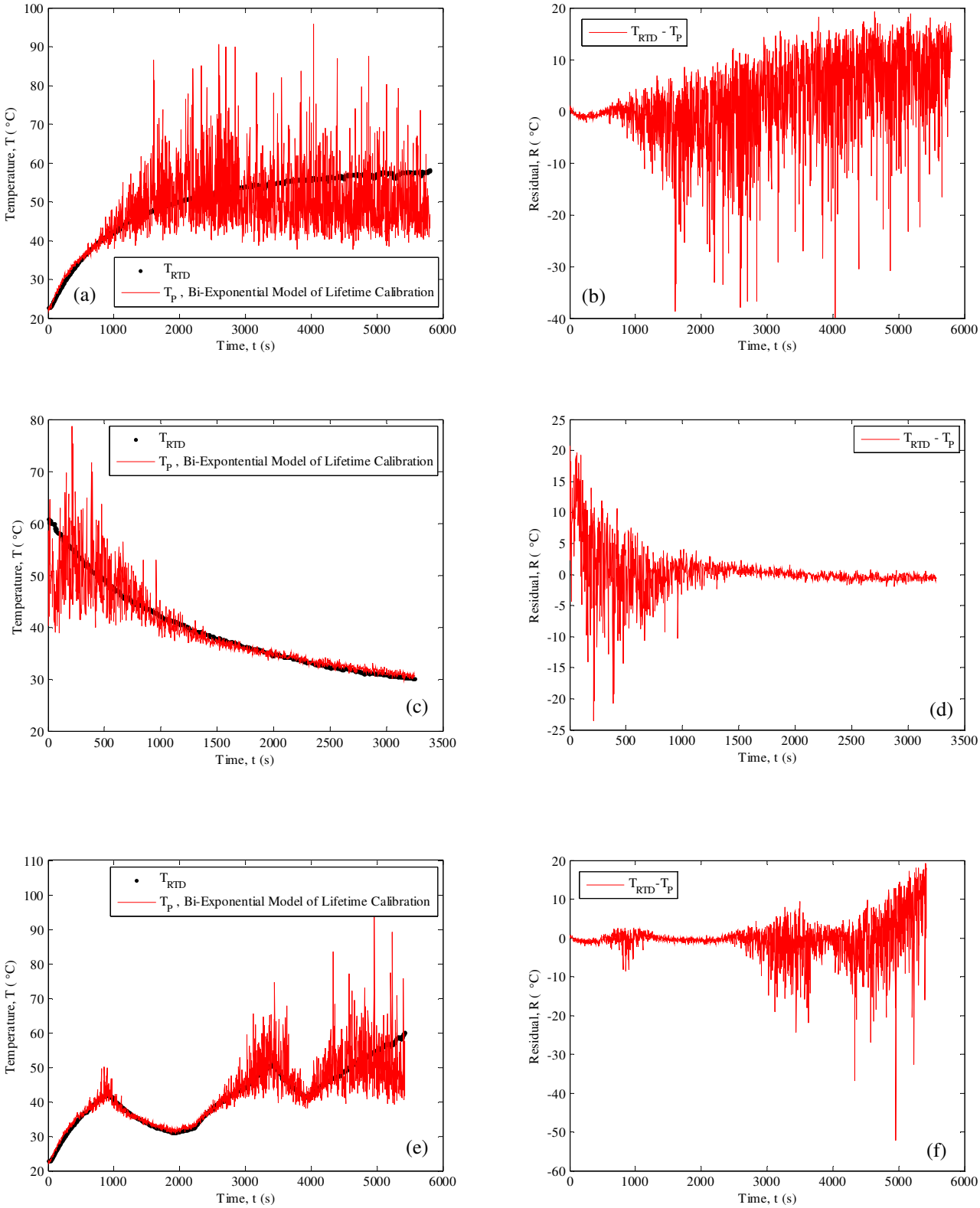

Figure A.1.5: All Transient Temperature Predictions and Corresponding Residuals Resolved Using Bi-Exponential Function Regression Model of Lifetime Decay (Coefficients found in Table A.1.3), (a-b) Heating, (c-d) Cooling, and (e-f) Oscillating

A.2 Investigation into Shot-Averaging

A side investigation of this experiment involved examining the effects of using different average counts, N, in the total integral calibration method to resolve transient temperature profiles. This was carried out by conducting two separate transient cases of constant voltage heating. In the first test, phosphor signals averaged over $N = 128$ waveforms were obtained, and in the second test phosphor signals averaged over $N = 32$ waveforms were obtained. As in the experiment seen in the main body of this thesis, the time base of a given emission spanned $\Delta t = 100\ \mu s$. Also, the waveform record for each collected emission contained $m' = 2000$ time-voltage data pairs. The times of data collection associated with these experiments can be seen in Table A.2.1. It was originally postulated that using smaller average counts would decrease the total oscilloscope transit time of a phosphor emission so that the integrated intensity calibration technique could be applied in faster transient scenarios. However, by observing Table A.2.1, it can be seen that the contribution of the averaging time, $N(\Delta t)$, remains a negligible component of total oscilloscope transit time. Thus, a better method to decrease the total transit time might lie in collecting a smaller waveform record, m'. This would need to be investigated in future work.

The temperature prediction profile and corresponding local residuals can be seen in Figs. A.2.1a-d and Figs. A.2.2a-d. All transient profiles are generated using the total integral technique. Both the rational function representation of the calibration curve (Table 4.3.2b) and the bi-exponential function representation of the calibration curve (Table 4.3.2c) are used. From all results, it can be seen that the functional relationships produced from the steady state calibration data averaged over $N = 512$ waveforms do not translate well to other average counts. Therefore, separate calibration data would need to be taken to generate a calibration curve corresponding to each average count.

Table A.2.1: Data Collection Times Associated with Different Average Counts

N	$N(\Delta t)$ (ms)	m'	t_{test} (s)	Approximate Oscilloscope Transit Time of Emission (s)
32	3.2	1175	2517	2.1
128	12.8	1105	2513	2.3

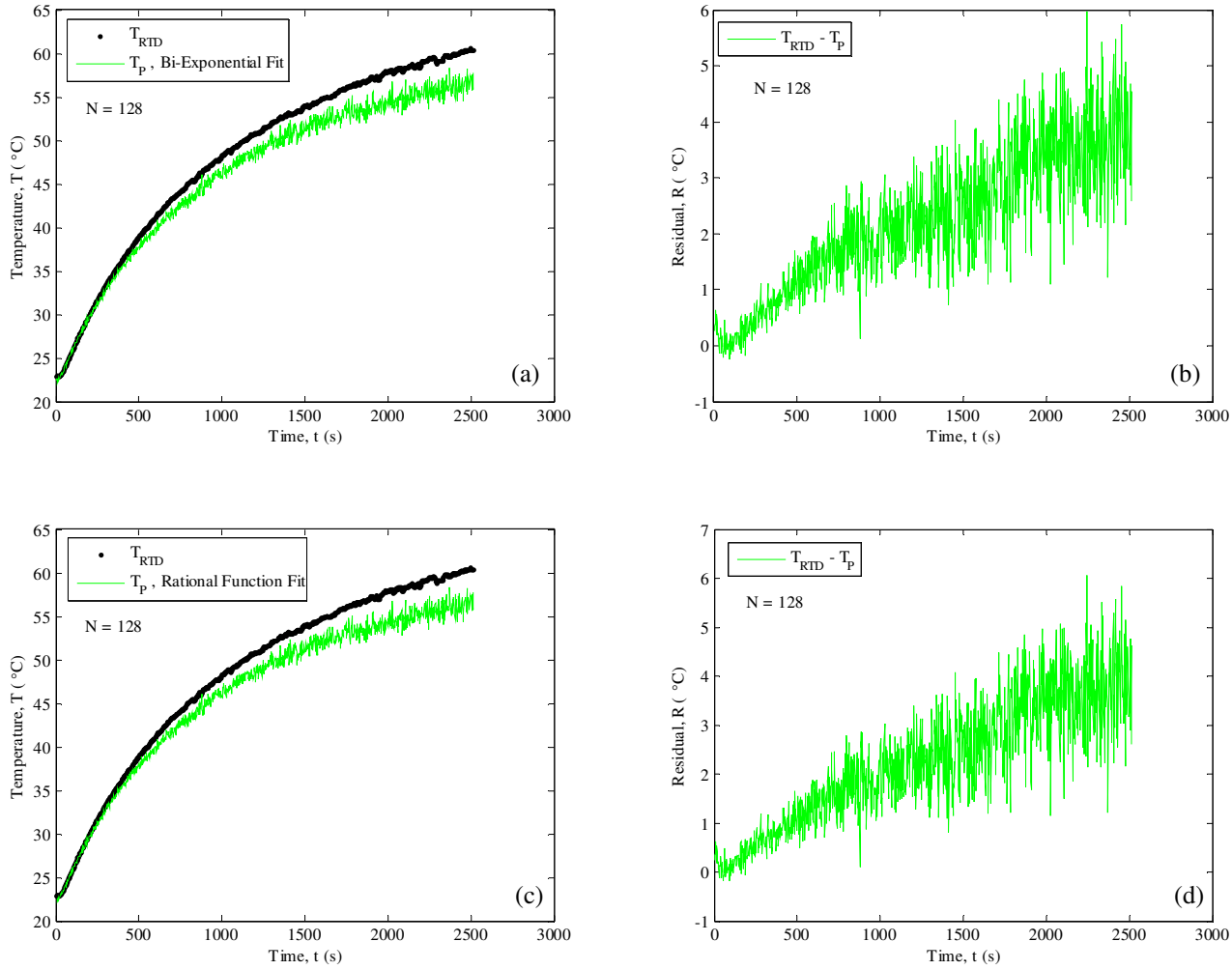

Figure A.2.1: Transient Temperature Predictions and Corresponding Residuals Generated Using Total Integral Calibration for N=128 Emission Average Count, (a-b) Bi-Exponential Fit Coefficients: Table 4.3.2c; (c-d) Rational Fit Coefficients: Table 4.3.2b

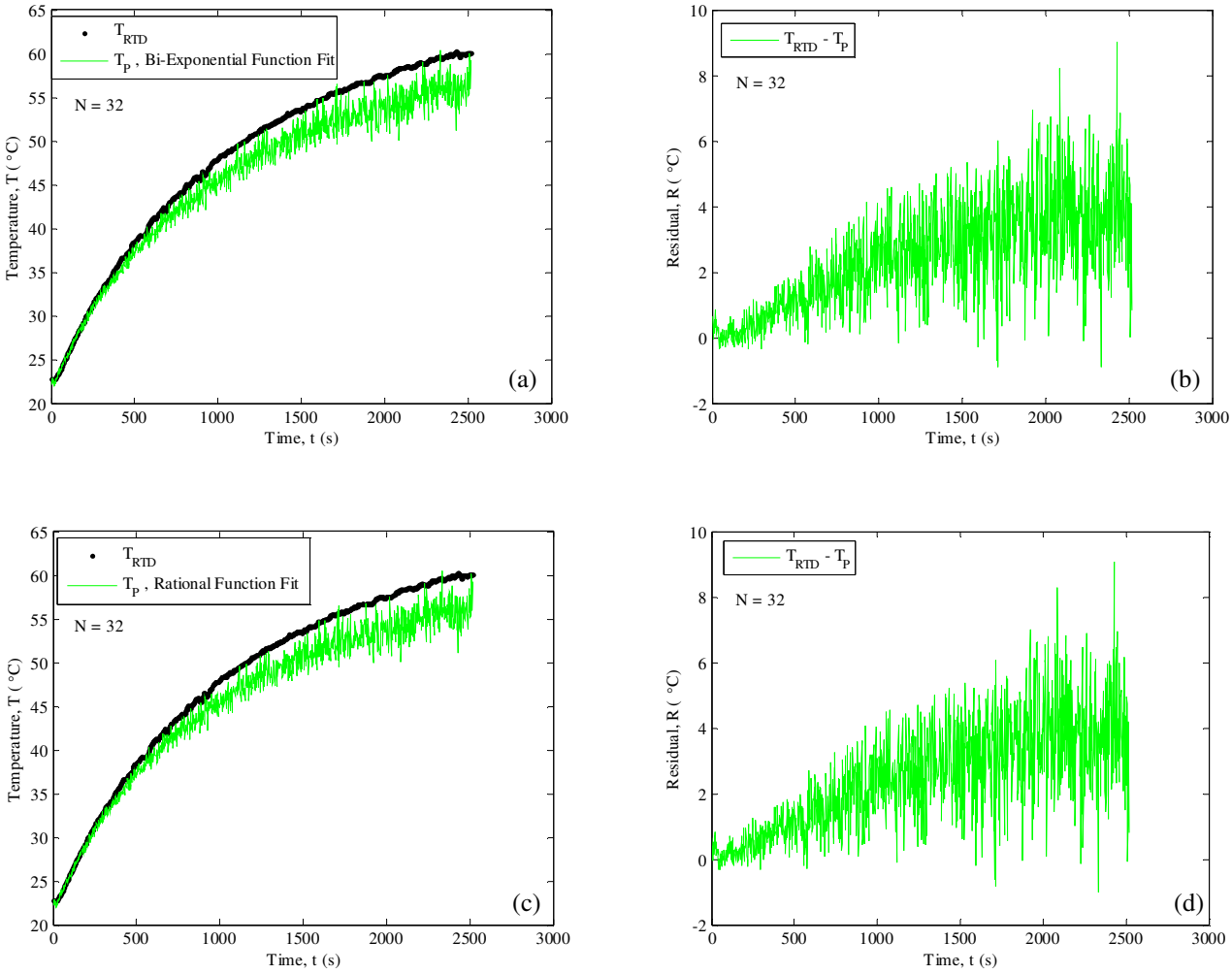

Figure A.2.2: Transient Temperature Predictions and Corresponding Residuals Generated Using Total Integral Calibration for N=32 Emission Average Count, (a-b) Bi-Exponential Fit Coefficients: Table 4.3.2c; (c-d) Rational Fit Coefficients: Table 4.3.2b

A.3 Oscilloscope Data Acquisition Code

```
/*
 * Written by Kelsey Winstead
 *
 * This source code is written to communicate remotely with the Agilent InfiniiVision DSO-X-3034A
 * oscilloscope via a USB connection.  It is written for Visual Studio 2010 in C#.  This VisaComLib
 * must be added to the Reference section of whichever Console Application it is being used in.
 * This program recalls setup_2 that was saved manually on the oscilloscope using the Save softkey,
 * and it turns on the waveform generator.  It acquires the waveform in the AVERAGE acquistion mode.
 * The average count settings can be editted inside the code.  Channel 4 is digitized and saved in WORD
 * format so that 16-bit data is transferred.  The voltage data is written to a text file that is saved
 * in the specified folder.  Further explanations of the commands used to interface with the oscilloscope
 * can be found in the Agilent InfiniiVision 3000 X-Series Oscilloscopes Programmer's Guide.
 */


using System;
using System.IO;
using System.Text;
using Ivi.Visa.Interop;
using System.Runtime.InteropServices;
using System.Threading;
using System.Diagnostics;
using System.Media;

namespace InfiniiVision
{
   class VisaComInstrumentApp
   {
      private static VisaComInstrument myScope;
      public static void Main(string[] args)
      {
         // User Inputs
         string folderName = @"c:\scope\data";   //outpath folder
         string date = "2_16_2014";  //date of experimental run
         int Temp = 35;  //steady state temperature
         string exp = "SS";
         int[] AVGCounts = new int[1] { 512};   //average counts desired
         int numRuns = 1;    //number of runs to perform at each average count setting
         /*
          * DO NOT CHANGE BELOW THIS LINE.
          * ----------------------------------------------------------------------------------------------
           */
         try
         {
            myScope = new VisaComInstrument("USB0::0x0957::0x17A4::MY52394016::0::INSTR");
            myScope.SetTimeoutSeconds(10);
            // Initialize - start from a known state.
            Initialize();
            // Capture data.
            Capture();
            // Analyze the captured waveform.
            Analyze(Temp, exp, folderName,date,AVGCounts,numRuns);
         }
         catch (System.ApplicationException err)
```

```
        {
            Console.WriteLine("*** VISA COM Error:" + err.Message);
        }
        catch (System.SystemException err)
        {
            Console.WriteLine("*** System Error Message : " + err.Message);
        }
        catch (System.Exception err)
        {
            System.Diagnostics.Debug.Fail("Unexpected Error");
            Console.WriteLine("*** Unexpected Error:" + err.Message);
        }
        finally
        {
            myScope.Close();
        }
    }

    /*
* Initialize the oscilloscope to a known state.
* ---------------------------------------------------------------
*/
    private static void Initialize()
    {
        string strResults;
        // Get and display the device's *IDN? string.
        strResults = myScope.DoQueryString("*IDN?");
        Console.WriteLine("*IDN? result is: {0}", strResults);
        // Clear status and load the default setup.
        myScope.DoCommand("*CLS");
        myScope.DoCommand("*RCL 2");
        myScope.DoCommand(":WGEN:OUTPut 1");
    }

    /* Capture Waveforms
   * ---------------------------------------------------------------------------------
   */
    private static void Capture()
    {
        // Set Acquisition Type
        myScope.DoCommand("ACQuire:TYPE AVERage");
        // For acquire type average
        myScope.DoCommand("ACQuire:COUNt 512");

    }

    /*
    * Analyze the captured waveform.
    * ---------------------------------------------------------------
    */
    public static void Analyze(int Temp, string exp, string folderName,string date,int[] AVGCounts,int numRuns)
    {
        //get timestamp
        DateTime saveNow = DateTime.Now;
        string Time = saveNow.ToString("hh_mm_ss");
        // Digitize desired channel
```

```
myScope.DoCommand(":DIGitize CHANnel4");

// Download waveform data.
// ------------------------------------------------------------

short[] ResultsArray; // Results array.
int nLength = 0;      // Number of data points

//Least significant byte transferred first
myScope.DoCommand(":WAVeform:BYTeorder LSBFirst");
//Unsigned integers turned off
myScope.DoCommand("WAVeform:UNSigned 0");
//Collects maximum number of points from the waveform record
myScope.DoCommand(":WAVeform:POINts:MODE MAXimum");
//Specifies that the channel 4 is the waveform to be collected
myScope.DoCommand(":WAVeform:SOURce CHANnel4");

//Specify WORD format so that 16-bit data is transferred
myScope.DoCommand(":WAVeform:FORMat WORD");

// Get the number of waveform points available.
myScope.DoCommand(":WAVeform:POINts 2000");
Console.WriteLine("Waveform points available: {0}",myScope.DoQueryString(":WAVeform:POINts?"));

// Writes the format of the data returned (WORD, BYTE, ASCII):
Console.WriteLine("Waveform format: {0}", myScope.DoQueryString(":WAVeform:FORMat?"));

// Display the waveform settings:
double[] fResultsArray;
fResultsArray = myScope.DoQueryNumbers(":WAVeform:PREamble?");
double fFormat = fResultsArray[0];
Console.WriteLine("fFormat is: {0}", fFormat);
if (fFormat == 0.0)
{
Console.WriteLine("Waveform format: BYTE");
}
else if (fFormat == 1.0)
{
Console.WriteLine("Waveform format: WORD");
}
else if (fFormat == 4.0)
{
Console.WriteLine("Waveform format: ASCii");
}
double fType = fResultsArray[1];
Console.WriteLine("fType is: {0}", fType);
if (fType == 0.0)
{
Console.WriteLine("Acquire type: NORMal");
}
else if (fType == 1.0)
{
Console.WriteLine("Acquire type: PEAK");
}
else if (fType == 2.0)
{
```

```
Console.WriteLine("Acquire type: AVERage");
}
else if (fType == 3.0)
{
Console.WriteLine("Acquire type: HRESolution");
}
double fPoints = fResultsArray[2];
Console.WriteLine("Waveform points: {0:e}", fPoints);
double fCount = fResultsArray[3];
Console.WriteLine("Waveform average count: {0:e}", fCount);
double fXincrement = fResultsArray[4];
Console.WriteLine("Waveform X increment: {0:e}", fXincrement);
double fXorigin = fResultsArray[5];
Console.WriteLine("Waveform X origin: {0:e}", fXorigin);
double fXreference = fResultsArray[6];
Console.WriteLine("Waveform X reference: {0:e}", fXreference);
double fYincrement = fResultsArray[7];
Console.WriteLine("Waveform Y increment: {0:e}", fYincrement);
double fYorigin = fResultsArray[8];
Console.WriteLine("Waveform Y origin: {0:e}", fYorigin);
double fYreference = fResultsArray[9];
Console.WriteLine("Waveform Y reference: {0:e}", fYreference);

//sets up output folder for the collected data
string tempString = date;
//string tempString = date;
string pathString = System.IO.Path.Combine(folderName, tempString);
System.IO.Directory.CreateDirectory(pathString);
string pathString1 = System.IO.Path.Combine(pathString, exp);
string folder1 = Temp.ToString() + "C";
string tempPathString = System.IO.Path.Combine(pathString1, folder1);

//Sends the average count command to the oscilloscope
for (int m = 0; m < AVGCounts.Length; m++)
{
   //Check steady state temperature and continue
   System.Media.SystemSounds.Beep.Play();
   ConsoleKeyInfo cki = new ConsoleKeyInfo();
   Console.WriteLine("\nCheck Temperature. Press Plus on Numerical Pad to continue.\n");
   do
   {
      Thread.Sleep(250);
      cki = Console.ReadKey(true);
   } while (cki.Key != ConsoleKey.Add);


   if (AVGCounts[m] == 512)
   {
      myScope.DoCommand("ACQuire:COUNt 512");
      Console.WriteLine("Number of averages is: {0}", AVGCounts[m]);
   }
   else if (AVGCounts[m] == 256)
   {
      myScope.DoCommand("ACQuire:COUNt 256");
      Console.WriteLine("Number of averages is: {0}", AVGCounts[m]);
   }
```

```
            else if (AVGCounts[m] == 128)
            {
               myScope.DoCommand("ACQuire:COUNt 128");
               Console.WriteLine("Number of averages is: {0}", AVGCounts[m]);
            }
            else if (AVGCounts[m] == 64)
            {
               myScope.DoCommand("ACQuire:COUNt 64");
               Console.WriteLine("Number of averages is: {0}", AVGCounts[m]);
            }
            else if (AVGCounts[m] == 32)
            {
               myScope.DoCommand("ACQuire:COUNt 32");
               Console.WriteLine("Number of averages is: {0}", AVGCounts[m]);
            }
            else if (AVGCounts[m] == 16)
            {
               myScope.DoCommand("ACQuire:COUNt 16");
               Console.WriteLine("Number of averages is: {0}", AVGCounts[m]);
            }
            else
            {
               myScope.DoCommand("ACQuire:COUNt 8");
               Console.WriteLine("Number of averages is: {0}", AVGCounts[m]);
            }

            // Current average count value
            int AverageNumb = AVGCounts[m];

            // Completes the number of waveform acquisitions that is desired
            for (int currentRun = 0; currentRun < numRuns; currentRun++)
            {

               Console.WriteLine("Beginning run {0}", currentRun);

               // Queries and collects the waveform data from the oscilloscope
               ResultsArray = myScope.DoQueryIEEEBlock("WAVeform:Data?");
               nLength = ResultsArray.Length;
               Console.WriteLine("Number of data values: {0}", nLength);

               // Set up output text file:
               string folder2 = AverageNumb.ToString();
               string pathString2 = System.IO.Path.Combine(tempPathString, folder2);
               System.IO.Directory.CreateDirectory(pathString2);
               int CR_MLform = currentRun + 1;
               //string fileName = date + "_waveform_data_" + Temp.ToString() + "_" + AverageNumb.ToString() +
"_" + CR_MLform.ToString() + ".txt";
               string fileName = date + "_waveform_data_" + exp + "_" + AverageNumb.ToString() + "_" +
CR_MLform.ToString() + "_" + Time + ".txt";
               string strPath = System.IO.Path.Combine(pathString2, fileName);
               if (File.Exists(strPath)) File.Delete(strPath);

               // Open file for output.
               StreamWriter writer = File.CreateText(strPath);

               // Writes time and voltage waveform data to the open text file
```

```
                for (int j = 0; j < nLength - 1; j++)
                    writer.WriteLine("{0:f9}    {1:f6}",
                    fXorigin + ((float)j * fXincrement),
                    (((float)ResultsArray[j] - fYreference)
                    * fYincrement) + fYorigin);



                // Close output file.
                writer.Close();
                Console.WriteLine("Waveform format BYTE data written to {0}",
                strPath);

                //get timestamp
                saveNow = DateTime.Now;
                Time = saveNow.ToString("hh_mm_ss");
                //Start another waveform acquisition
                myScope.DoCommand(":DIGitize CHANnel4");
            }
        }
    }
}

   class VisaComInstrument
{
private ResourceManager m_ResourceManager;
private FormattedIO488 m_IoObject;
private string m_strVisaAddress;
// Constructor.
public VisaComInstrument(string strVisaAddress)
{
// Save VISA addres in member variable.
m_strVisaAddress = strVisaAddress;
// Open the default VISA COM IO object.
OpenIo();
// Clear the interface.
m_IoObject.IO.Clear();
}
public void DoCommand(string strCommand)
{
// Send the command.
m_IoObject.WriteString(strCommand, true);
// Check for inst errors.
CheckInstrumentErrors(strCommand);
}
public void DoCommandIEEEBlock(string strCommand,byte[] DataArray)
{
// Send the command to the device.
m_IoObject.WriteIEEEBlock(strCommand, DataArray, true);
// Check for inst errors.
CheckInstrumentErrors(strCommand);
}
public string DoQueryString(string strQuery)
{
// Send the query.
m_IoObject.WriteString(strQuery, true);
```

```
// Get the result string.
string strResults;
strResults = m_IoObject.ReadString();
// Check for inst errors.
CheckInstrumentErrors(strQuery);
// Return results string.
return strResults;
}
public double DoQueryNumber(string strQuery)
{
// Send the query.
m_IoObject.WriteString(strQuery, true);
// Get the result number.
double fResult;
fResult = (double)m_IoObject.ReadNumber(
IEEEASCIIType.ASCIIType_R8, true);
// Check for inst errors.
CheckInstrumentErrors(strQuery);
// Return result number.
return fResult;
}
public double[] DoQueryNumbers(string strQuery)
{
// Send the query.
m_IoObject.WriteString(strQuery, true);
// Get the result numbers.
double[] fResultsArray;
fResultsArray = (double[])m_IoObject.ReadList(
IEEEASCIIType.ASCIIType_R8, ",;");
// Check for inst errors.
CheckInstrumentErrors(strQuery);
// Return result numbers.
return fResultsArray;
}
public short[] DoQueryIEEEBlock(string strQuery)
{
   // Send the query.
   m_IoObject.WriteString(strQuery, true);
   // Get the results array.
   System.Threading.Thread.Sleep(2000); // Delay before reading.
   short[] ResultsArray;
   // Sets the unit to little endian
   m_IoObject.InstrumentBigEndian = false;
   ResultsArray = (short[])m_IoObject.ReadIEEEBlock(
   IEEEBinaryType.BinaryType_I2, false, true);
   // Check for inst errors.
   CheckInstrumentErrors(strQuery);
   // Return results array.
   return ResultsArray;
}
private void CheckInstrumentErrors(string strCommand)
{
// Check for instrument errors.
string strInstrumentError;
bool bFirstError = true;
do // While not "0,No error".
```

```
    {
m_IoObject.WriteString(":SYSTem:ERRor?", true);
strInstrumentError = m_IoObject.ReadString();
if (!strInstrumentError.ToString().StartsWith("+0,"))
{
if (bFirstError)
{
Console.WriteLine("ERROR(s) for command '{0}': ",
strCommand);
bFirstError = false;
}
Console.Write(strInstrumentError);
}
} while (!strInstrumentError.ToString().StartsWith("+0,"));
}
private void OpenIo()
{
m_ResourceManager = new ResourceManager();
m_IoObject = new FormattedIO488();
// Open the default VISA COM IO object.
try
{
m_IoObject.IO =
(IMessage)m_ResourceManager.Open(m_strVisaAddress,
AccessMode.NO_LOCK, 0, "");
}
catch (Exception e)
{
Console.WriteLine("An error occurred: {0}", e.Message);
}
}
public void SetTimeoutSeconds(int nSeconds)
{
m_IoObject.IO.Timeout = nSeconds * 1000;
}
public void Close()
{
try
{
m_IoObject.IO.Close();
}
catch { }
try
{
Marshal.ReleaseComObject(m_IoObject);
}
catch { }
try
{
Marshal.ReleaseComObject(m_ResourceManager);
    }
catch { }
}
}
}
```

VITA

Kelsey Michele Winstead was born in Harrisburg, PA to Joel and Suzanne Winstead. When she was 3 years old she moved to Memphis, TN with her parents. In 2007, she began her college career at the University of Tennessee at Knoxville. Though she originally wanted to be a doctor, her parents encouraged her to first pursue a technical degree. Thus, she studied aerospace engineering and ended up loving it. She graduated with a Bachelors of Science degree in May 2012. She has conducted heat transfer research for the Mechanical, Aerospace, and Biomedical Engineering Department from August 2011 to May 2014. She intends to pursue a career in the aerospace industry.